12-2022

# ADVANCED THOMSON SCATTERING DIAGNOSTICS FOR VARIOUS APPLICATIONS

Zichen He
zhe9@vols.utk.edu

To the Graduate Council:

I am submitting herewith a dissertation written by Zichen He entitled "ADVANCED THOMSON SCATTERING DIAGNOSTICS FOR VARIOUS APPLICATIONS." I have examined the final electronic copy of this dissertation for form and content and recommend that it be accepted in partial fulfillment of the requirements for the degree of Doctor of Philosophy, with a major in Mechanical Engineering.

Zhili Zhang, Major Professor

We have read this dissertation and recommend its acceptance:

Zhili Zhang, Yanfei Gao, Jeff Reinbolt, Mark Gragston

Accepted for the Council:

Dixie L. Thompson

Vice Provost and Dean of the Graduate School

(Original signatures are on file with official student records.)

# ADVANCED THOMSON SCATTERING DIAGNOSTICS FOR VARIOUS APPLICATIONS

A Dissertation Presented for the
Doctor of Philosophy
Degree
The University of Tennessee, Knoxville

Zichen He
December 2022

# ACKNOWLEDGEMENTS

I would like to express my gratitude to those who supported my PhD study over these years: First and foremost, I am grateful to my advisor, Dr. Zhili Zhang, for his invaluable guidance and continuous support in my PhD study. I would also like to thank Dr. Theodore Biewer, who has given me the opportunity to join the PDP project at Oak Ridge National Laboratory. Special thanks goes to Hangyao Li for her profound moral support. Additionally, I thank you, my dear bikes, for your loyal services. And lastly, thank you, Coffee, for always being there for me to drink when I wrote this dissertation.

# ABSTRACT

Controlled nuclear fusion has been pursued as an ideal form of renewable energy for decades and the study of fusion plasma is fueling an increased demand for diagnostic capability. Furthermore, with the increasing applications of plasma in industry and medicine, it has become essential to characterize plasma dynamics and properties. Laser Thomson scattering diagnostics are considered to be the most reliable plasma diagnostic approaches for measuring electron temperature and electron density, the two most important parameters of a plasma. Four advanced Thomson scattering systems are discussed in this work to respectively address four different limitations or difficulties commonly encountered in conventional Thomson scattering based plasma diagnostic scenarios.

The background of this study is discussed in Chapter One. Chapter Two discusses the solution for lifting the limitation of spatial resolution of Thomson scattering diagnostics. A multi-point Thomson scattering system has been implemented for an electrothermal arc source to test its diagnostic capability. A high-speed Thomson scattering system is demonstrated in Chapter Three as a solution to the low temporal resolution in the conventional setup. This chapter presents the development of a high-repetition-rate Thomson scattering system to greatly increase the temporal resolution of measurements while maintaining a high rate of data acquisition. Chapter Four identifies a challenge in low-temperature plasma, especially in a weakly ionized gas discharge, that the probing laser of a Thomson scattering system could also induce rotational Raman scattering. A new approach presented in this chapter bypasses the necessity of making the estimation of gas temperature and seek to resolve this problem directly with a forward scattering approach. Chapter Five demonstrates a preliminary study on a compressed sensing-based enhanced data acquisition technique for future planar laser-based 2D Thomson scattering diagnostic. The work presented in this chapter demonstrates a compressed single-shot hyperspectral imaging system. And lastly, Chapter Six summarizes all works in the four tasks and discusses unaddressed problems, potential upgrades and future works.

# TABLE OF CONTENTS

# LIST OF FIGURES

# CHAPTER ONE
# INTRODUCTION

## Background

Thomson scattering (TS) is one of the plasma diagnostic approaches that measures electron temperature ($T_e$) and electron density ($n_e$), the two most important parameters of a plasma. As Thomson scattering is the most reliable and trusted plasma diagnostic technique [1], the aim of this research is to improve Thomson scattering diagnostics by providing solutions to difficulties encountered in the conventional Thomson scattering systems with more advanced configurations of the Thomson scattering system. The diagnostic in this work mainly focuses on thermonuclear fusion-relevant plasmas.

### *The Pursuit for an Ideal Power Source*

Harnessing the heat released from thermonuclear fusion reaction to generate electricity is known as fusion power and has been pursued as an ideal source of renewable energy for decades. Among other advantages, the most attractive attribute of fusion power is the vast amount of potential fuel reserve on Earth. As the energy produced by fusion is essentially the binding energy released from fusing lighter atoms into heavier ones, and there are plenty of light elements on Earth, such as hydrogen. Fusion power is seen as the future energy technology that would reduce the global carbon footprint and relieve the world from the potential energy crises often associated with fossil fuels.

The first thermonuclear fusion reaction was demonstrated by Rutherford back in 1934, when he fused deuterium and tritium, isotopes of hydrogen, into helium [2]. But it was not until the 1950s when researchers around the world began to explore the possibility of controlled thermal nuclear fusion intently. To control the fusion process, the fusion plasma has to be confined to prevent the plasma from quickly dissipating. Many confinement concepts have been proposed and evaluated and can be broadly categorized into either magnetic or inertial confinement.

One of the most well-known magnetic confinement concepts is called a "tokamak". Proposed by Igor Tamm and Andrei Sakharov, a tokamak is one of the earliest magnetic confinement concepts [3]. The word "tokamak" is a transliteration of the Russian abbreviation for "toroidal chamber with magnetic coils" [3]. In 1968, the T-3 tokamak of the former Soviet Union reached a performance ten times higher than any other fusion devices of other magnetic or inertial confinement concepts at that time, and the tokamak immediately became the most popular plasma confinement technique for controlled thermonuclear fusion [4]. In the 1980s, an international fusion project named "International Thermonuclear Experimental Reactor" (ITER) was initiated to build the world's largest tokamak and demonstrate the technological feasibility of fusion power on a practical scale [4]. Currently, ITER is specifically designed to have a fusion energy gain factor of 10 (Q=10), producing 500 MW of fusion power from 50 MW of input power [5]. As of 2022, ITER is still under construction in France. The diagram of ITER is shown in Figure 1 (a).

Except for tokamak, there are other magnetic confinement concepts such as stellerators [6]. Unlike tokamaks that run an electric current through the plasma and creates a magnetic field on its own that pulls the plasma in along with external magnets, and keeps the plasma away from the reactor wall, stellarators rely on non-axisymmetric external magnetic field coils to create the rotational transform of a helical magnetic field to confine the plasma [7]. This confinement design, compared to tokamak, has the advantage of theoretically eliminating plasma instability. A diagram of a stellarator is shown in Figure 1 (b).

The alternative but less popular approach in controlled thermal nuclear fusion is inertial confinement. Inertial confinement is like trying to achieve fusion with brute force. The concept is imitating the fusion environment of the Sun (high temperature and high pressure) by heating small pellets of fusion fuel with high-energy driver beams, such as particle beams, or more commonly, laser beams.

**(a)**

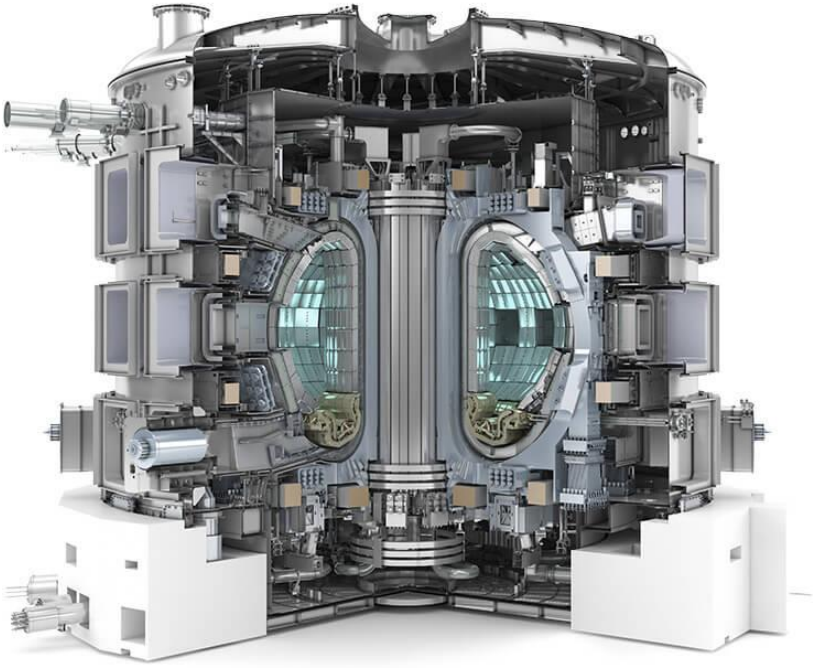

**(b)**

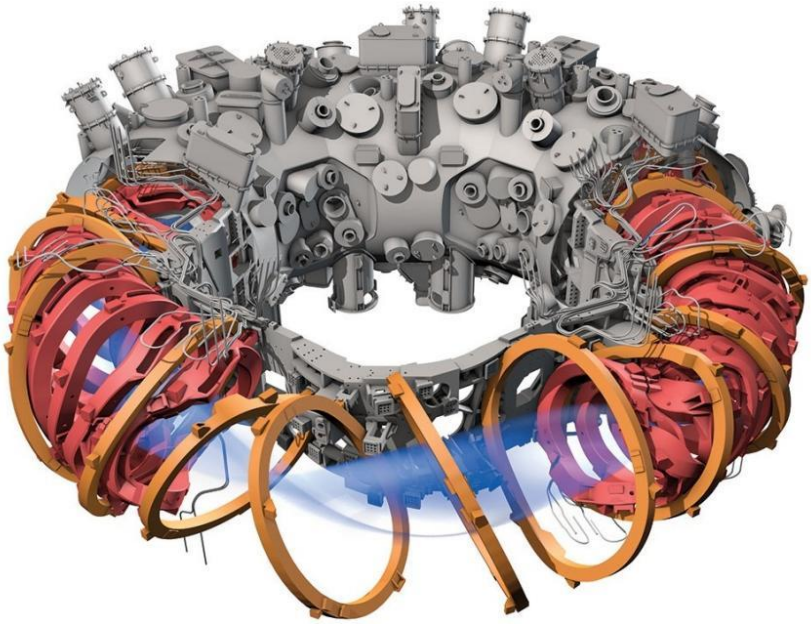

**Figure 1.** Diagrams of magnetic confinement fusion devices. (a) A diagram of ITER tokamak (from https://fusionforenergy.europa.eu). (b) A diagram of Germany's Wendelstein 7-X stellarator (from https://www.science.org).

The driver beams are designed to produce kinetic force on the fuel pellet so that they apply physical compression on the surface of the pellet. The ablation of the heated outer layers of the fuel pellets will be ionized and implode, producing a shock wave that compresses the center of the of the pellet, heating it to fusion temperatures, thus fusion occurs inside the fuel pellet under high temperature and high pressure.

***Plasma Disruption***

Thermonuclear fusion requires a very high temperature environment to overcome the Coulomb barrier so the lighter nuclei in the plasma may fuse together and form into a heavier nucleus when they collide as they move in the plasma. It also requires sufficient confinement time so the plasma would sustain long enough for the collision to occur. Moreover, the density of the plasma also affects the chance, or cross-section, of collision between two nuclei. To sustain fusion, the fusion plasma needs to be constantly heated. The heating power is provided by both the external heating that supports fusion and the internal heat that is generated by fusion. Therefore, the hotter the fusion plasma, the less external heating is required to sustain fusion, and the higher the fusion energy gain factor. When the internal heating from the fusion plasma is hot enough to sustain itself, that external heating is no longer required, the plasma is said to have undergone "ignition". The triple product ($n_e T_e \tau_E$) of plasma electron density ($n_e$), electron temperature ($T_e$), and confinement time ($\tau_E$) is an indicator of how close a fusion device is to ignition [8], and the minimum value of this triple product to reach ignition is known as Lawson criterion.

However, for fusion power devices, especially for reactors of which the plasma confinement relies on the plasma current such as Tokamak and Tokamak-based devices like ITER, one of their major challenges is the confinement time. During operation, the fusion plasma confined in the reactor could become unstable and lead to plasma disruption, a phenomenon that results in cease of fusion reaction by rapid loss of thermal energy and magnetic confinement [9, 10]. During a disruption, the particles in the fusion plasma escapes the magnetic confinement and hit the reactor wall, often resulting in damage to the

wall surface. Less destructive instabilities such as Edge Localized Modes (ELMs) could also damage the reactor wall due to loss of confinement.

### *Edge Localized Modes*

ELMs, a phenomenon first observed in the high confinement mode (H-mode) of the ASDEX tokamak in 1981 [11], are a class of violent plasma quasi-periodic instability occurring near the inner walls of the fusion chamber of tokamak-like fusion devices [12, 13]. An ELM is essentially a sudden loss of plasma confinement which results in a significant release of heated particles from the fusion plasma onto the plasma-facing components in the fusion chamber, such as the inner wall surface. This results in a reduction of the lifetime of the plasma-facing components due to plasma erosion. Such instabilities have become a major challenge for controlled fusion [14]. Although ELMs have been studied for decades, the mechanism of ELMs has not yet been fully clarified. Thomson scattering is the most trusted diagnostic tool in fusion research, and it was widely used as one of the primary plasma diagnostic approaches to help plasma physicists understand the nature of fusion plasma instabilities.

## Thomson Scattering Diagnostics

### *Thomson Scattering*

Thomson scattering is a phenomenon in plasma physics that photons elastically collide and then bounce off from free charged particles such as free electrons in the plasma. From the classical perspective, which regards photons as electromagnetic waves, Thomson scattering is an electromagnetic wave that forces the free charged particle to oscillate in the direction of the electric field of the electromagnetic wave. The oscillation of the free charged particle is essentially an electromagnetic dipole radiation emitting at the same frequency as the incident wave, which is Thomson scattering.

Thomson scattering diagnostics is based on the physical phenomenon of Thomson scattering. The diagnostic uses coherent light, typically from a laser, to probe the plasma. Although, the wavelength of the photons from the incident light does not change after the

scattering, from the observer's view, the observed wavelength from the scattering changes with scattering angle, which is the angle between the vector of a photon before and after the scattering. This change of observed wavelength is due to thermal Doppler broadening. Thermal Doppler broadening of spectral lines is caused by the random thermal motions of particles, due to the Doppler effect that occurs when the particles move relatively to the observer. The observed broadening is a Gaussian distribution with a standard deviation defined by Equation 1, and a full width at half maximum (FWHM) defined by Equation 2, where $\sigma_\lambda$ denotes the standard deviation, and $\lambda$ is the incident wavelength, $k_B$ is the Boltzmann constant, T is the temperature of the particle, c is the speed of light and m the mass of the particle and $\Delta\lambda_{FWHM}$ is the FWHM of the Doppler profile.

$$\sigma_\lambda = \lambda\sqrt{k_B T/mc^2} \tag{1}$$

$$\Delta\lambda_{FWHM} = \lambda\sqrt{8kT \cdot \ln 2/mc^2} \tag{2}$$

Doppler shift in Thomson scattered light is defined by Equation 3, where $\Delta\lambda$ is the amount of change in wavelength, $\lambda_s$ is the wavelength after scattering, $\boldsymbol{v}$ the velocity of the scatterer, in which case, the free electron, and c the speed of light.

$$\Delta\lambda = \lambda_s - \lambda = (\boldsymbol{k} \cdot \boldsymbol{v})\,\lambda^2 / (2\pi c) \tag{3}$$

The $\boldsymbol{k}$ vector denotes the differential scattering wave factor, which is the difference between the scattered wave vector and incident wave vector, indicating the scattering effect on a photon. The $\boldsymbol{k}$ vector is defined by Equation 4, where $\theta$ is scattering angle.

$$|\boldsymbol{k}| = 4\pi \cdot \sin(\theta/2)/\lambda \tag{4}$$

***Thomson Scattering in Plasma Diagnostics***

The reason Thomson scattering diagnostics is so widely welcomed in plasma research, especially in fusion plasma, is not only due to its reliability but that the diagnostic technique is considered non-intrusive compared to other diagnostic methods like Langmuir probe, which needs contact with the plasma environment. Thomson scattering is based on a direct physical phenomenon, which provides an advantage compared to passive optical emission spectroscopy, which requires a collisional radiative model to help "translate" the emission spectrum into meaningful plasma parameters. Thus, emission spectroscopy is indirect and possibly inaccurate depending on the model validity and applicability. Moreover, in fusion plasma, as mentioned previously, the triple product of Lawson criterion is composed of the electron density and temperature of plasma, and time of confinement. Thomson scattering is able to reliably provide two out of the three parameters, and the last one, time of confinement, is easy to measure. Hence, there is strong interest in Thomson scattering measurements.

The calculation of electron temperature and density from Thomson scattering is based on the profile of the Thomson scattering spectrum induced by the probing laser and is typically measured with a spectrometer. The observed profile of a Thomson scattering spectrum is a Voigt distribution, which is the convolution of a Lorentz distribution (natural broadening) and a Gaussian distribution (thermal Doppler broadening). However, the spectral profile is approximated with a Gaussian distribution for simplicity of curve fitting, because the line broadening by Doppler shift is the dominating broadening effect in Thomson scattering. Electron temperature and electron density of the plasma can be calculated from the parameters of the fitted Gaussian curve. The electron temperature is defined as Equation 5 [15, 16],

$$T_e = \frac{m_e c^2}{8k_B \sin^2(\theta/2)} \times \frac{\Delta\lambda^2}{\ln(2)\lambda^2} \tag{5}$$

where $m_e$ is the electron mass (0.511 MeV/$c^2$), $k_B$ is the Boltzmann constant ($8.617 \times 10^{-5}$ eV/K), $\theta$ is the scattering angle, and $\Delta\lambda$ is the half-width-at-half-maximum of the Thomson scattering profile. The electron density measured from Thomson scattering diagnostics indicates the absolute number density of free electrons in the plasma. In this work, it is calibrated with rotational Raman spectrum of nitrogen in air, as shown in Equation 6 [15, 16],

$$n_e = \frac{A_e}{A_{N_2}} \times \frac{d\sigma_{N_2}/d\Omega}{d\sigma_e/d\Omega} \times n_{N_2} \times f \tag{6}$$

where $A_e$ is the total emission power of Thomson scattering, $A_{N_2}$ is the total emission power of rotational Raman line of nitrogen at J=4→6, $d\sigma_{N_2}/d\Omega$ and $d\sigma_e/d\Omega$ are differential cross section of rotational Raman of nitrogen at wavelength of the probing laser ($3.82 \times 10^{-30}$ $cm^2$/sr at 532 nm) and differential cross section of Thomson scattering ($7.94 \times 10^{-26}$ $cm^2$/sr) respectively, $n_{N_2}$ is the molecule number density of nitrogen in air ($0.79 \times 44.94$ mol $\times$ $N_A$; $N_A$ is Avogadro's constant), and lastly, $f$ is the fraction of rotational Raman scattering of nitrogen at the J=4→6 transition.

This absolute calibration of electron density does not necessarily require the transition line at J=4→6. The reason it is chosen in this work is because it has relatively the high intensity out of all the Raman lines for rotational Raman scattering of air, which offers relatively higher signal-to-noise ratio and therefore reduce uncertainty of measurement. The mechanism of this calibration is based on the idea that the absolute number density of $N_2$ molecules in the ambient air can be calculated based on ideal gas law; and the total emission power of rotational Raman scattering from the $N_2$ in the air, which is induced by the same laser that probes the plasma, can be obtained from the rotational Raman spectrum; meanwhile, the same laser (same wavelength and same pulse energy) probes the free electrons in the plasma and induces Thomson scattering. Since both spectra, Thomson scattering and rotational Raman scattering, are induced by the same laser, and the emission power of both scatterings also linearly scale with the laser power, theoretically, the

emission power of both scattering divided by each of their cross sections and quantities of the particle should yield the same result, which is the intensity of the laser beam per particle. So, at this point, the number density of $N_2$ molecules is known, and both of their emission powers are measured from their spectra, the only unknown part is the density of free electrons. Consequently, the number density of free electrons can be calibrated based on the knowledge of density-to-emission ratio from rotational Raman scattering and the cross sections of electron and $N_2$ molecule, as both scatterings are induced by the same electromagnetic wave. Moreover, this absolute calibration does not necessarily have to be rotational Raman of air, or $N_2$, it could be Raman of other gases, or even other laser induced scatterings like Rayleigh scattering, as long as the laser pulse energy-to-scattered intensity ratios are calculated correctly.

***Conventional Thomson Scattering System***

Figure 2 shows an example of the setup of a conventional Thomson scattering system. The laser, typically a red or green laser, is focused onto and steered into the plasma by a set of laser optics. The focal point of the laser focusing lens is where the intensity of the laser beam is the highest, that is also where the signal of Thomson scattering is the strongest. A set of collection optics, usually including a camera lens, collects Thomson scattered light at the scattering angle (observation angle) of 90 degrees. The optical axis of the collection optics is perpendicular to the polarization of the laser to obtain maximum signal strength of Thomson scattering. As the wavelength of both Rayleigh scattering and stray light (mostly the reflection of laser beam) are the same as laser, and the magnitude of Rayleigh scattering is approximately 100 times larger than Thomson scattering. Therefore, the contamination of Rayleigh scattering and stray light have always been a major noise source in Thomson scattering measurements. Usually stray light mitigation techniques are implemented to reduce the stray light noise in the spectrum, and sometimes an optical or physical filter is used to block Rayleigh scattering.

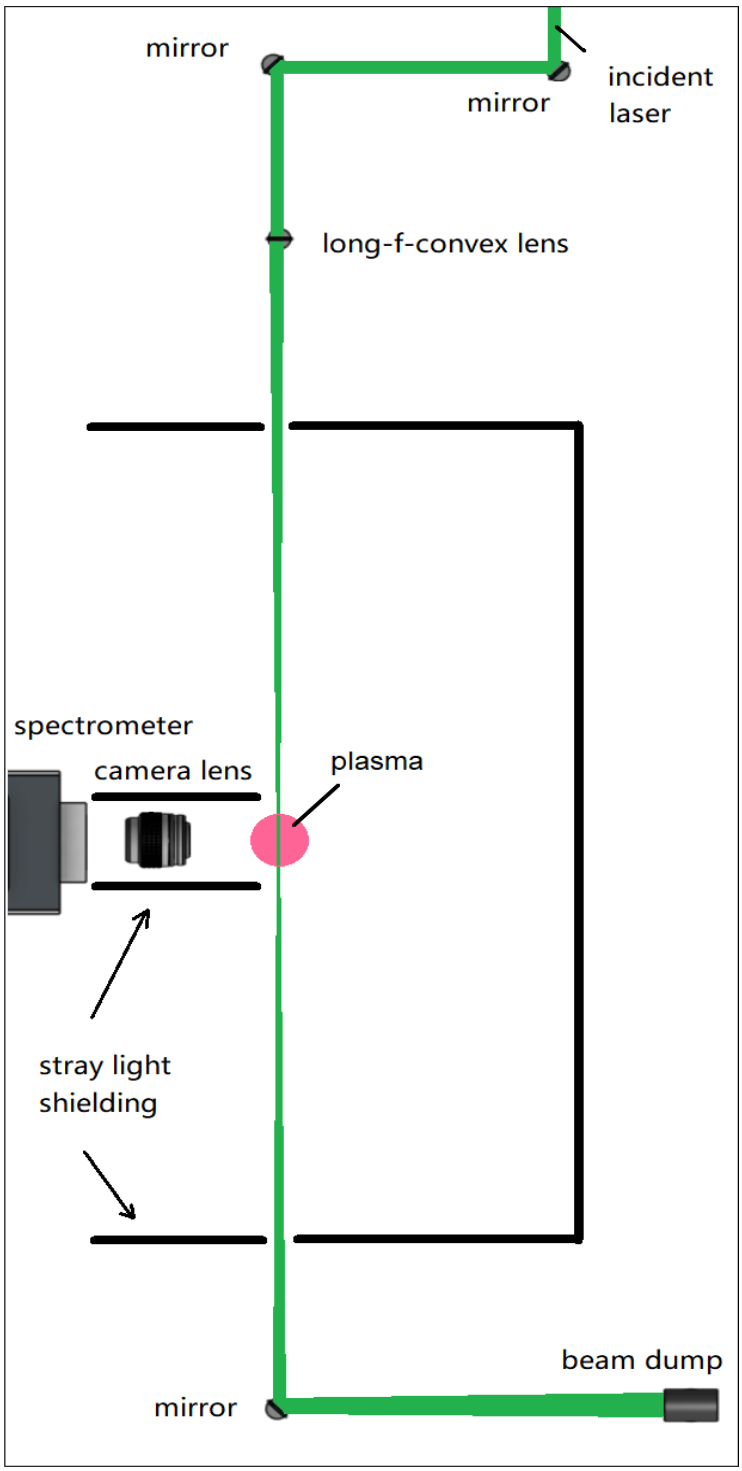


**Figure 2.** A typical setup for conventional laboratory Thomson scattering system for glow discharge.

***Error Analysis for Thomson Scattering Diagnostics***

The error analysis for Thomson scattering diagnostics used in this work is illustrated in Figure 3. The raw spectrum contains Thomson scattered light, as well as plasma emissions, Rayleigh scattering, stray light from the collection optics as well as noises from electronics. The electronics in the scientific camera affects the original signal with: statistical uncertainty, instrumental broadening, baseline offset, and camera white noise. The statistical uncertainty is caused by the time-varying camera sensitivity to photons.

The instrumental broadening is essentially a blurring effect due to the inevitable imperfection in manufacturing of optical elements in a practical imaging device. That blurring effect is presented as line-broadening in spectroscopy. The baseline offset and white noise are common electrical noises in electronic signals, which is also present in scientific cameras. The intensity calibration is a process to correct camera detectors' uneven sensitivity to different wavelengths, which is neglected due to the narrow spectral range needed for Thomson scattering measurements in this work. All these electronic "effects" to the original Thomson scattering signal are described with transfer functions (also known as point spread functions in electrical engineering) and known as signal degradation, which are electrically or digitally removed as noises.

To remove the noises from a degraded Thomson scattering signal, the process is to perform an inverse process of how the degraded signal is physically generated. That is removing baseline, stray light, plasma emission and Rayleigh scattering from the raw Thomson scattering spectrum. Then a Gaussian curve can be fitted to the Thomson scattering spectrum as its spectral profile, this process introduces a fitting error to the final results. To remove broadening, one must first identify the broadening effect of the spectrometer-camera system, of which the transfer function is commonly described as a convolution with a Gaussian function. So, the Thomson scattering profile should de-convolves with the broadening transfer function to restore the true spectral profile of the Thomson scattering measurement.

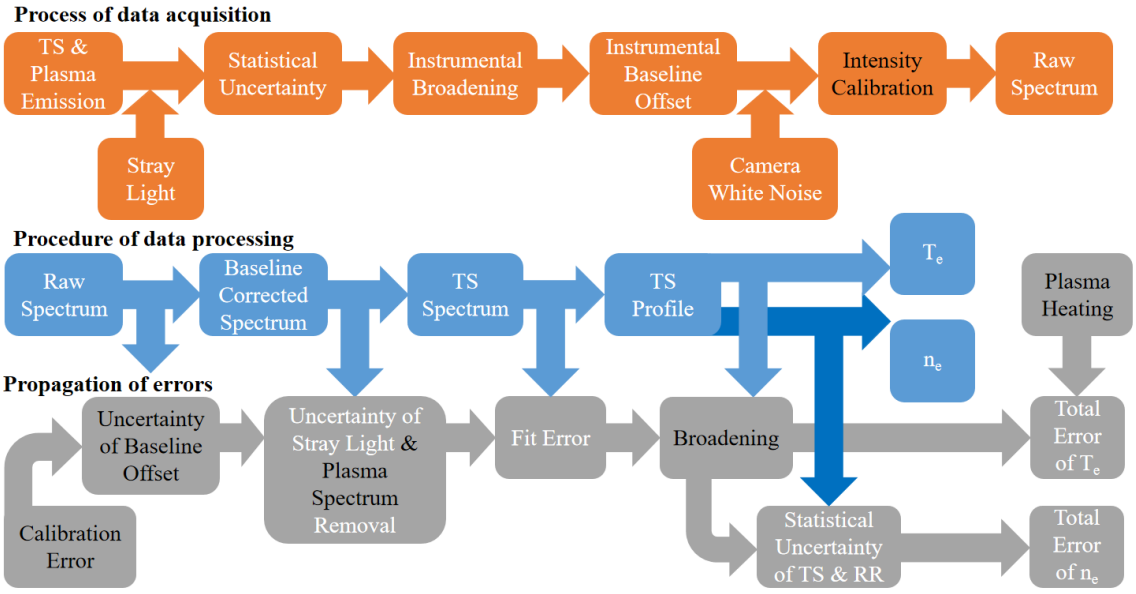


**Figure 3.** A flow chart showing full propagation of errors that analyzes the uncertainty of Thomson scattering measurements. The black texts indicate the neglected errors. The orange tiles illustrate the process of data acquisition, blue tiles as procedure of data processing, and gray tiles as full propagation of errors.

The error of instrumental broadening is neglected in this work, as the magnitude of error in wavelength is only on sub-nm level, meaning the error on the measured electron temperature is only about 1%, due to the use of high resolution gratings (1200 g/mm or higher) in the spectrometers.

For calculation of electron density, as it requires calibration with a rotational Raman spectrum, the uncertainties that the Raman spectrum carries also should be included in the error propagation of electron density measurement. For calculation of electron temperature, an additional error is plasma heating via inverse-bremsstrahlung effects [17, 18]. It is the energy of the laser accelerating the free electrons, hence inevitably increasing their temperature during Thomson scattering measurements. The procedure of removing this error requires "zero pulse energy", which is taking measurements of the same plasma with various pulse energy (e.g., from 100 to 200 mJ/pulse), and then plot a regression curve based on the known pulse energy-to-electron temperature relationship to find the supposed electron temperature at "zero pulse energy". Plasma heating is a neglected error in this work, due to the difficulty in obtain signals as low energy and complication of tuning laser pulse energy.

***Limitations in Conventional Thomson Scattering Diagnostics***

To better understand characteristics of plasmas, Thomson scattering systems of higher performance that provide more detail on plasma than that is presently available is much desired for plasma-related researches. Four limitations in the diagnostic capability of the conventional Thomson scattering system are identified and addressed separately as four tasks in this study. Each task demonstrates an advanced Thomson scattering system that is dedicated to overcoming or at least improve one of the four limitations. The limitations and solutions addressed in each task is listed discussed below.

Task 1: as the plasma is probed by a focused laser, the conventional Thomson scattering measurement is limited to a single point, which is the focal point of the laser focusing lens. The first task is to resolve this limitation by increasing the lines-of-sight of detection: a

Thomson scattering system will be implemented on a high density and low temperature electrothermal arc source. The collection optics will include a bundle of 11 optical fibers, lining up radially to the arc, thus providing simultaneous multi-point measurement. Each line-of-sight from the fibers will provide a Thomson scattering spectrum, thus a theoretically 11-point radial profile of electron temperature and density can be established for the plasma. This task investigates the feasibility of increasing detection lines-of-sight of Thomson scattering diagnostics.

Task 2: similar to Task 1, the sampling rate of a Thomson scattering system is also limited by the laser. Because the camera captures Thomson scattering spectra only as fast as the repetition rate of the pulsed laser, which is typically as low as tens of Hertz.Task 2 aims to lift the limitation on temporal resolution with a high-repetition-rate pulse-burst laser system that will greatly increase the sampling rate of Thomson scattering measurements. The Thomson scattering system will be implemented on table-top plasmas to validate the feasibility of obtaining ~100 meaningful data points at a sampling rate of 10 kHz.

Task 3: unlike the first two tasks that focus on fusion research, the third task addresses a problem in the field of low temperature plasma, especially for weakly ionized plasmas. The problem is Thomson scattering spectrum being entangled with rotational Raman spectrum in Thomson scattering measurements. In this work, the goal is to spectrally separate Thomson scattering and rotational Raman scattering spectrum. Thomson scattering spectrum will be collected in forward scattering directions to compress the width of Thomson scattering spectrum, so it will be narrow enough to “sit” in the gap between the Stokes and anti-Stokes lines of simultaneously measured rotational Raman scattering. The separated Thomson and rotational Raman scattering spectra will provide simultaneous measurements of electron temperature, electron density, as well as temperature of the gas present in the weakly ionized plasma.

Task 4: the last task addresses a general limitation in spectroscopy, which is the spectral image captured by any spectrometer loses all information from a spatial dimension due to

the mechanism of spectrometer. The task aims to preserve the lost information of the spatial dimension with hyperspectral reconstruction. This will be a preliminary study that can be potentially implemented on Thomson scattering diagnostic in the future to obtain single-shot hyperspectrum of Thomson scattering. The preliminary study will be a proof-of-principle that validates the feasibility of reconstructing a 3D Thomson scattering hyperspectrum from a coded single-shot 2D spectrum. The preliminary study will use the spectrum of a methane-air flame emission instead and computationally reconstruct it into a hyperspectrum based on a compressed sensing algorithm.

# CHAPTER TWO
# IMPLEMENTATION OF A PORTABLE DIAGNOSTIC SYSTEM FOR THOMSON SCATTERING MEASUREMENTS ON AN ELECTROTHERMAL ARC SOURCE

A version of the contents in this chapter was presented on High-Temperature Plasma Diagnostics (HTPD) Conference in 2022 and published Review of Scientific Instruments.

To fulfill the increasing needs for plasma diagnostic support for researchers in fusion technology, a portable diagnostic package (PDP) equipped for both laser Thomson scattering (TS) and optical emission spectroscopy (OES) has been designed and constructed at Oak Ridge National Laboratory (ORNL), aiming to measure temperature and number density of electrons and temperatures of ions in plasmas for fusion devices. The PDP has been initially implemented on a high density and low temperature electrothermal arc source (ET-arc) at ORNL to test its TS capability. TS from the plasmas in the ET-arc has been obtained using the PDP. The electron temperature and number density were determined from TS spectra. These results were then compared to measurements from previous studies on the ET-arc. The TS diagnostic measured 0.82 ± 0.10, 1.31 ± 0.15 and 0.71 ± 0.08 eV and $(4.36 \pm 0.50) \times 10^{21}$, $(5.86 \pm 0.66) \times 10^{21}$ and $(4.31 \pm 0.48) \times 10^{21}$ $m^{-3}$ from respectively 3 lines-of-sight that transect the plasma column.

## Introduction

For decades, fusion energy has been pursued as an ideal power source. But the challenge of finding a sustainable confinement method for fusion reactions in order to achieve long-term net positive energy gain remains today. Laser Thomson scattering (TS) is a reliable and well-trusted diagnostic technique for accurate and simultaneous measurements of time-resolved local electron number density and temperature of plasmas [15, 19, 20]. Therefore, TS has become one of the key plasma diagnostic methods that provides performance validation and understanding of the underlying physics for plasma confinement techniques

in fusion technology. However, a state-of-the-art diagnostic system is normally immobile and designed only for a specific fusion experiment, and not all fusion projects can equip a state-of-the-art TS diagnostic system. With the increasing need of plasma diagnostic support, especially TS, the concept of a modular Thomson scattering and optical emission spectroscopy (OES) diagnostic system has been funded by the Advanced Research Projects Agency-Energy (ARPA-E) to create a mobile plasma diagnostic system that can be transported and shared among various fusion facilities [21]. Additionally, the measurements by the same diagnostic system will be more consistent and comparable.

The portable diagnostic package (PDP) is developed to fulfill this concept. It is a transportable plasma diagnostic suite, providing both TS and OES, movable to where high-performance plasma diagnostics are needed. The PDP is packed with a Quantel Q-smart 1500 amplified Nd:YAG laser, two Princeton Instruments SCT320 spectrometers each with a triple grating turret, two Princeton Instruments PI-MAX4 intensified cameras (for simultaneous TS and OES measurements), and an optical fiber bundle providing 11 line-of-sight inputs to each spectrometer. The PDP also comes with a computer with a dedicated data storage unit and on-board data processing software (MATLAB). A photograph of the PDP is shown in Figure 4. The main devices of the PDP are loaded on a cart. The cart has 4 layers, providing storage space for (respectively from top layer to the bottom): camera and spectrometer #1, camera and spectrometer #2, an optical fiber panel, computer main frame and data storage unit. Either camera #1, #2 or both can be used for TS measurements, depending on the configuration at the optical fiber panel.

The PDP has been transported within Oak Ridge National Laboratory (ORNL) by a van from its original assembly laboratory to the laboratory where the electrothermal arc (ET-arc) source is located (a distance of ~3 miles). This was to test the mobility and TS

**(a)**

**(b)**

**Figure 4.** Photographs of the portable diagnostic package (PDP), which includes. (a) A mobile cart carrying 2 sets of Princeton Instruments SCT320 spectrometers and PI-MAX4 iCCD cameras, and (b) a Quantel Q-smart 1500 amplified Nd: YAG laser with laser steering optics.

performance of the system. The ET-arc source was originally developed to produce transient plasma heat and particle fluxes to simulate and study the plasma-material interaction of edge localized modes in tokamaks [13, 22, 23]. The high-velocity and undirectional plasma jet created by the ET-arc source was a 1 ms Helium gas jet ionized by a high voltage and high current DC capacitive discharge [24].

In previous studies on the ET-arc, the arc discharge process was monitored by a FLIR SC4000 infrared camera, two Tektronix P6015A high voltage probes and a Pearson Model 5664 current monitor to obtain the images of the plasma, voltage and current data of each discharge period, respectively. An Ocean Optics LIBS 2500+ spectrometer was used to obtain OES of the ET-arc [23, 25]. The OES and collisional radiative model (CRM) based characterization of the ET-arc indicated its electron temperature ($T_e$) and electron number density ($n_e$) were approximately 5 eV and 2.4 × 1022 $m^{-3}$, respectively [25]. Since the ET-arc has not been characterized by a TS system before, and the PDP is fully equipped to provide simultaneous TS measurements from 11 line-of-sight fiber inputs, the $T_e$ and $n_e$ of the ET-arc at multiple radial positions can be characterized to establish an electron temperature and density profile for the ET-arc, while the TS performance of the PDP is thus validated.

In this paper, the implementation of the TS aspect of the PDP was demonstrated on the 1 ms ET-arc discharge. TS spectra have been obtained from 3 out of 11 line-of-sight fiber inputs of the PDP. And the $T_e$ and $n_e$ of the ET-arc were determined.

## Experimental Design

As shown in Figure 5, the horizontally polarized pulsed Nd:YAG laser at 532 nm was steered to the direction where it can horizontally enter and exit the ET-arc chamber through Brewster's windows, probing the plasma that is 15 mm away from the exit nozzle of the ET-arc source. A lens with a 50 cm focal length was used to focus the laser beam into the plasma. The exit laser beam was steered 90 degrees to a beam dump to reduce possible stray light. The collection optics and the optical fiber bundle for TS were located at the

observation window at the bottom of the ET-arc chamber, while a visible camera (Edgertronic SC1) viewed the chamber through the window meant for digital holography [26], and captured images of the plasma discharge. Spectrometer #2 with a 1800 grooves/mm grating was used to obtain TS light.

During an ET-arc discharge, as illustrated in Figure 6 (a), the plasma travelled from the exit nozzle of the ET-arc source and hit the target plate that was installed on the internal wall of the chamber. simultaneously, the laser beam entered the chamber and interrogated the plasma by TS. The laser and collection optics were aligned in such a way that the beam path of the laser intersected the radial center of the plasma, and the beam path was also on the focal plane of a camera lens for collecting light into the optical fibers at the bottom of the ET-arc chamber, as shown in Figure 6 (b). The image and internal structure of the ET-arc chamber is shown in Figure 7. Both the Thomson scattered light and the plasma emissions were collected into the optical fibers. The optical fiber bundle was a 3-by-11 fiber array. Only a 1-by-11 array (11 fibers arranged horizontally) of optical fibers was instrumented for this TS measurement. Potentially, a 2-by-11 array can be used for simultaneous measurements of TS and OES: one 1-by-11 row for TS, another 1-by-11 row for OES. The fibers were reconfigurable at the fiber panel on the PDP and can be separated into two 11-by-1 arrays (11 fibers arranged vertically along the spectrometer slit), each separately collects TS or potentially OES signal. These two 11-by-1 arrays were then connected to the slits of the spectrometers, achieving 11-lines-of sight of simultaneous TS and OES measurements.

The synchronization of the nanosecond laser pulse with the 1 ms plasma discharge and the camera gating was achieved by the circuit illustrated in Figure 8. The set-up was to have the pulsed laser running on its own 10 Hz internal trigger continuously, and actively synchronize the camera gating and the plasma discharge with the laser pulse. To achieve this, a delay generator was connected to the logic gate output to delay the “go signal” for 100.15 ms, so that the camera and ET-arc waited for the subsequent laser pulse.

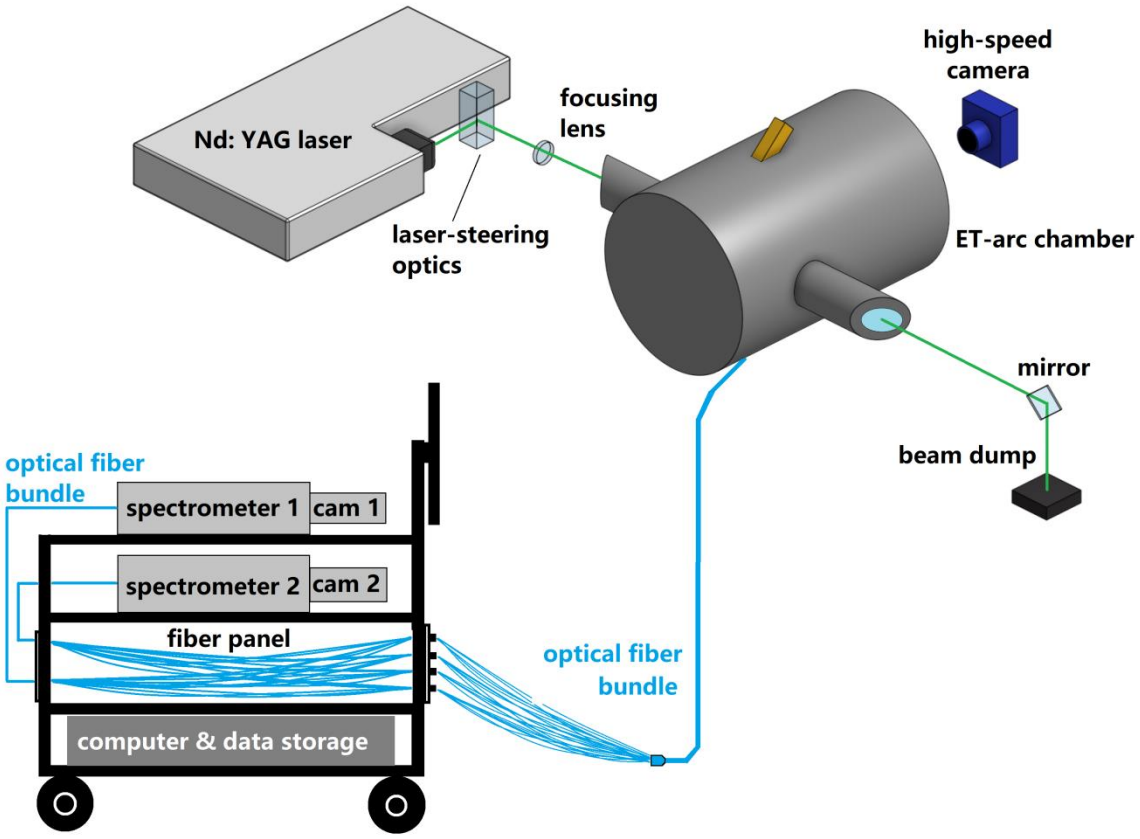


**Figure 5.** Diagram of the full setup of Thomson scattering measurement that characterizes the ET-arc plasma as the proof-of-principle for the PDP system's simultaneous multiple line-of-sights measurement.

**(a)**

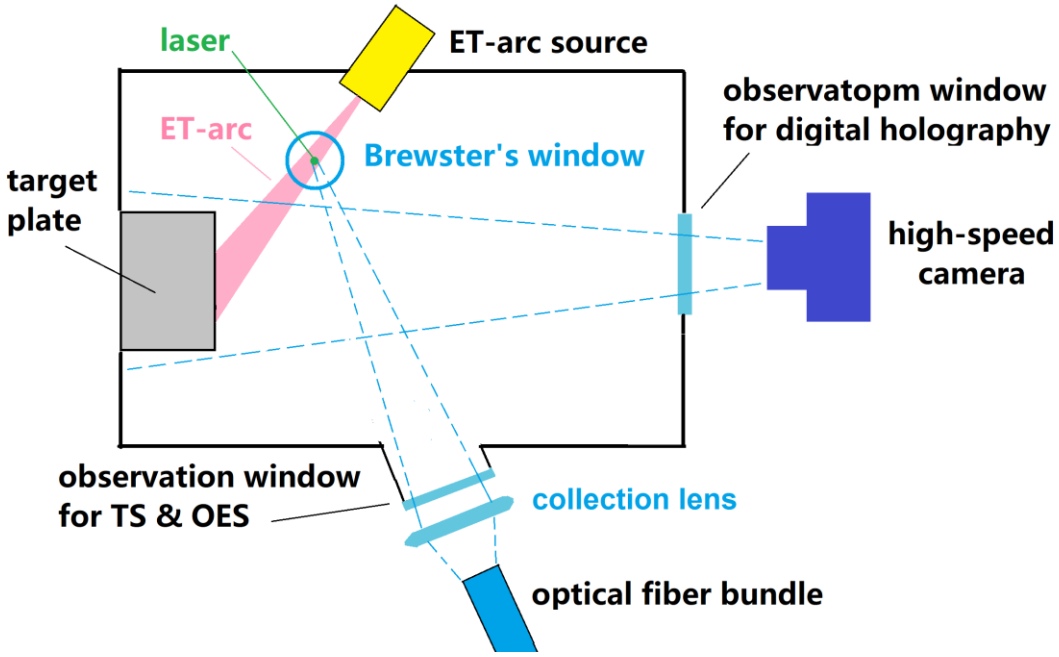


**(b)**

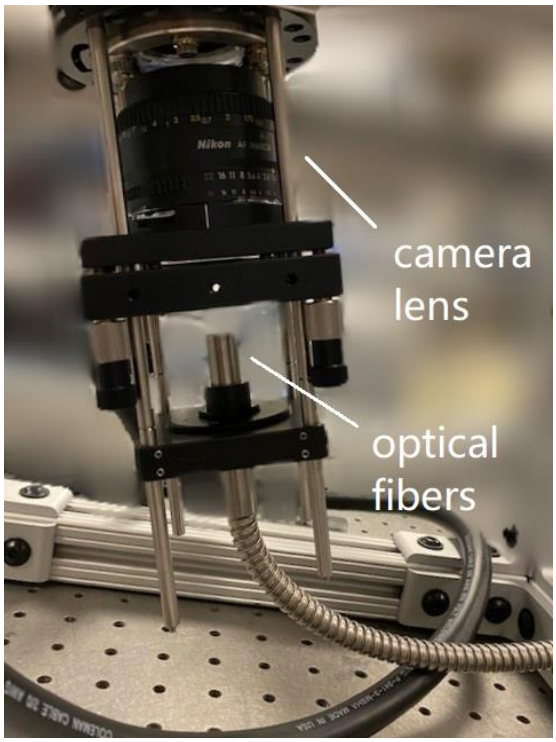


**Figure 6.** (a) A diagram of implementation of PDP on the ET-arc discharge. (b) A photograph of the collection optics and the optical fiber bundle underneath the ET-arc chamber.

**(a)**

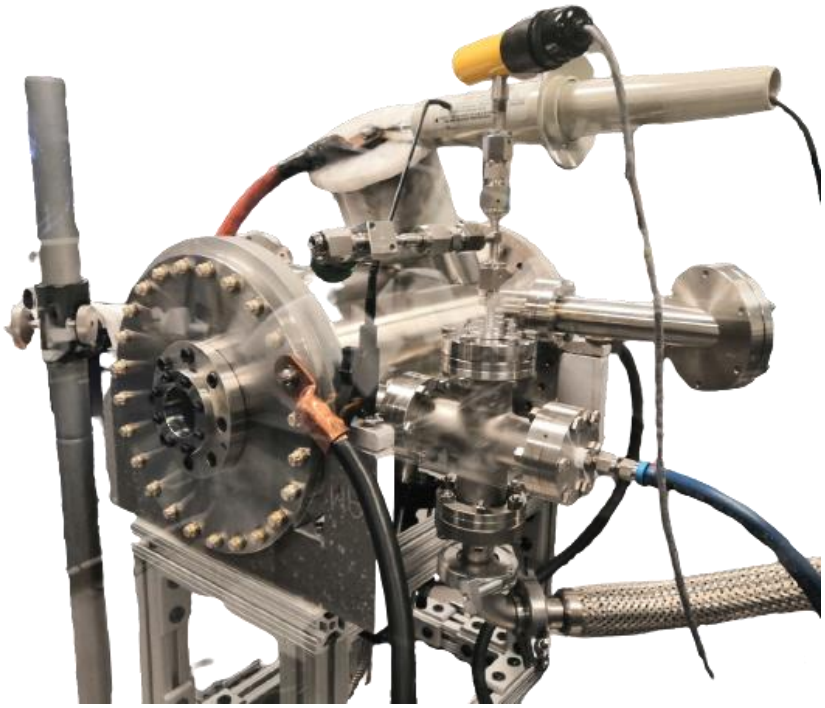

**(b)**

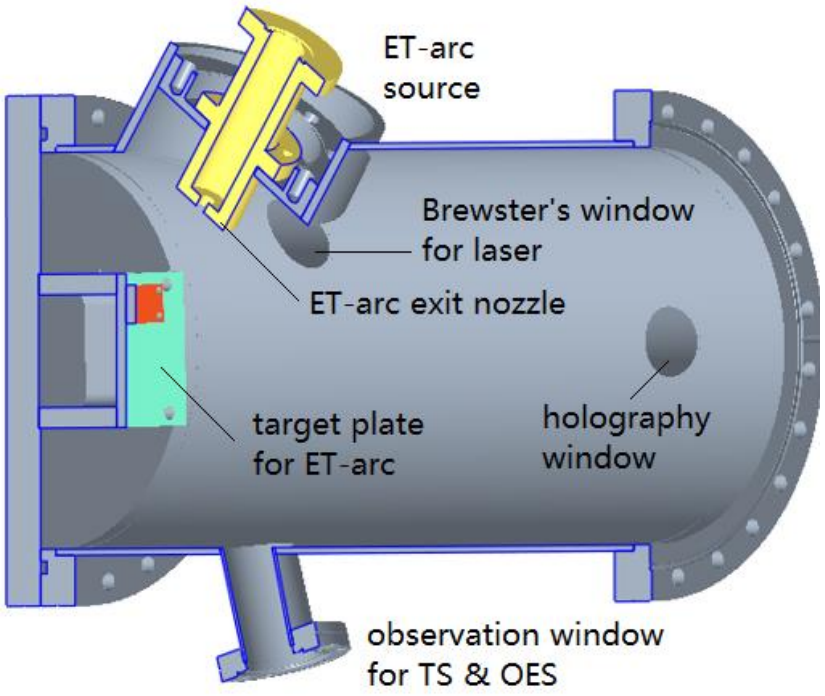


**Figure 7.** (a) A photograph of the ET-arc chamber. (b) A diagram of internal structure of the ET-arc chamber.

**(a)**

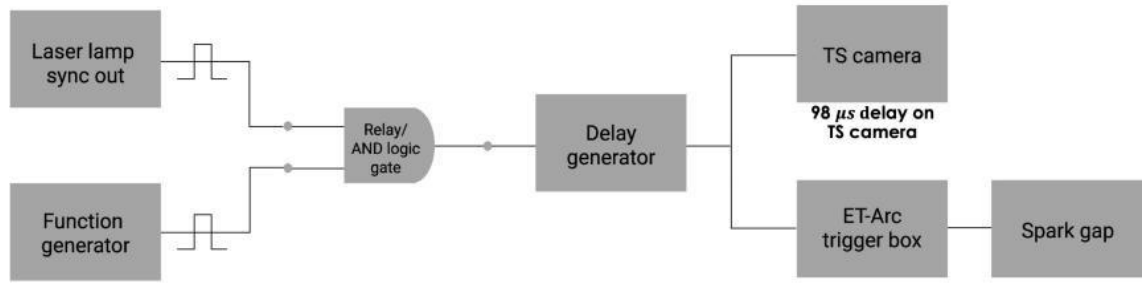


**(b)**

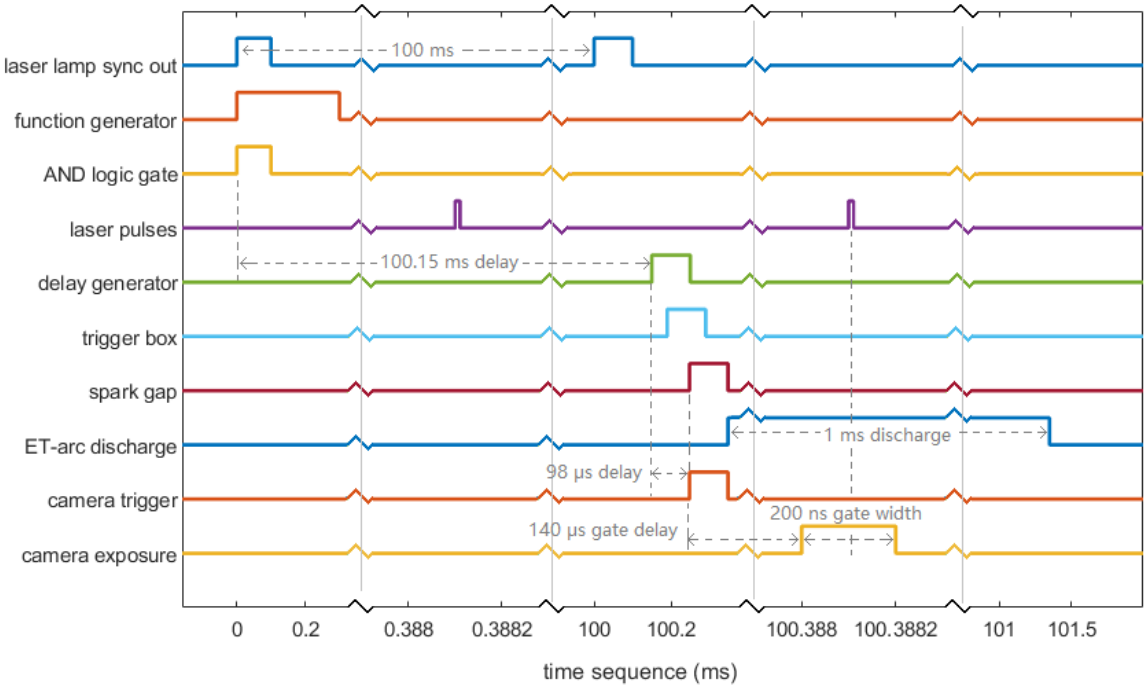


**Figure 8.** (a) Circuitry diagram of the synchronization of laser, plasma and camera. (b) Timing diagram of the signal sequences.

After the delay, the ET-arc trigger box was activated and the spark gap discharged, creating the plasma. In short, once the arc discharge was ready to fire, a trigger signal from the first laser pulse initiated the synchronization process, but the first laser pulse would come in too soon and miss the plasma. So the plasma discharge and the camera exposure were delayed in a well calculated way so they both were synchronized with the next laser pulse.

## Calibration

Rotational Raman scattering (RR) of air at various pressures were conducted prior to TS measurements. The advantages of RR are as follows: RR linearly scales with gas pressure, which can be used for validation of the overall pressure sensitivity of the PDP on ET-arc system. Additionally, RR spectrum can be used to validate the imaging system efficiency due to its feature of numerous Stokes and anti-Stokes lines. Emission intensities of RR and TS are on the similar magnitude, thus obtaining clear and sharp RR spectra indicates the system is sensitive enough for TS. The RR spectrum was also used for absolute calibration of $n_e$. The TS profile based $n_e$ calibration process and $T_e$ calculation have been discussed in Chapter One and in Reference [15] and Reference [20]. Once the system's sensitivity and efficiency have been validated with RR, TS of the ET-arc were obtained with the PDP system.

As the TS signal is weak and difficult to obtain, the efficiency of the imaging system plays a crucial role in obtaining the TS spectrum. To validate the imaging system efficiency, RR of ambient air was conducted as an important validation procedure for TS. The ET-arc chamber was filled with air at atmospheric pressure, laser pulse energy was reduced to avoid optical breakdown, and the RR spectrum was obtained. Figure 9 shows the RR spectrum obtained from the 5th line-of-sight which has the highest SNR, averaged over 300 laser pulses. The well resolved Stokes and anti-Stokes lines indicated good efficiency of the imaging system. And the total emission of the Stokes line at transition $J = 4 \rightarrow 6$ was used for absolute calibration of $n_e$.

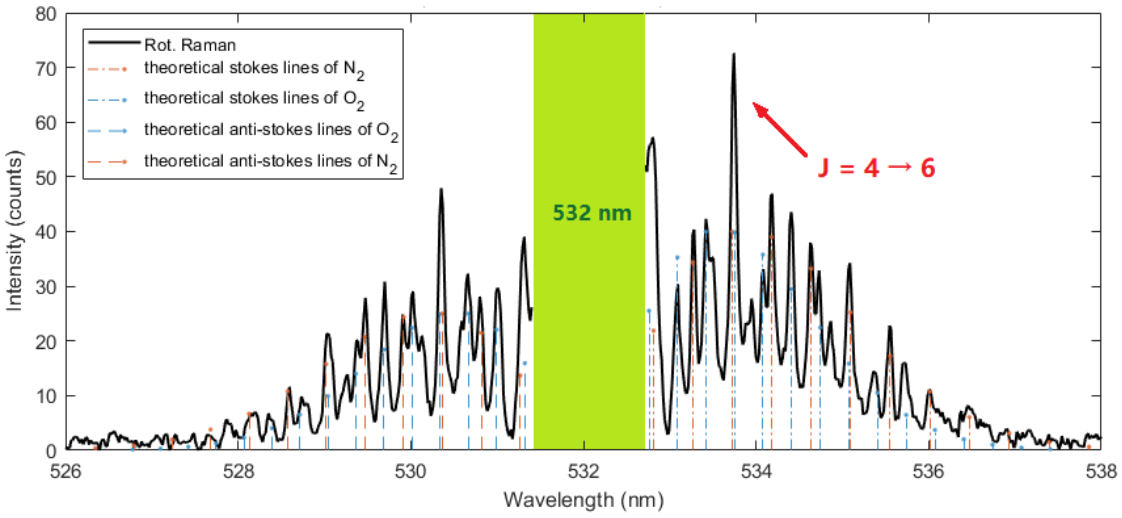


**Figure 9.** Rotational Raman spectrum of atmospheric air obtained with the PDP on ET-arc system. The well resolved Stokes and anti-Stokes lines indicated good efficiency of the imaging system. The lines also match with the theoretical simulation. The total emission of stokes line at transition J = 4→6 was used for absolute calibration of $n_e$.

## Experiment Results

With the system calibrated by RR, TS measurements of the ET-arc plasma were conducted. Figure 10 shows one of the images of the 1 ms ET-arc discharge and a photograph of the plasma-eroded target plate. The image shows a cone of plasma, which is the high intensity area in the image, coming down from the ET-arc nozzle. The target plate is also visible in the image. The elliptical "burn mark" on the target plate surface is the result of erosion by the ET-arc, which indicates the area of impact of the most concentrated portion of the ET-arc plasma. The "burn mark" is also visible in the contrast increased image.

Single-shot TS spectra of ET-arc were obtained. The gate width of the camera was 200 ns, and each TS spectrum was obtained with a single laser pulse probing the plasma when the driving current was at its highest, which was 140 μs after the plasma was triggered, as illustrated in Figure 11.

TS spectra were observed in 3 out of 11 line-of-sight inputs from the optical fibers. These 3 lines of sight captured the emissions at 15 mm downstream (y-axis) from the exit nozzle of the ET-arc source, and radially (x-axis) -5, 0, 5 mm off the axial direction, as illustrated in Figure 12 (a). The corresponding TS spectra and fitted TS profiles are shown in Figure 12 (b).

The $T_e$ calculated from these TS profiles were, respectively, 0.82 ± 0.10, 1.31 ± 0.15 and 0.71 ± 0.08 eV; the $n_e$ that were calibrated with RR were, respectively, (4.36 ± 0.50) x $10^{21}$, (5.86 ± 0.66) x $10^{21}$ and (4.31 ± 0.48) x $10^{21}$ $m^{-3}$, as shown in Figure 13.

**(a)**

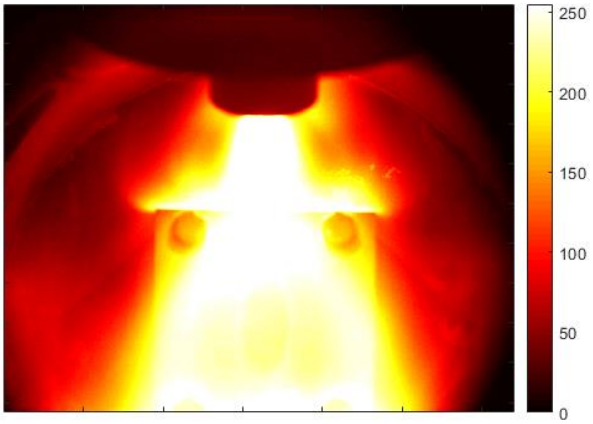


**(b)**

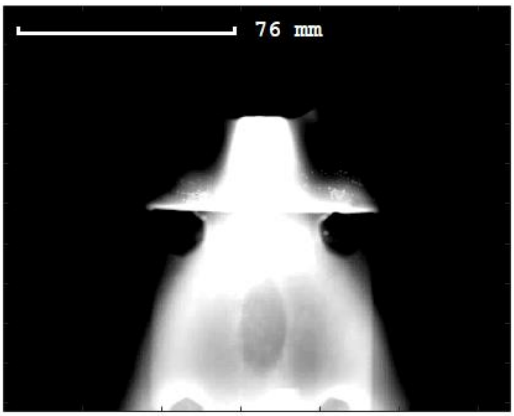


**(c)**

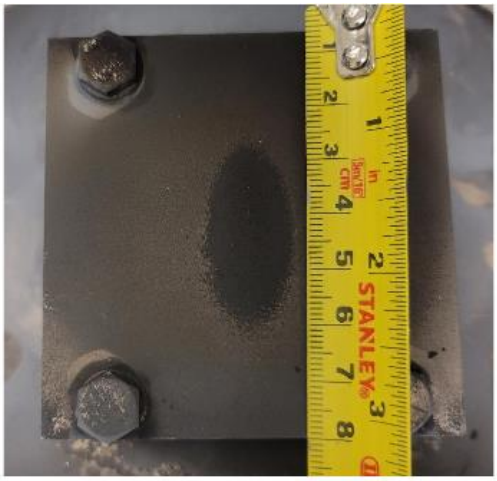


**Figure 10.** (a) An artificially colored image of the ET-arc discharge taken by the high-speed camera. (b) The same image with higher contrast makes the "burn mark" on the target plate visible. (c) A photograph of the plasma-eroded target plate.

**(a)**

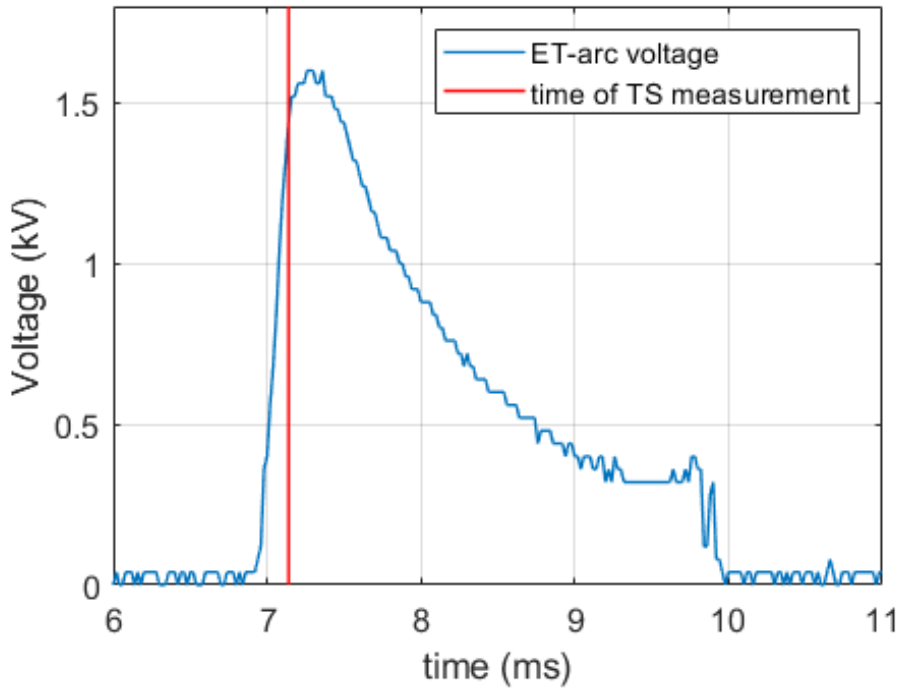


**(b)**

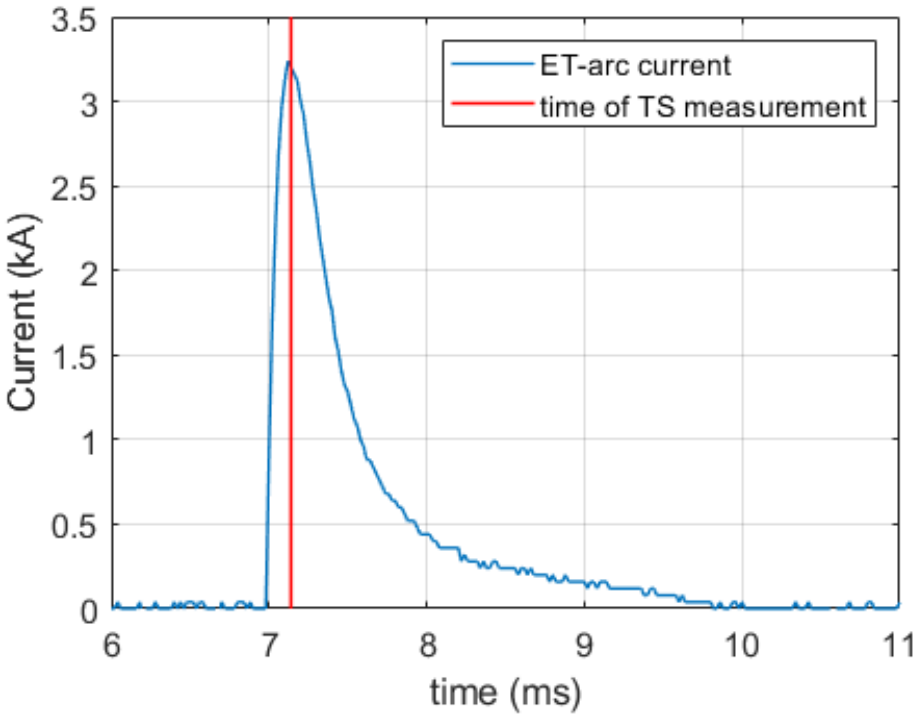


**Figure 11.** The measured (a) voltage and (b) current during a 1 ms ET-arc discharge. The red solid line marks the time when TS was conducted.

**(a)**

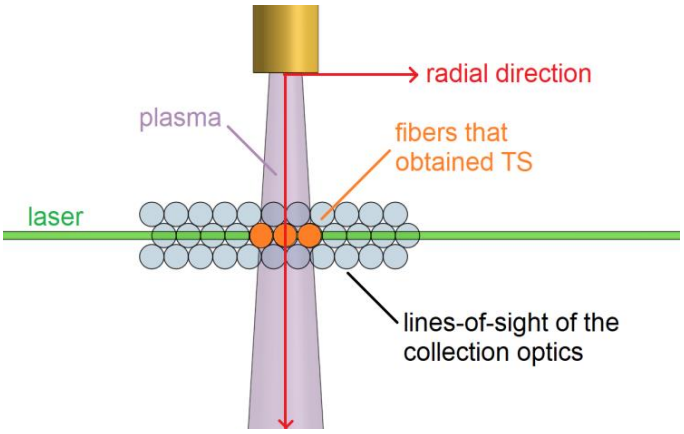


**(b)**

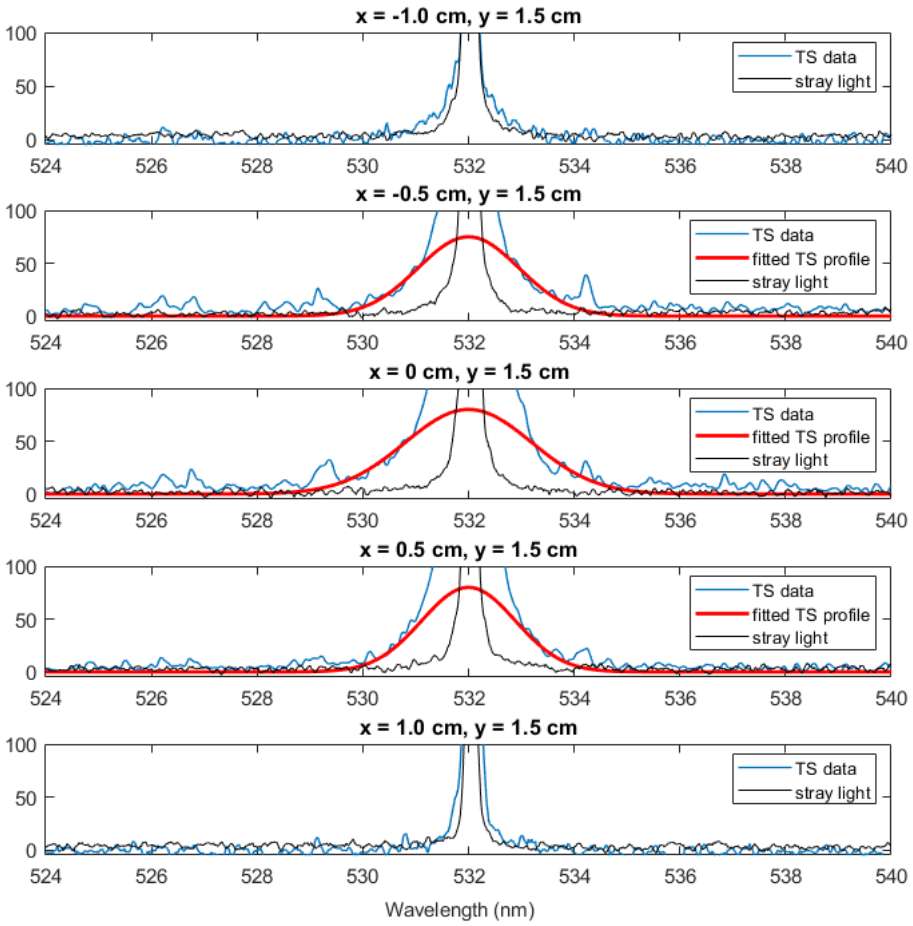


**Figure 12.** (a) A diagram illustrating the fibers that collected TS spectra. The 3 lines of sight that were spatially interrogating the ET-arc were radially (x-axis) -5, 0, 5 mm off the axial direction. (b) The TS spectra from the 5 lines-of-sight fiber inputs, and 3 middle ones have obtained TS.

**(a)**

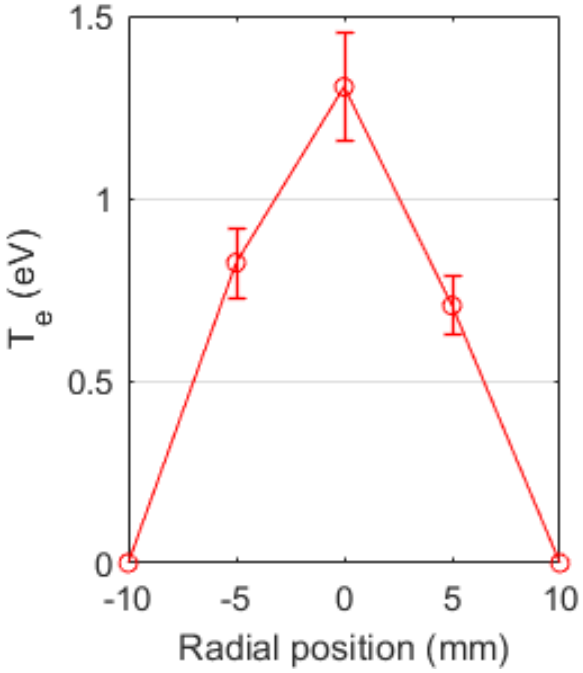


**(b)**

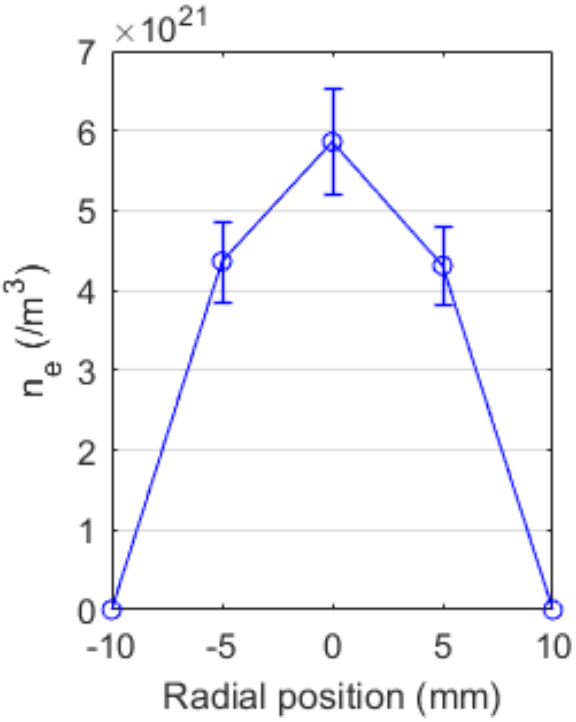


**Figure 13.** (a) The calculated $T_e$ from the 3 line-of-sight inputs and (b) the calculated $n_e$ from the 5 lines-of-sight inputs.

## Summary

Motivated by the concept of a modular Thomson scattering diagnostic system, the PDP has been developed at ORNL to provide the ability to measure several fundamental plasma parameters in one transportable package. As proof-of-principle demonstration, the PDP has been implemented on an electrothermal arc source to measure the electron temperature and number density of a Helium plasma using a laser Thomson scattering diagnostic. Rotational Raman scattering of atmospheric air have been conducted to validate the system sensitivity and efficiency. Thomson scattering and plasma emission spectra from multiple lines-of-sight fiber inputs were obtained. Previous optical emission and collisional radioactive model based studies on that plasma suggested the electron temperature of the plasma was 5 eV and electron number density was $2.4 \times 10^{22}$ $m^{-3}$. Thomson scattering from the PDP measured $0.82 \pm 0.10$, $1.31 \pm 0.15$ and $0.71 \pm 0.08$ eV and $(4.36 \pm 0.50) \times 10^{21}$, $(5.86 \pm 0.66) \times 10^{21}$ and $(4.31 \pm 0.48) \times 10^{21}$ $m^{-3}$ from 3 line-of-sight fiber inputs, respectively. The variation in plasma parameters between the TS measurements and the previous CRM estimation could be due to both the different locations of the measurements and the different geometry of the ET-arc source between the TS and OES measurements.

## Acknowledgement

This project is supported by Advanced Research Projects Agency-Energy (ARPA-E) under the U.S. Department of Energy. Contract No. DE-AC05- 00OR22725.

# CHAPTER THREE
# PULSE-BURST LASER-BASED 10 KHZ THOMSON SCATTERING MEASUREMENTS

A version of the contents in this chapter was presented on The Southeastern Section of the American Physical Society (SESAPS) Conference in 2018 and The American Institute of Aeronautics and Astronautics (AIAA) SciTech Conference in 2020, and published on Plasma Science and Technology.

Thomson scattering (TS), as a popular and reliable diagnostic technique, has successfully measured electron temperatures and electron number densities of plasmas for many years. However, conventional TS techniques using Nd:YAG lasers operate only at tens of Hertz. Here, we present the development of a high-repetition-rate TS instrument based on a high-speed, pulse-burst laser system to greatly increase the temporal resolution of measurements. Successful instrument prototype testing by collecting TS light from laboratory helium and argon plasmas at 10 kHz, was carried out. Calibration of the instrument detection sensitivity using nitrogen/oxygen rotational Raman scattering signal is also presented. Quantitative electron number densities and electron temperatures of the plasma were acquired at 10 kHz, for stable plasma discharges as, respectively, ~0.9 eV and ~5.37 × $10^{21}$ $m^{-3}$ for the argon plasma, and ~1 eV and ~ 6.5 × $10^{21}$ $m^{-3}$ for the helium plasma.

## Introduction

Laser Thomson scattering (TS) is a standard technique for diagnosing plasmas in high-energy-density physics experiments. TS is historically the most reliable diagnostic method for providing detailed and simultaneous profiles of the local electron density and temperature. This non-intrusive technique has been found to be well suited to magnetically and inertially confined plasmas, where geometrical constraints put restrictions on the use of other techniques [27-30]. Experiments in plasmas with electron densities in the range of $10^{13} < n_e < 10^{21}$ $cm^{-3}$ and electron temperatures in the range of 1 eV < Te < 5 keV are now

being performed. Recent attempts have been made to lower the detection limit for TS measurements to below $10^{12}$ $cm^{-3}$ [31, 32]. TS is one of the key diagnostics used in modern tokamaks and use of this technology is planned in future facilities such as the ITER project.

Conventional TS systems can only obtain sparse temporal data points per discharge cycle due to their low diagnostic sampling rates. This can significantly limit the ability of real-time systems for the critical detection of highly transient plasma instabilities, such as edge-localized modes (ELMs). Conventional TS diagnostic designs utilize a 10–50 Hz solid-state Nd:YAG pulsed laser to probe target plasmas [33, 34]. The light scattered by the electrons is collected by a set of lenses, often with a radial array of optical fibers, and then transferred into a polychromator or spectrometer. Some approaches to improve the temporal and spatial resolutions of TS systems have utilized multiple observation ports and paths. The collection of sub-nanosecond (sub-ns) time-resolved TS signals for a total time of 7 ns was achieved by establishing two observation angles (90° and 30°) [35]. A similar ns-level TS technique has been developed by splitting the incident laser beam into two paths [36]. One of the paths was delayed with respect to the other by 3 to 14 ns. Other multi-pass techniques include a dual-pass technique in which the arrangement allows the laser beam to pass through the plasma for a second time in a different location [32]. Although these multi-pass and multi-angle TS techniques have achieved nanosecond-level temporal resolution, only a handful of data points may be obtained in each laser cycle.

To better understand and predict plasmas, TS at much faster sampling rates (e.g. 1 kHz or higher) is in demand. High temporal resolution TS data will provide greater detail on plasma behavior than that is presently available and could therefore aid the development and improvement of plasma control systems through its advancement of diagnostic capability. To achieve this, a straightforward laser cluster has been successfully demonstrated [37, 38]. Multiple lasers at 10–50 Hz are operated in sequential or burst modes to increase the data acquisition rates, i.e., to obtain a few pulses at higher repetition rates. Example specifications include 30 pulses at 1 kHz, 4 pulses at 20 kHz, or 6 pulses at 13 kHz, etc [38]. However, number of high-repetition-rate pulses from the laser cluster is

limited. Hence it remains challenging for utilization of high-speed TS to track fusion plasma dynamics.

In this paper we have demonstrated a viable pulse-burst laser-based highly time-resolved TS diagnostic technique operating at 10 kHz. The principal components of the system are a 0.3 m spectrometer, a high-speed electron-multiplying CCD (EMCCD) camera, and a pulse-burst laser. As suggested in references [39-41], the pulse-burst laser can provide the required high-energy laser pulses at high repetition rate for high-speed TS measurements. The pulse-burst laser was originally developed for supersonic or hypersonic flow diagnostics. It has a high pulse repetition frequency with an output only limited by the heat capacity of the laser medium. Instead of undergoing continuous cooling like conventional pulsed lasers, pulse-burst lasers operate until the heat capacity reaches a maximum acceptable temperature; at this point they are shut off and aggressively cooled before the next cycle. Each cycle fires a train of high-energy laser pulses at a high repetition rate over a short period of time.

The pulse sequence of a pulse burst laser can reach energies of ~100 mJ per individual pulse at up to MHz rates, or ~1 J per individual pulse at up to 10 kHz rates, while maintaining low average power. This technology has been demonstrated for high-speed measurements of temperature [39] and mixture fraction [40], as well as planar laser-induced florescence (PLIF) detection of OH [41], NO [42, 43], CH [44, 45], and $CH_2O$ [46] molecular entities. Raman line imaging of $O_2$, $N_2$, $CH_4$, and $H_2$ [47], with measurement rates ranging from 1 kHz to 1 MHz has also been achieved with this laser. Furthermore, some pulse-burst laser systems have recently been adopted for high-speed TS plasma diagnostics in fusion devices, namely the Madison Symmetric Torus (MST) [48] and National Spherical Torus Experiment Upgrade (NSTX-U) [49].

# Experimental Setup

***Pulse-burst laser for Thomson scattering experiment***

A schematic of the pulse-burst laser used in the high-speed TS experiment is illustrated in Figure 14. The architecture of the burst-mode laser system has been discussed in detail elsewhere [50]; therefore, here we only describe the details of obtaining elongated pulses using an acousto-optic modulator (AOM). The flexible master oscillator of the long-pulse burst-mode laser produces tunable pulse widths by slicing the output of a 1064 nm (vacuum wavelength), 30 mW continuous-wave (CW), narrow-band diode laser. Pulse slicing is achieved using a >10 GHz bandwidth, fiber AOM with a >50 dB extinction ratio. The AOM is modulated by a pulse generator that is able to generate pulses with 10 ns rise and fall times and adjustable durations that are controlled using software. Utilization of the AOM-based pulse slicer allows tunable pulse durations over a range wider (10-1000 ns) than what is possible with only a conventional beam-splitter-based optical pulse stretcher (typically ~100 ns). The sliced 1064 nm pulse train is amplified to 10 W peak power in a ytterbium fiber amplifier. Then, the pulses are further amplified in a series of Nd:YAG amplifiers. The final laser output can reach ~2.3 J/pulse at 1064 nm or 1.35 J/pulse at 532 nm, with a repetition rate of 10 kHz and a burst duration of 10 ms. The laser energy fluctuates about 3%.

If the laser energy density is sufficiently localized in the volume of the discharge chamber, then the residual neutral gas can spontaneously break down to form a plasma. To avoid optical breakdown in the laboratory plasma vacuum (or other weakly ionized plasma formation), the laser pulses are stretched to 70 ns. Figure 15 shows the temporal profiles of the burst-mode-laser output at the 1064 nm fundamental wavelength, with various pulse durations from 100 ns to 1000 ns achieved by adjusting the AOM slicing time. In contrast to multiple-peak pulse stretching using delay lines, the temporal profiles of the AOM output pulses have Gaussian-like shapes, with a slightly longer trailing tail, particularly at longer pulse durations. This is due to the gain-depletion effect of the laser system.

**(a)**

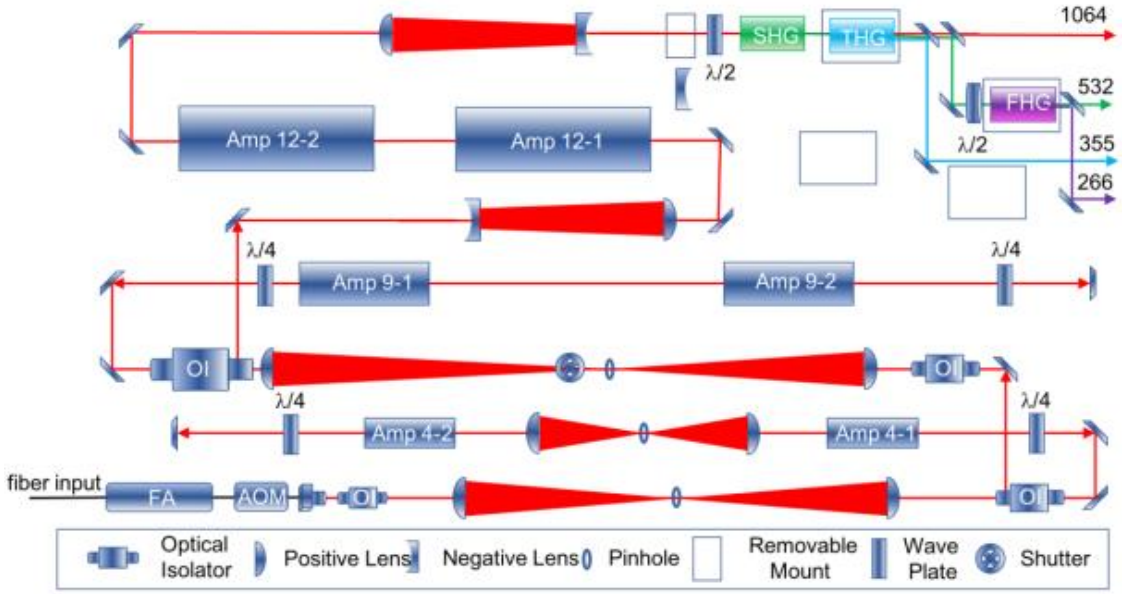


**(b)**

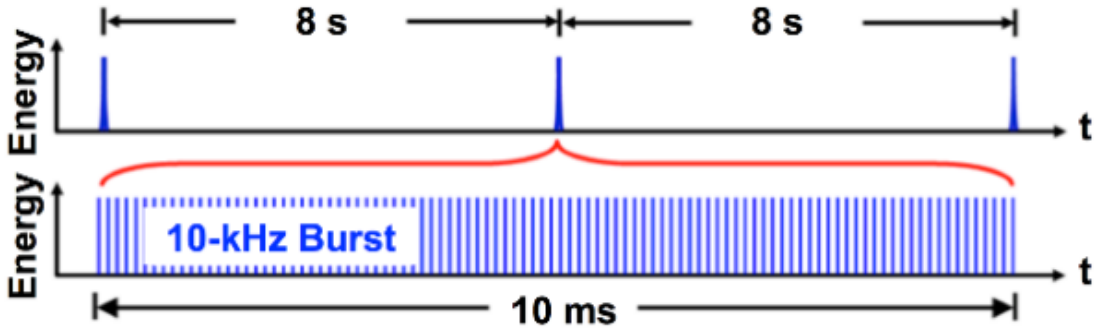


**Figure 14.** (a) Schematic diagram of the pulse-burst laser used in this experiment. (b) Details of the pulse burst, indicating the 10 kHz repetition rate, 10 ms burst duration, and 8 s interval between sequential burst trains.

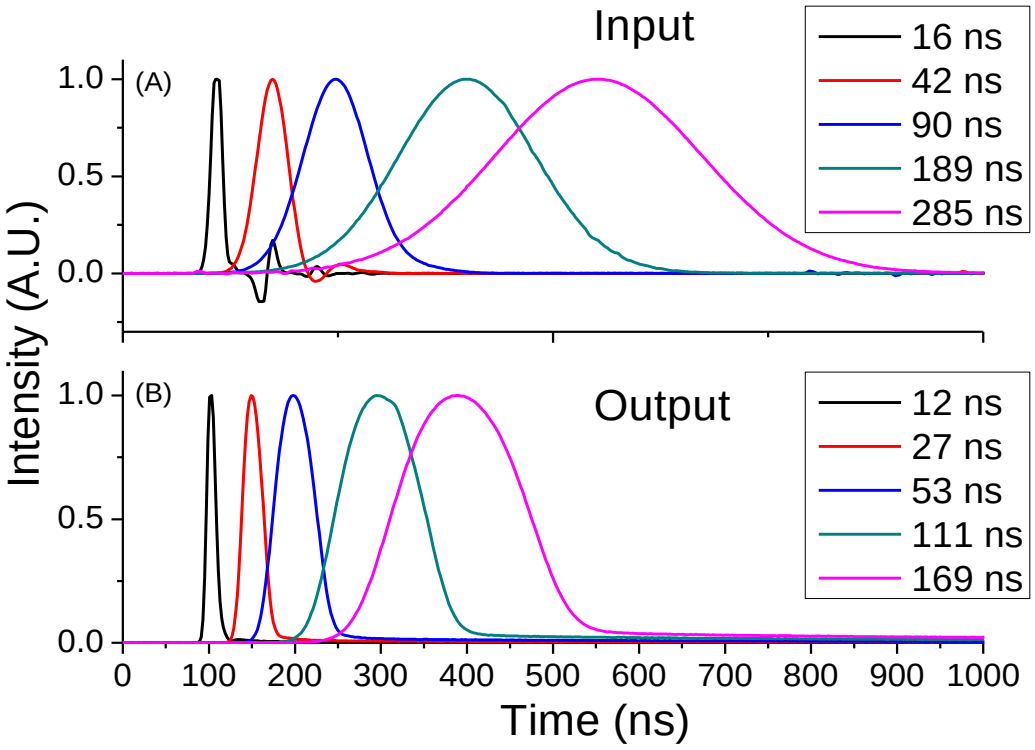


**Figure 15.** Experimental characterization of the stretched laser pulses. Temporal profiles of laser pulses with various duration measured (top plot) immediately after the AOM pulse slicing and (bottom plot) the same pulses after subsequent amplification steps.

**(a)**

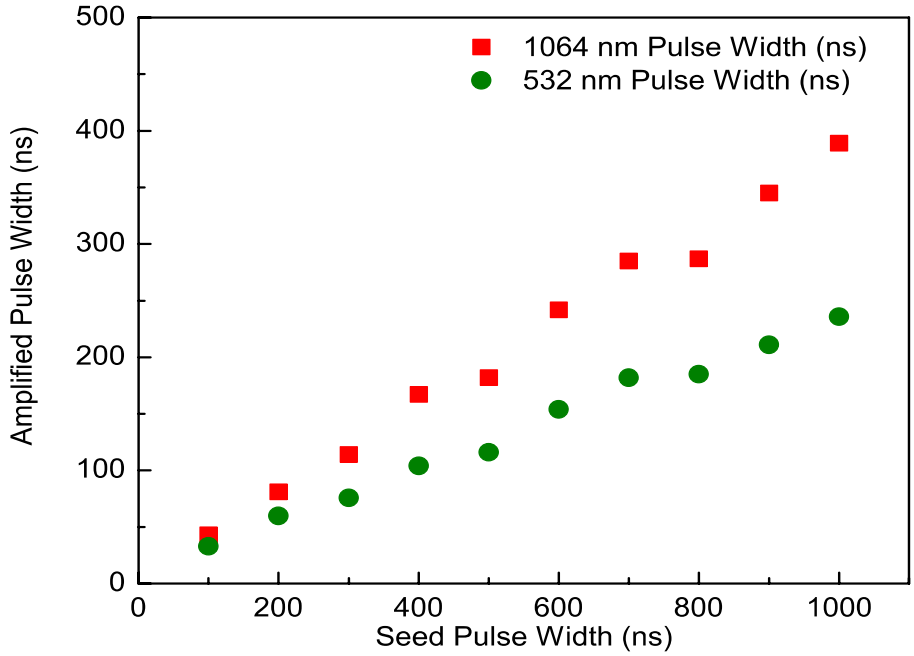


**(b)**

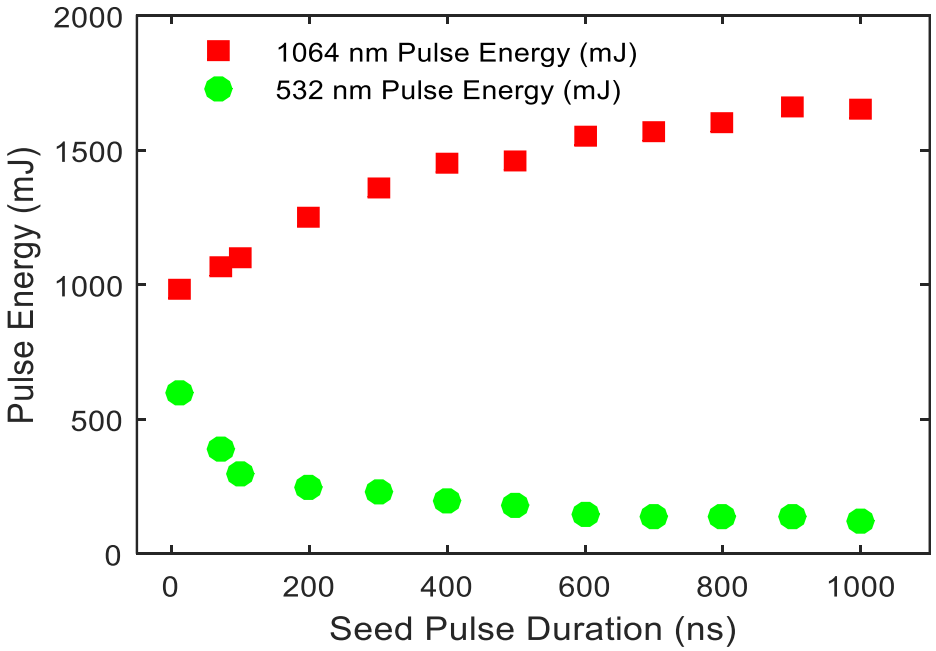


**Figure 16.** (a) Laser pulse widths of AOM-sliced pulses: before v.s. after subsequent amplification. (b) Laser pulse energies for pulses of different widths.

Figure 16 reveals that the final laser output at 1064 nm has shorter pulse widths than those of the initial AOM slicing because of a gain-narrowing effect during pulse amplification. For example, with a 100 ns AOM slicing time, the final laser pulse duration after all of the amplification steps is ~70 ns (FWHM), and when the initial AOM pulse is 500 ns or 1000 ns, the final high-power laser pulse duration is shortened to ~200 ns or ~300 ns, respectively. Further pulse-width stretching (up to several μs) is also possible with the current method, and these results will be discussed elsewhere. Both pulse width and repetition rates can be controlled by the software.

***Thomson scattering setup for laboratory plasma***

The TS system for a laboratory plasma test setup is shown in Figure 17. The vacuum cell was constructed to generate the plasma, with two quartz windows for laser propagation and one quartz side window to collect the Thomson-scattered photons. Both windows for laser propagation were constructed at the Brewster angle of 56.2° to remove the reflection of the incident laser beam, which could otherwise illuminate the electrodes and contribute a strong background photon noise. Other measures to remove noise from stray light were the installation of shields around the camera lens and software background subtraction. To reduce overheating of the positive electrode, a pair of Swagelok Torr seals were used to seal off and isolate the connections between the electrodes and the vacuum cell, as well as sustain the high temperature. Further, external forced-air cooling was used to delay the overheating of the positive electrode during the experiment. Figure 18 shows photos of the setup and the table-top argon plasma glowing in the dark.

The generation of the laboratory plasma is affected by the applied electric voltage, the pressure inside the vacuum cell, the ballast resistor, and the distance between the electrodes. The power of the DC generator was set to 1 kV, 400 mA, and the pressure inside the cell was around 35 Torr. A notable detail is the trade-off between the distance between the electrodes and plasma stability: if the electrodes are too far apart, the plasma will be weak and unstable; if the electrodes are too close, then the plasma will expand to occupy a

stable, large ball-like space (due to the gradient of the medium resistance), which will also weaken the electron density of the plasma, albeit also reducing the plasma electron density.

The TS system includes a 532 nm pulse-burst laser, a 0.3 m spectrometer (Princeton Instrument PI 2300i), an EMCCD high-speed camera (Princeton Instrument ProEM HS 1024B), and a set of lenses and mirrors. Each 10 ms burst of the laser consists of 100 pulses (500 mJ/pulse) at a repetition frequency of 10 kHz. The laser beam was focused by a convex lens with a focal length of 1 m. The spatial resolution is limited by the laser beam focus, which is about 1 mm in length and 100 μm in diameter. The table-top plasma was generated between two pin electrodes, to which was applied a high DC voltage, inside the vacuum cell. The plasmas were generated in either helium or argon. TS from plasmas occurs under controlled pressures and electric currents. The TS signal was first collected by a lens behind the central window on the vacuum cell, and then directed to the slit on the spectrometer, and detected by the high speed EMCCD camera. The "spectra-kinetics" mode of the EMCCD can capture the TS spectra at a rate of 10 kHz with a quantum efficiency of ~90% near 532 nm.

## Experimental Results

***Calibration of 10 Hz Thomson scattering by rotational Raman scattering***

To validate and calibrate the high-speed Thomson scattering detection system, experiments using a 10 Hz Nd:YAG laser were conducted. First, Rayleigh scattering was used to calibrate the spectrometer's central wavelength. Rotational Raman scattering from ambient air (295 K, 750 Torr) was obtained to calibrate the overall optical detection system, including the wavelength registration and detection efficiency. The calibration was later used for absolute measurements of electron number density of argon plasmas obtained using the 10 Hz laser.

Figure 19 (a) shows a rotational Raman scattering spectrum obtained by averaging over 300 exposures. Lines in both the Stokes and anti-Stokes branches of $N_2$ and $O_2$ are apparent in the spectrum.

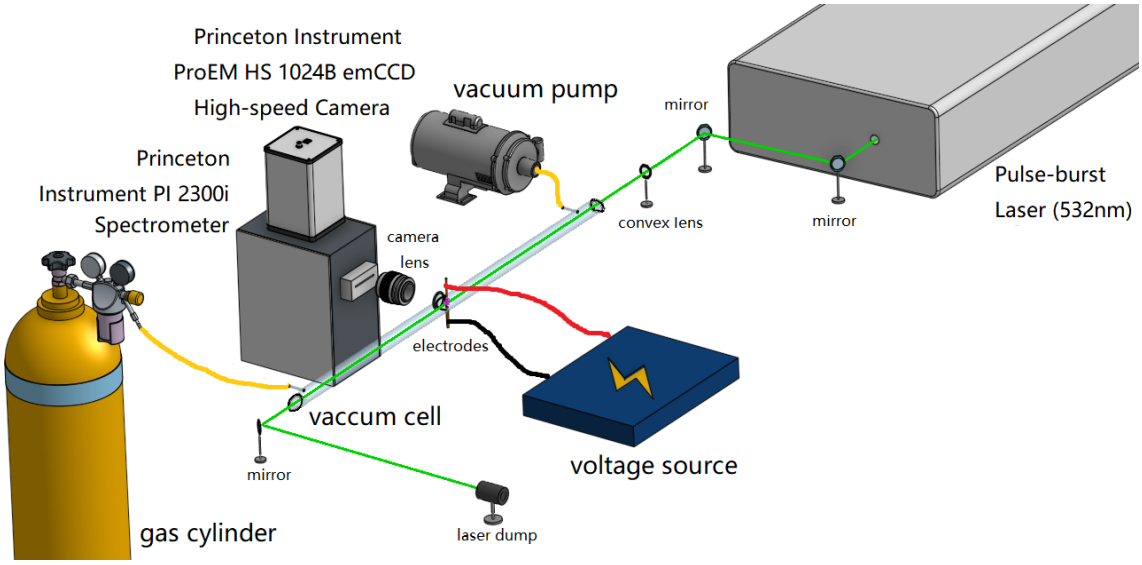


**Figure 17.** A diagram of the Thomson scattering system, including a pulse-burst laser, spectrometer, EMCCD high-speed camera, and a set of lenses and mirrors. The plasma was generated inside the vacuum cell, while the TS signal was collected at the side window on the vacuum cell and detected by the high-speed EMCCD camera.

**(a)**

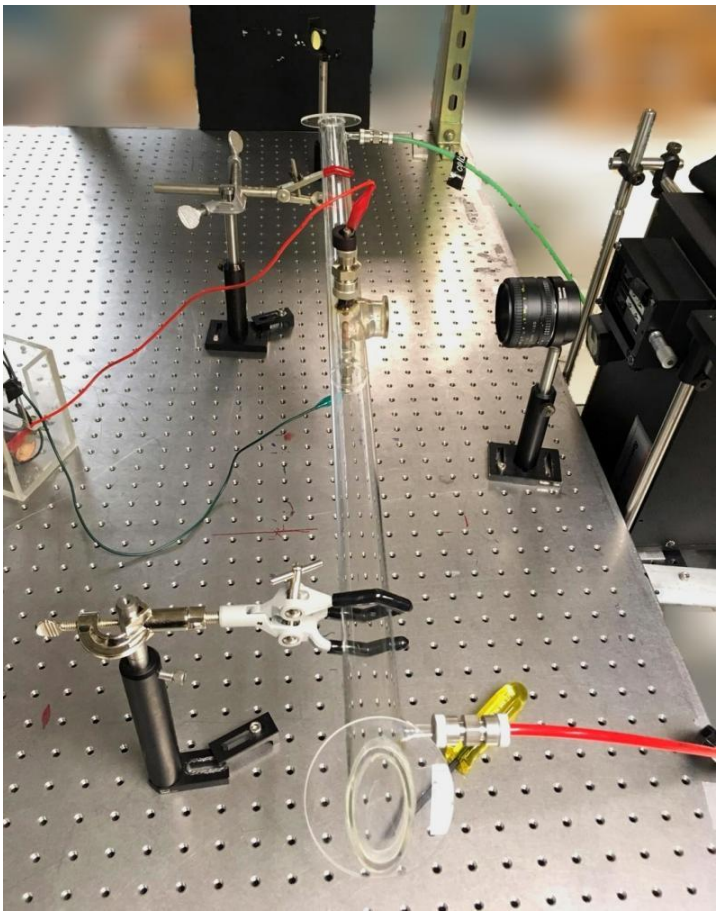

**(b)**

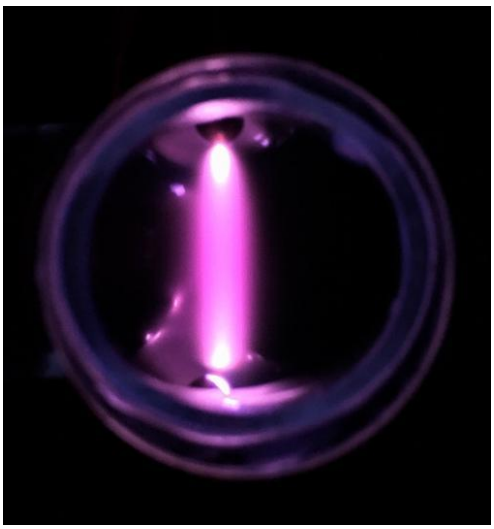

**Figure 18.** (a) A photo of the experimental setup for the table-top argon plasma. (b) A photo of the argon plasma taken in the dark.

**(a)**

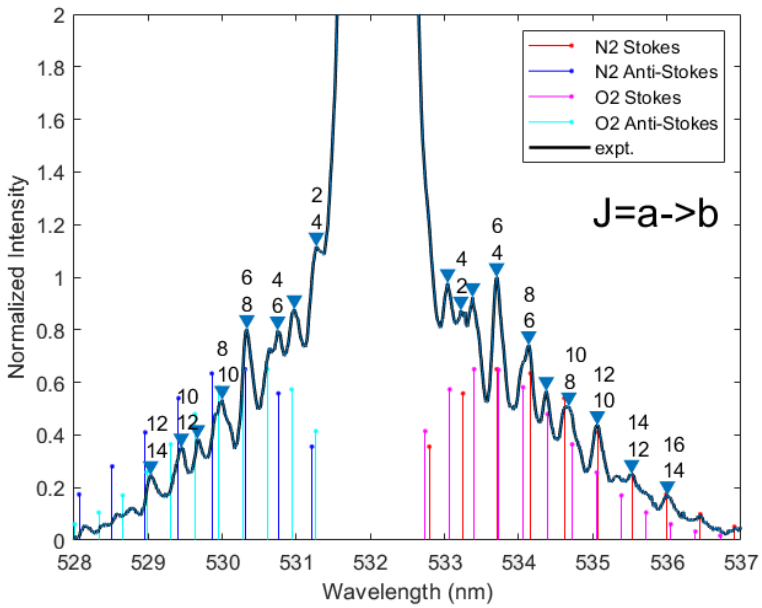


**(b)**

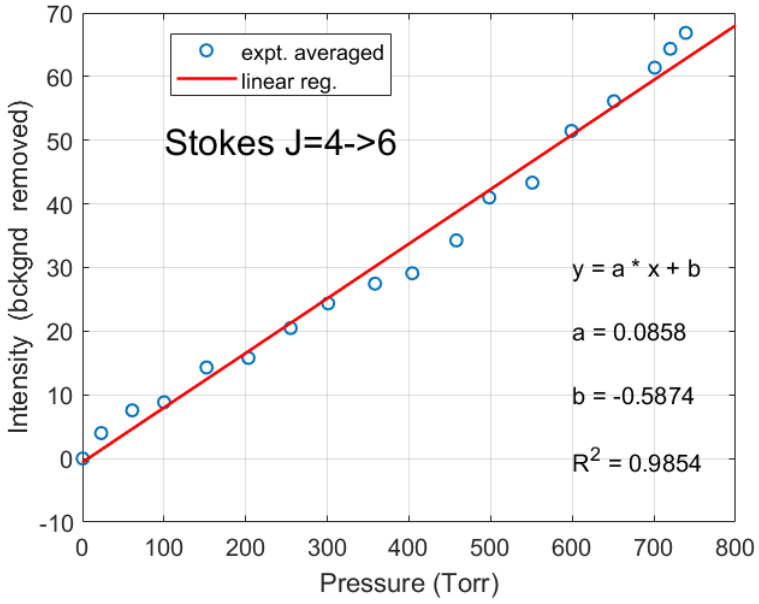


**Figure 19.** Rotational Raman scattering of ambient air. (a) Rotational Raman spectrum; the straight lines in the figure are mathematically generated locations of Stokes and anti-Stokes lines for $N_2$ and $O_2$ that match peaks in the experimental spectrum, and the numbering above the peaks indicates the $N_2$ Stokes and anti-Stokes transitions. (b) Intensity of the $N_2$ J = 4→6 (Stokes branch) transition lines at various pressures.

The straight lines in the figure are mathematically generated locations of Stokes and anti-Stokes lines for $N_2$ and $O_2$, and these agree well with the experimental measurement. Peaks marked with numbers indicate Stokes and anti-Stokes transition levels for $N_2$. Figure 19 (b) shows the scaling of the relative intensity of the $N_2$ J = 4→6 transition measured at various pressures from a few Torr to 750 Torr. A linear regression of the Raman peaks with pressure gave an $R^2$ value of 98.5%, indicating good alignment and efficiency of the detection system. The calculation of electron temperature and electron number density have been discussed in Chapter One (see Equation 5 & 6). Thomson scattering in argon plasmas was conducted with a 10 Hz pulsed laser (100 shots average) under various conditions. As shown in Figure 20, the discharge conditions of the displayed example measurement were 1 kV, 400 mA DC, and 60 Torr of argon. Electron temperatures were computed and electron number densities were calibrated in accordance with the rotational Raman scattering spectrum shown in Figure 19 (a). The single-shot spectra acquired using the 10 Hz pulsed laser proves the concept of obtaining a TS spectrum per pulse as well demonstrates the sensitivity of the instrument by its capacity to generate such a spectrum.

***Demonstration of 10 kHz Thomson scattering in a laboratory scale plasma***

After completion of TS detection system calibration, the 10 Hz pulsed laser was then replaced by a 10 kHz pulse-burst laser for high-speed measurements. Before making TS measurements, rotational Raman scattering of ambient air (750 Torr) was again conducted for system realignment and calibration of absolute measurements of electron number density, which were subsequently performed for the argon and helium laboratory plasma test setup.

Stokes and anti-Stokes lines are visible in the rotational Raman scattering spectrum obtained using the 10 kHz pulse-burst laser, as shown in Figure 21. Compared to the spectrum shown in Figure 19, the change of spectral shape of rotational Raman scattering near the Rayleigh band (at 532 nm) was created by a physical block placed between the EMCCD camera and the output of the spectrometer.

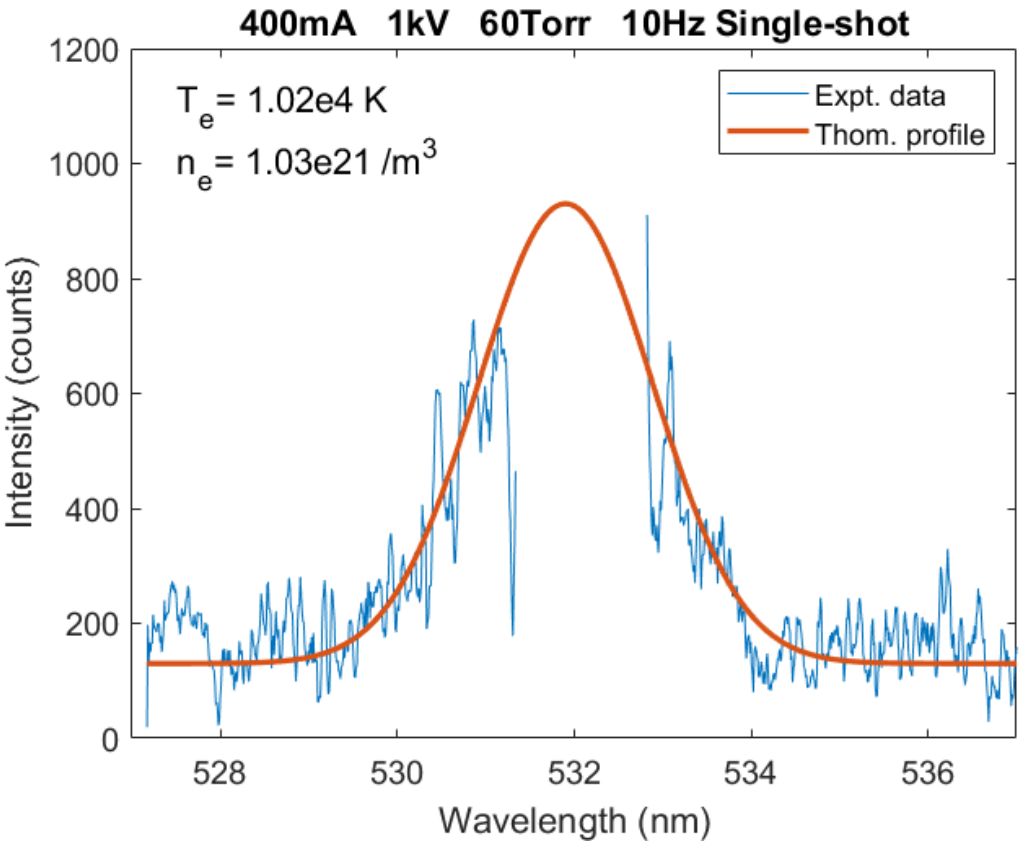


**Figure 20.** An example calibrated spectrum of single-shot Thomson scattering measurements of laboratory argon plasma using a 10 Hz pulsed laser. Experimental condition: argon gas pressure at 50 Torr, DC discharge current at 400 mA and voltage at 1 kV.

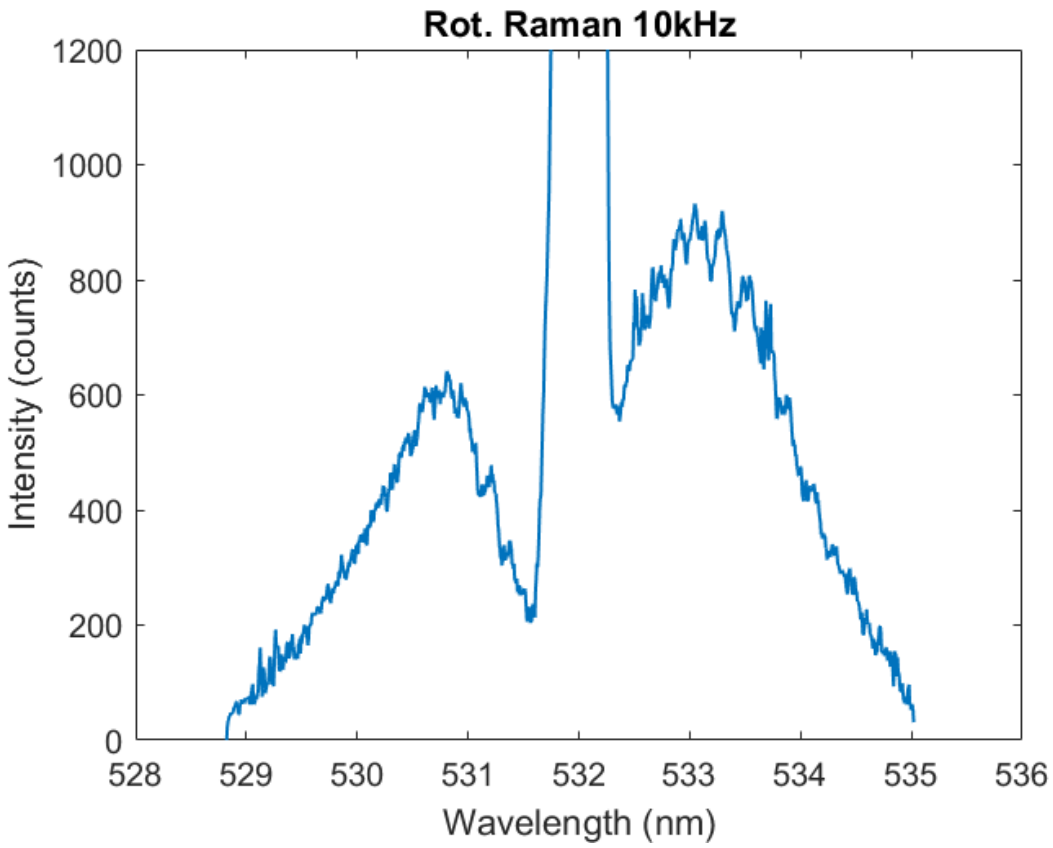


**Figure 21.** Single-shot Raman scattering spectrum of ambient air at 750 Torr captured by our high-speed TS system.

This block was inserted to remove Rayleigh scattering from the spectrum but was able to completely block Rayleigh scattering. Next, a 400 mA, 1 kV DC power was applied to the electrodes to generate a plasma inside an argon-filled vacuum cell where the internal pressure was 33 Torr.

Figure 22 shows a single-shot TS spectrum of the argon plasma captured by the high-speed TS system. The pulse-burst laser parameters were set to ~500 mJ/pulse at 532 nm at 10 kHz. From the Thomson profile, the electron temperature was computed. As for absolute electron number density, we assumed the pulse energy fluctuation pattern in each burst of the pulse-burst laser is constant (pulse-to-pulse fluctuation is less than 5% during the 10 ms burst), and therefore, we calibrated the electron number density in each frame using the corresponding frame of the previously obtained Raman scattering spectra (Figure 21).

Figure 23 illustrates the variation in the resultant electron temperatures and electron number densities of the argon plasma over time. The mean electron temperature and mean electron number density are ~0.88 eV ($1.03 \times 10^4$ K) and $5.37 \times 10^{21}$ $m^{-3}$, respectively.

As helium is more easily ionized than argon, the vacuum cell was then refilled with helium, and TS spectra of helium plasma generated by a 400 mA, 1 kV DC power at 37 Torr were obtained. Figure 24 displays the TS spectral profile, the electron temperature as well as the electron number density was computed.

Furthermore, Figure 25 illustrates the fluctuations in the obtained electron temperatures and electron number densities. The electron temperature oscillates around 1.02 eV ($1.18 \times 10^4$ K), and the absolute electron number density fluctuates around $6.45 \times 10^{21}$ $m^{-3}$.

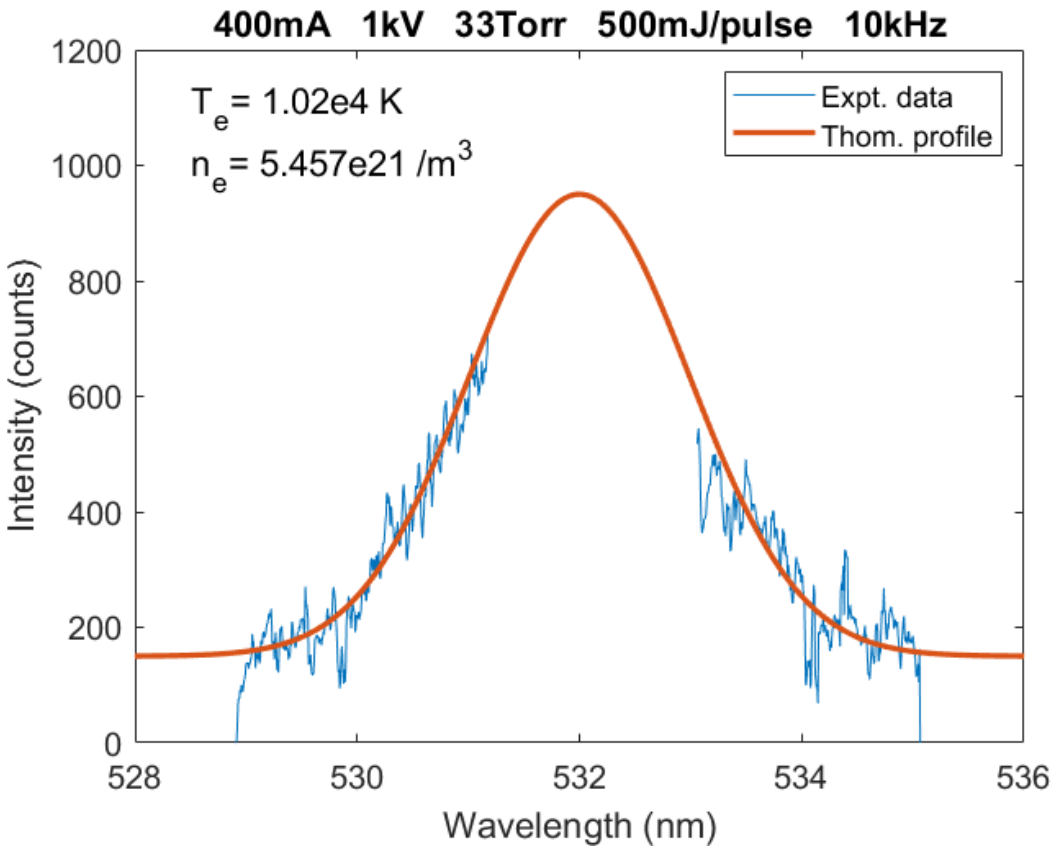


**Figure 22.** Single-shot TS spectrum of electrons in an argon plasma captured by our high-speed TS system at 10 kHz. The plasma was generated using 400 mA, 1 kV DC power at 33 Torr.

**(a)**

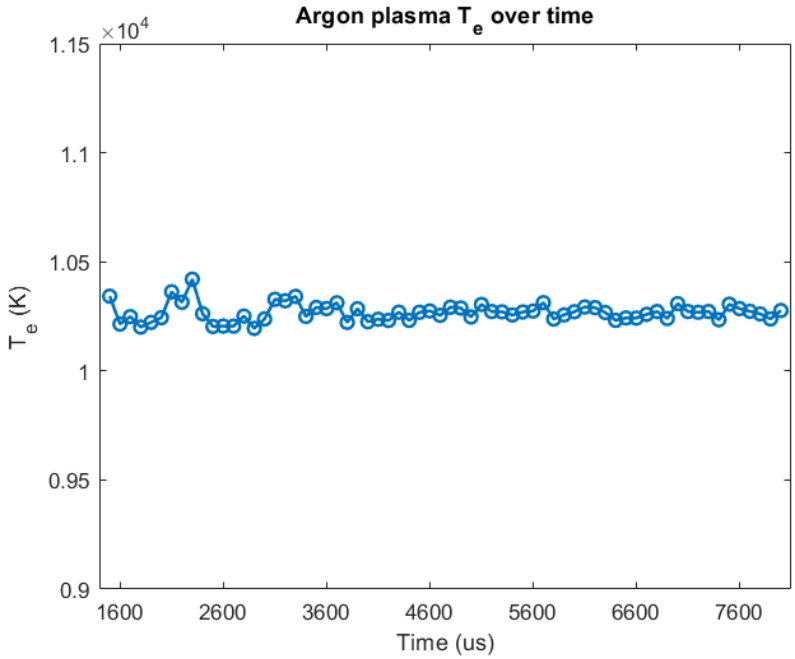


**(b)**

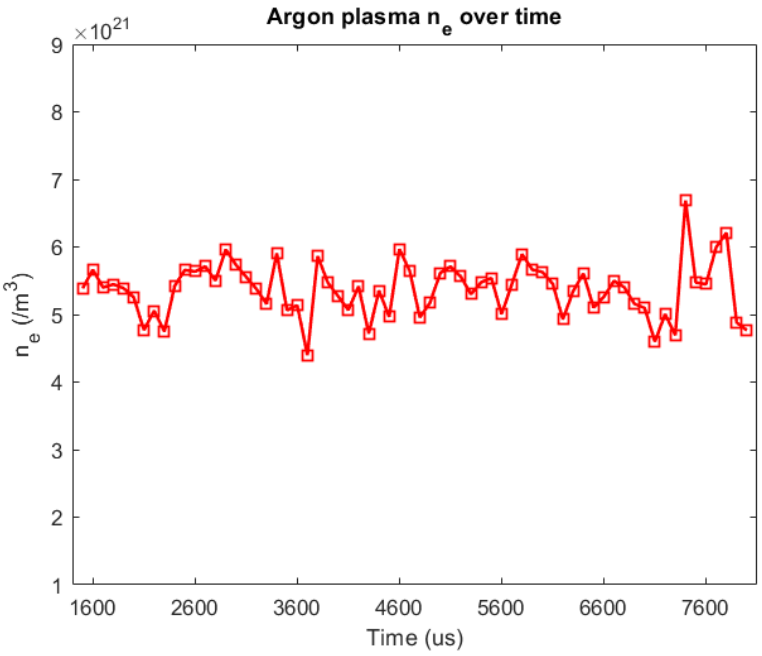


**Figure 23.** Measurements of electron temperature and absolute electron number density of the argon plasma by 10 kHz Thomson scattering. (a) Electron temperature fluctuates around 0.88 eV. (b) Calibrated by 10 kHz rotational Raman scattering, the electron number density fluctuates around $5.37 \times 10^{21}$ $m^{-3}$.

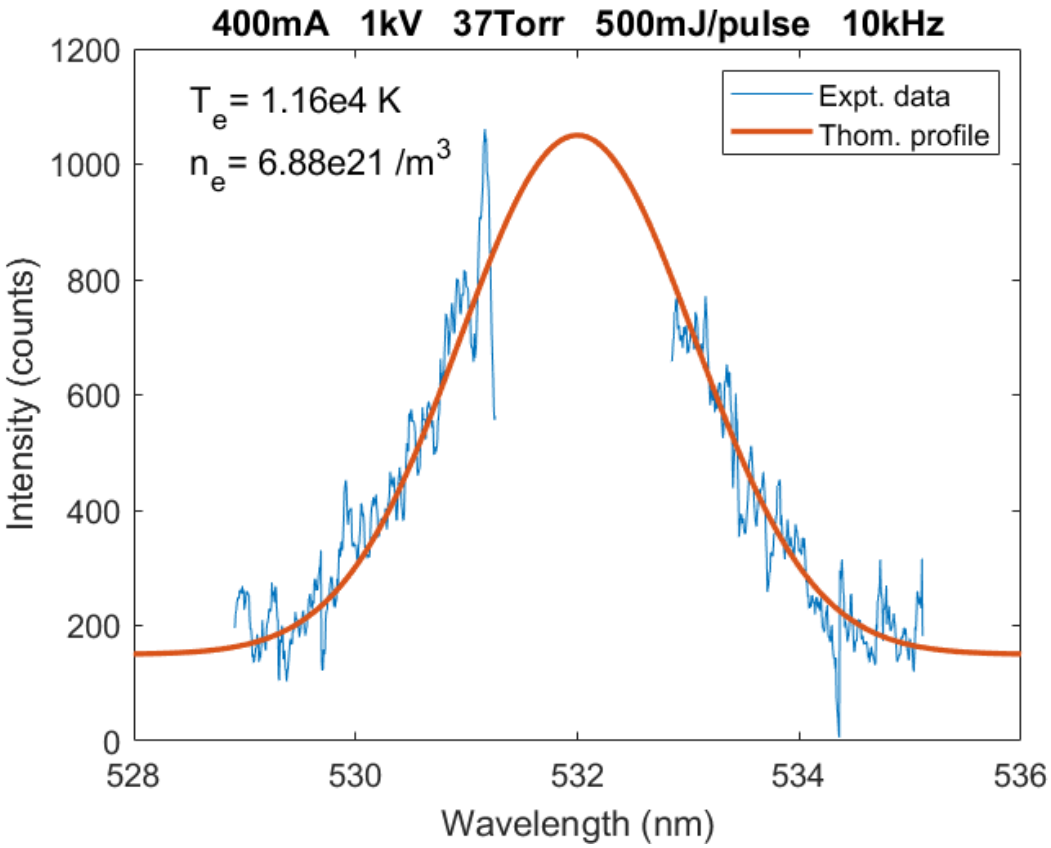


**Figure 24.** Single-shot TS spectrum of helium plasma captured by the high-speed TS system. The Thomson profile of the spectrum has been automatically generated, and the electron temperature and electron number density have been computed.

**(a)**

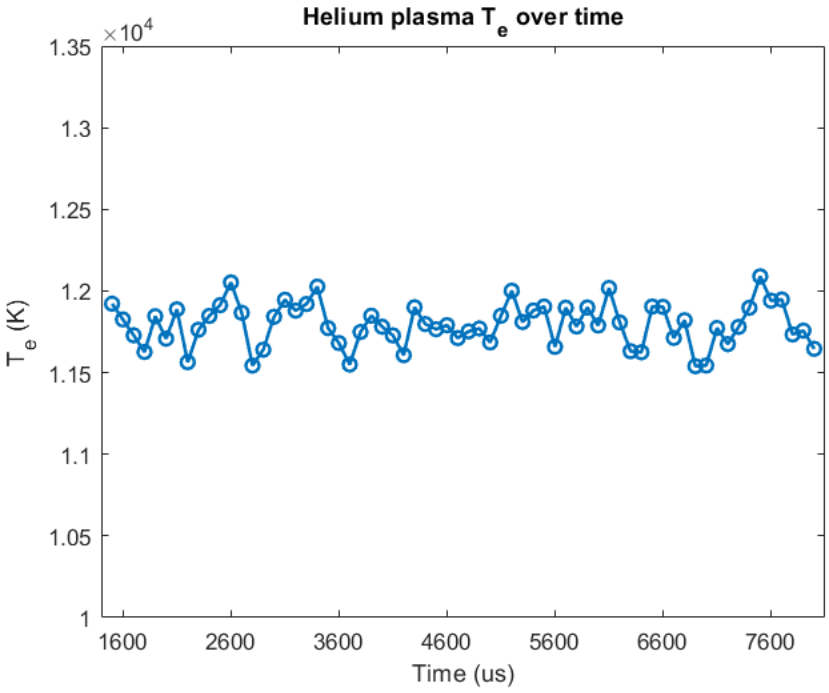


**(b)**

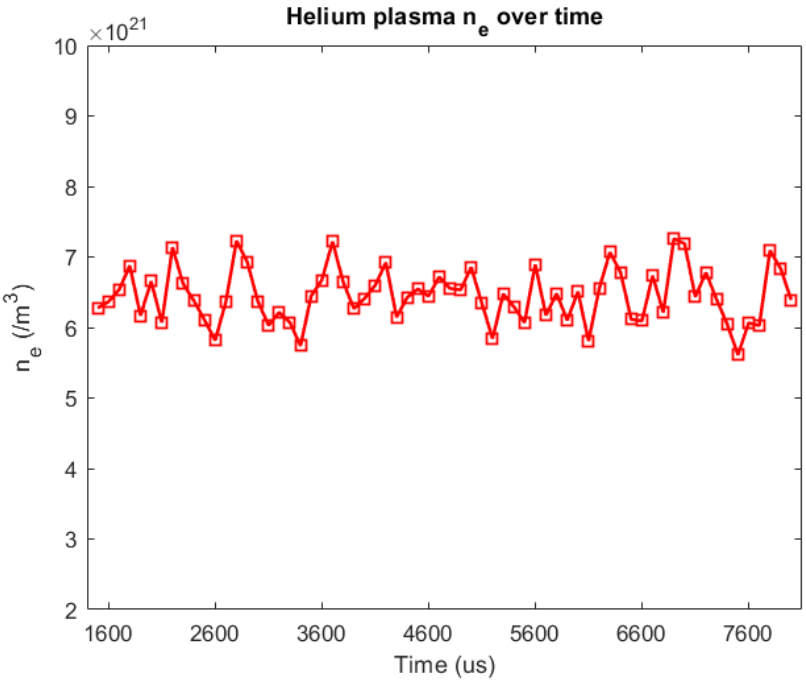


**Figure 25.** Measurements of (a) electron temperature and (b) absolute electron number density for the helium plasma using 10 kHz Thomson scattering.

## Summary

A pulse-burst laser-based high-speed Thomson scattering instrument has been developed and demonstrated for measurements of electron temperature and electron number density of a laboratory plasma. The pulse-burst laser can output 2.3 J/pulse at 1064 nm or 1.3 J/pulse at 532 nm, with a repetition rate of 10 kHz and a burst duration of 10 ms. To avoid optical breakdown in weakly ionized plasmas, the laser pulse was reduced to 500 mJ and was stretched to a duration of ~70 ns to maintain a similar pulse energy but lower the intensity. Rotational Raman scattering of ambient air has been used to calibrate the optical detection system. Single-shot measurements of electron number density and electron temperature in helium and argon plasmas under various conditions have been conducted at 10 kHz. The proof-of-principle demonstration shows significant promise for using the pulse-burst-laser-based TS to track electron temperature and electron density variation in fusion plasma.

## Acknowledgments

This work was supported by the US Department of Energy's STTR program under Grant No. DE-SC0018672 (Program Manager: Dr. Matthew Lanctot).

# CHAPTER FOUR
# SIMULTANEOUS MEASUREMENTS OF FORWARD THOMSON SCATTERING AND ROTATIONAL RAMAN SCATTERING IN A WEAKLY IONIZED PLASMA

A version of the contents in this chapter has been submitted to Optics Continuum and is currently under peer review.

This chapter demonstrates a simultaneous Thomson scattering and rotational Raman scattering spectroscopy in a weakly ionized plasma in air. Thomson scattering was collected in the forward scattering direction, in order to compress the relative spectra width of Thomson scattering from the plasma. Simultaneous measurements of rotational Raman scattering were obtained in the same direction, which was not affected by the collection angles. The measurements thus yielded electron temperature ($T_e$) and electron number density ($n_e$) as well as gas temperature in a weakly ionized atmospheric pressure plasma. The separation of rotational Raman scattering and Thomson scattering occurred when the scattering angle decreased to 20 degrees in the plasma, where the air temperature was found to be 150 ± 25 °C, and electron temperature of the plasma was 0.587 ± 0.087 eV, and electron number density was (1.608 ± 0.416) × $10^{21}$ $m^{-3}$. The technique could be used for various plasma and combustion diagnostics in realistic engineering environments.

## Introduction

It is essential to study the characteristics of atmospheric pressure plasma (APP) due to its increasing applications in industries such as medicine [51], adhesives [52], catalysis [53], and food processing [54]. In a weakly ionized plasma, the vast difference in temperatures between electrons and neutrals results in using APP for heat-sensitive materials like food [55] and skin [56]. The measurements of electron number density and temperature [57] are vital due to its interaction with various species, which enhances the physicochemical properties of plasma and its interactions with the exposed surface. The creation of reactive molecular species [58] is dependent on direct electron impact reactions, such as

dissociation and excitation of the molecules. Electron kinetics play a significant role in these reactions, and it is directly related to electron temperature. Thus, measuring the electron number density and temperatures is salient in studying various plasma parameters for creating new plasma reactors that will have enhanced and reliable performance with longer lifetimes.

Laser Thomson scattering (TS) diagnostics has been demonstrated as a reliable and well-trusted plasma diagnostic technique for electron temperature ($T_e$) and electron number density ($n_e$) measurements [20, 32, 59]. However, in plasmas made of molecular species at moderate pressures (>10 Torr) at low electron temperature ($T_e$ ~ 1-10 eV), the rotational Raman scattering (RR) can be overlapped with the TS spectrum. For instance, in a TS measurement of a weakly ionized plasma, RR emission is also captured in the spectrum [58, 60, 61]. Also, in hypersonic flows [62], where the electron number density is relatively low compared to the neutral number density, RR interferes directly with TS. Conventionally, separating RR spectrum from TS spectrum requires subtracting a fitted RR spectrum [61]. This is only reliable when the temperature of the gas is already known, so a theoretical RR spectrum can be determined and subtracted from the overlapped "RR + TS" spectra. For cases where gas temperature is unknown or hard to determine, such as in a weakly ionized plasma with gas being heated by the plasma, the RR spectrum cannot be determined without making an assumption or estimation of the gas temperature, which makes the Raman-subtraction-based RR-TS separation unreliable, especially in cases where the plasma conditions and gas temperature is time-variant.

An alternative approach, whether the temperature of the gas is known or not, is to separate RR and TS physically, by utilizing forward collection angles [62]. Previously, Filip et al. applied forward Thomson scattering [63] for the detection of relativistic waves in plasma density of $2\times10^{15}$ $cm^{-3}$. Also, Glenzer et al. used forward TS for measuring high-density plasmas using X-ray [64]. Forward TS is obtained by placing the collection optics in a forward direction, i.e., the angle of the Thomson scattering collected by the imaging system is smaller than 90 degrees. As TS is essentially an elastic collision between photons from

the incident laser and the free electrons in the plasma, the frequency of the scattered photons is unchanged. However, from the observer's view, the frequency of the Thomson scattered photons are shifted due to thermal Doppler broadening, which is illustrated by Equation 1, 2 and 3 in Chapter One. As discussed in [65], the Thomson scattering has a Gaussian profile due to Doppler broadening. The full width at half maximum (FWHM) of the Gaussian curve is used to determine the electron temperature ($T_e$) of the plasma, as shown in Chapter One. The uncertainty of measuring $T_e$ and $n_e$ with TS diagnostics is respectively defined by Equation 7 and 8 [15],

$$\delta T_e = \frac{m_e c^2}{2k_B} \times \frac{\delta \Delta\lambda}{\ln(2)\lambda^2} \tag{7}$$

$$\delta n_e = \frac{\delta A_e}{A_{N_2}} \times \frac{d\sigma_{N_2}/d\Omega}{d\sigma_e/d\Omega} \times n_{N_2} \times f \tag{8}$$

where $\delta T_e$ and $\delta n_e$ are respectively the statistical uncertainty of $T_e$ and $n_e$, $\delta\Delta\lambda$ and $\delta A_e$ are respectively the uncertainty of fitted HWHM of TS spectrum and integrated intensity of TS.

As shown in Equation 5, the scattering angle is also a factor in the $T_e$ calculation. Therefore, for a plasma with a constant $T_e$, the measured HWHM of its TS profile becomes smaller as the scattering angle of collected the Thomson scattered photons becomes smaller. On the other side, as the RR emission is associated with energy released from laser-excited polyatomic molecules returning from a higher (virtual) energy level to lower ones, and the energy levels are independent of scattering angle, the wavelengths of RR emission do not change with scattering angles [66]. Therefore, it is possible to separate TS and RR spectrum by narrowing the TS spectrum by detecting TS in a forward direction [62], so that TS stays in the gap between the Stokes and anti-Stokes lines of RR. Figure 26 shows that theoretical forward TS spectrum of a plasma with constant $T_e$ and $n_e$ becomes narrower than the TS spectrum obtained from 90-degree scattering. The benefit of this technique not only

separates TS and RR spectra but also allows simultaneous measurements of electron temperature and electron number density of the plasma via TS and the temperature of the gas via RR.

Here the simultaneous measurements of TS and RR from a weakly ionized atmospheric pressure plasma and plasma-heated air were demonstrated by using forward collection angles. Electron temperature and electron number density of the plasma, as well as the air temperature were determined simultaneously. The parameters measured will be useful in validating or improving the computational simulation of atmospheric pressure plasmas.

## Experimental Design

***Plasma source***

The atmospheric pressure plasma was a pin-to-pin glow discharge of weakly ionzied air (nonthermal plasma, scattering parameter α was 0.4 degrees scattering) with a tip-to-tip electrode distance of 0.5 inch. It was powered by a high-power AC source (CTP-2000K, Nanjing Suman Plasma Technology Co., Ltd.) with an adjustable input voltage set on 260 Volt AC, and an input current at 260 mA. And the output voltage of the source was 30 kVAC with an adjustable output frequency set on 22 kHz, the output current was estimated to be a few mA. The full set of the power source consists of the high-power AC power source and two transformers (120 V to 220 V). The output of power source is controlled by the adjustable voltage transformer.

***Thomson scattering setup***

TS spectra are taken from scattering angles of 20, 30, 50, 70 and 90 degrees while the plasma remains the same. RR spectra of ambient air (not heated by plasma) from each angle are also separately obtained for corresponding $n_e$ calibrations as well as system alignment verification [20]. The TS setup for 90 degrees scattering is illustrated in Figure 27.

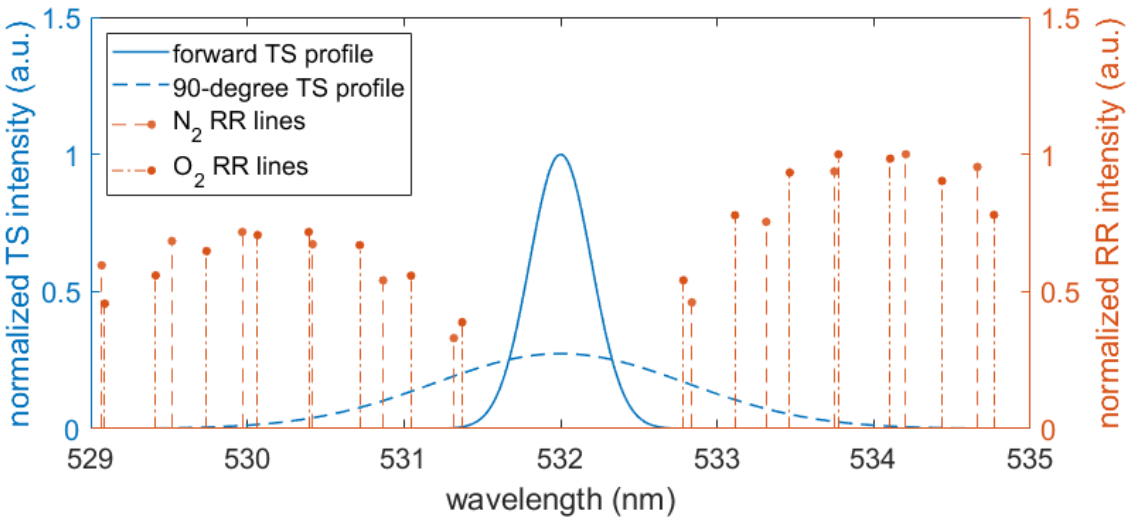


**Figure 26.** Theoretical forward TS spectrum of a plasma with constant Te and ne becomes spectrally narrower than the TS spectrum obtained at 90 degrees, thus "sits" between the gap between the Stokes and anti-Stokes lines of RR spectrum of air. Thus RR and TS are spectrally separated. TS spectra are normalized to the height of the forward TS spectrum, RR lines are normalized to its highest line.

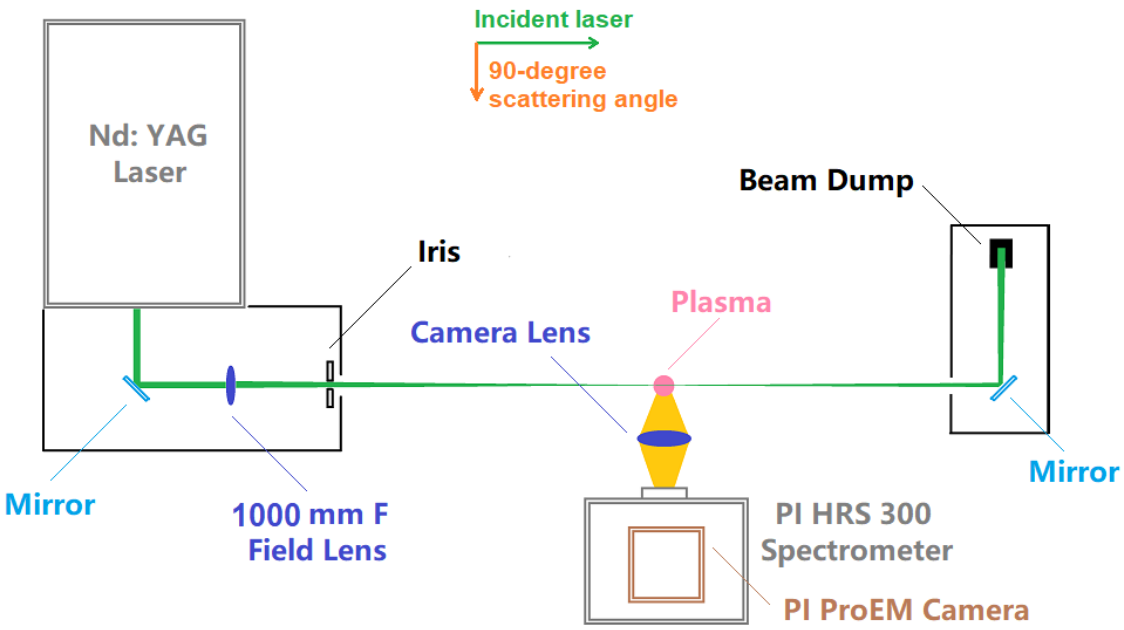


**Figure 27.** Diagram of the 90-degree Thomson scattering setup from a top-down view. For 30 to 70 degrees scattering, the camera lens and the imaging system were moved accordingly to the corresponding forward positions to collect 20-, 30-, 50-, 70-degree Thomson scattering spectra.

The probing laser was a Nd: YAG pulsed laser (Powerlite 8020) running on 10 Hz mode (outputs 120 mJ/pulse at 532 nm, pulse width 7 ns). The laser was first focused by a field lens with a 1000 mm focal length to generate intensity ~$1.1 \times 10^{10}$ W/cm$^2$. The focused laser probed the plasma that was generated between the electrodes. Finally, the laser was collected by a beam dump. The Thomson scattering photons were collected by a camera lens (focal length 50 mm). And the imaging system consisting of a spectrometer (Princeton Instrument SpectraPro HRS-300) and an electron-multiplying CCD camera (Princeton Instrument ProEM HS) was used to obtain the 90-degree TS spectrum. For 30- to 70-degree scattering, the camera lens and the imaging system were moved accordingly to the corresponding forward positions to collect those forward TS spectra. The TS setup for 20 degrees scattering was different from the others, because the angle was too sharp to just move the camera lens and the imaging system. Therefore, an additional concave mirror of 150 mm focal length was placed at the 20-degree position to reflect the forward Thomson scattered photons into the camera lens, as shown in Figure 28.

***Stray light removal***

Since TS is weak compared to incident laser beam, it is crucial to reduce the background and stray light to increase the signal-to-noise ratio of the TS spectrum. Stray light mostly comes from the reflections of the laser optics, and secondary reflections from other surfaces in the proximity. As the plasma was generated in atmospheric air, there was no vacuum chamber to obtain a stray light profile that can be directly subtracted from the TS spectrum in the post-processing. Therefore, a stray light mitigation setup was implemented to physically reduce the stray light intensity to near zero. As shown in Figure 28, multiple laser safety screens were used to form two housings to contain the laser optics inside, so that all the reflections from the optics were boxed in, hence removing stray light. Figure 29 (a) and (b) compare the intensity of stray light “before” and “after” the stray light mitigation. Figure 29 (c) shows an image of the laser beam intercepting the center of the atmospheric pressure plasma after the stray light mitigation was in place.

**(a)**

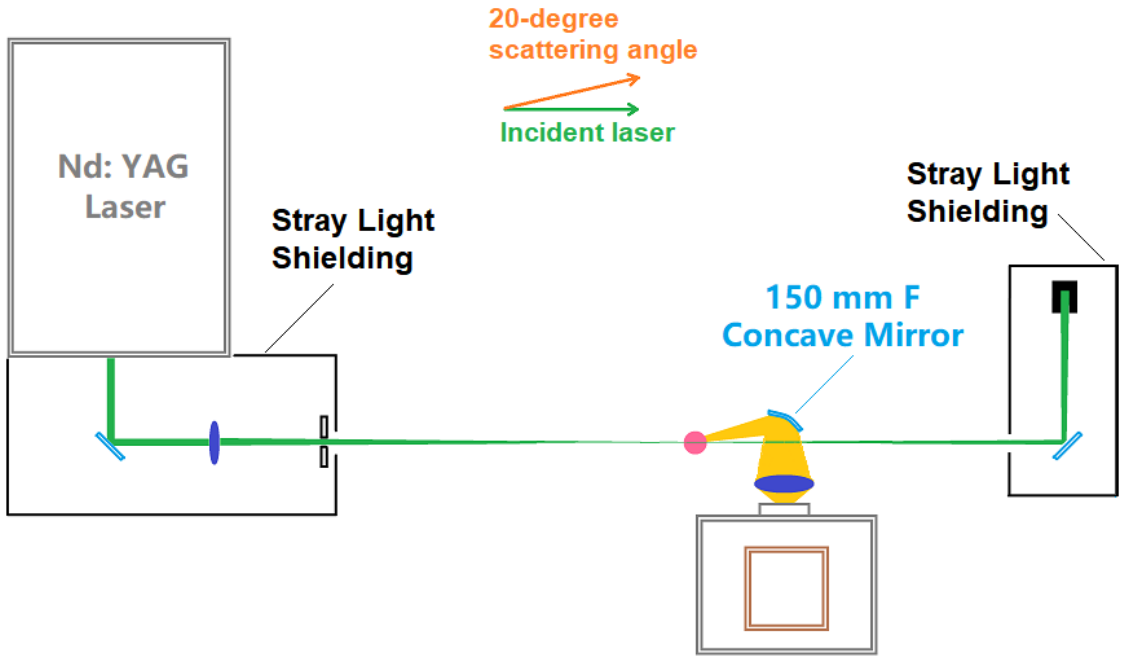


**(b)**

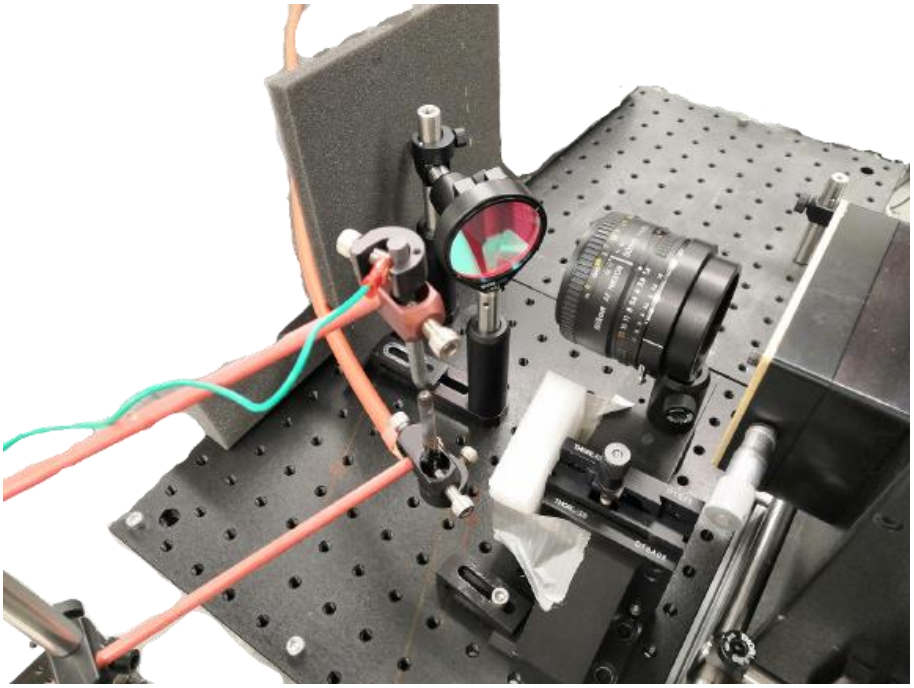

**Figure 28.** (a) Diagram for 20-degree forward Thomson scattering. Due to the sharp angle, an additional concave mirror was placed at the 20-degree position to collect Thomson scattered photons. (b) A photo of the collection optics used in 20-degree scattering.

**(a)**

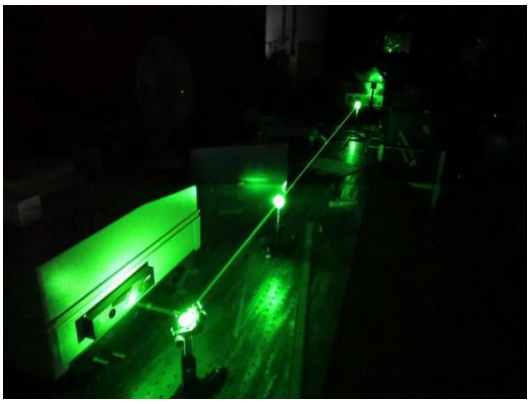

**(b)**

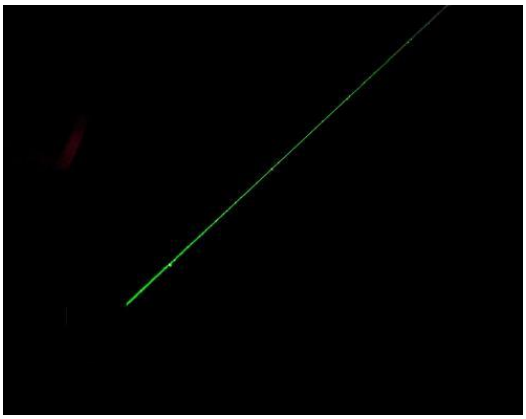

**(c)**

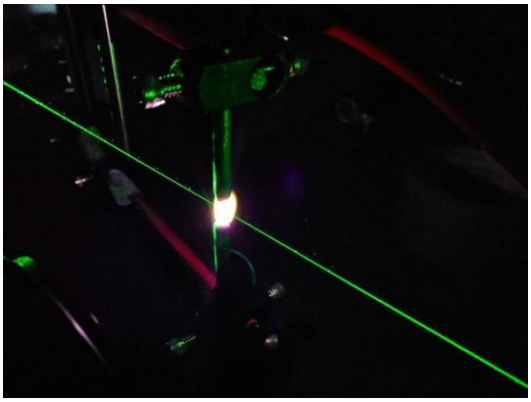

**Figure 29.** Demonstration of stray light mitigation for atmospheric pressure plasma. (a) An image of the laser beam and stray light before the stray light mitigation. (b) An image of the laser beam taken with the same camera settings after the mitigation process. The stray light intensity had been reduced to near zero. (c) An image of the laser beam probing the center of atmospheric pressure plasma after the stray light mitigation was in place.

## Experiment Results

RR spectra of ambient air from various forward scattering angles were first conducted as system alignment checks, and the Stokes line at transition J=4→6 from each scattering angle was used with corresponding forward TS spectrum to calibrate the electron number density of $n_e$ in the plasma. Figure 30 shows the RR spectrum obtained at 90 degrees (averaged over 300 shots) as an example, the red and blue dashed lines indicate the wavelengths and intensities of theoretical RR lines of $N_2$ and $O_2$, respectively, which is a good match with the experimental data. Subsequently, TS spectra at scattering angles of 90, 70, 50, 30 and 20 degrees were obtained while the plasma maintained the same (same electrode distance and same output power from the plasma source).

Figure 31 shows TS spectra obtained from the plasma at 90- and 20-degree scattering angles as the best examples: TS spectrum being entangled with RR spectrum at 90 degrees and TS spectrum being separated from RR spectrum in the forward 20-degree direction. From 90 to 20 degrees, each spectrum was an average of 300 shots. For spectra from 90 to 30 degrees, the $T_e$ was hot enough for the TS spectrum to expand into the RR spectral region. Therefore, for spectra from 90 to 30 degrees, TS and RR were separated by subtracting a theoretical RR spectrum based on the assumption that the air temperature was at room temperature (22 °C). But as the scattering angle decreased, the FWHM of the TS profile was reduced. When the scattering angle came down to 20 degrees, the TS spectrum became narrow enough to "sit" within the gap between the RR Stokes lines and anti-Stokes lines, thus achieving RR-TS separation in the forward scattering direction. It should be noted that the TS spectral profile was obtained by fitting a Gaussian curve based on the "wings" of the TS spectrum, as the central part (532 nm) is dominated by Rayleigh scattering in Figure 32.

It is now possible to determine the air temperature from the RR spectrum by finding the best fit via adjusting the temperature parameter of a theoretical RR spectrum to the RR portion of the data, since the RR spectrum does not interfere with the TS spectrum in the 20-degree forward scattering.

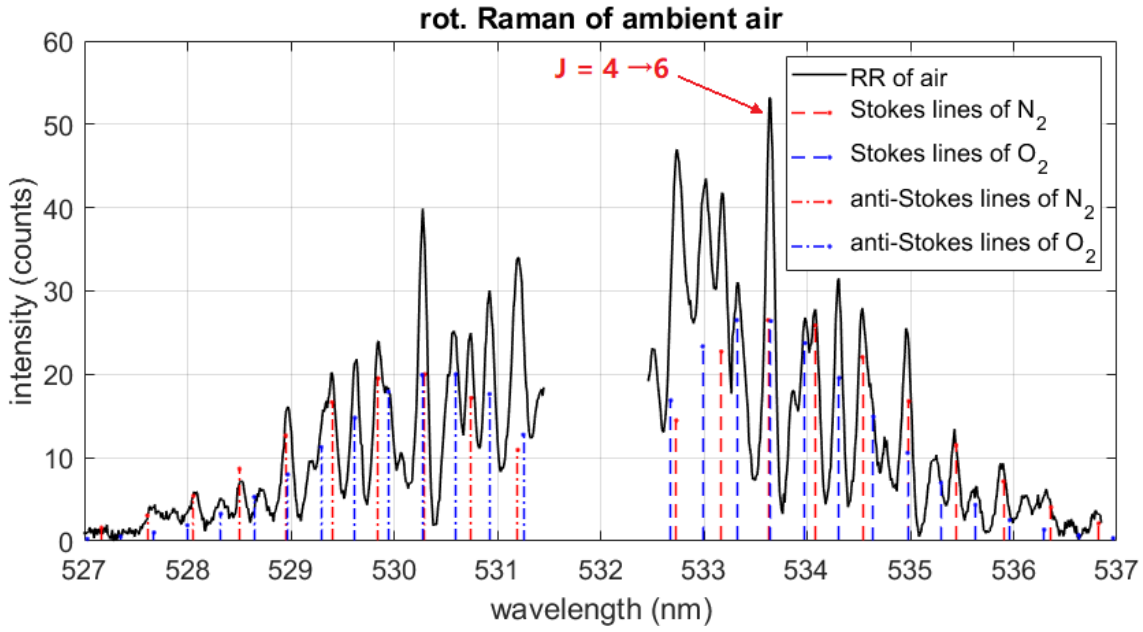


**Figure 30.** Rotational Raman spectrum of ambient air obtained at 90-degree scattering angle. The red and blue dashed lines indicate the wavelengths and intensities of theoretically rotational Raman lines of $N_2$ and $O_2$, respectively.

**(a)**

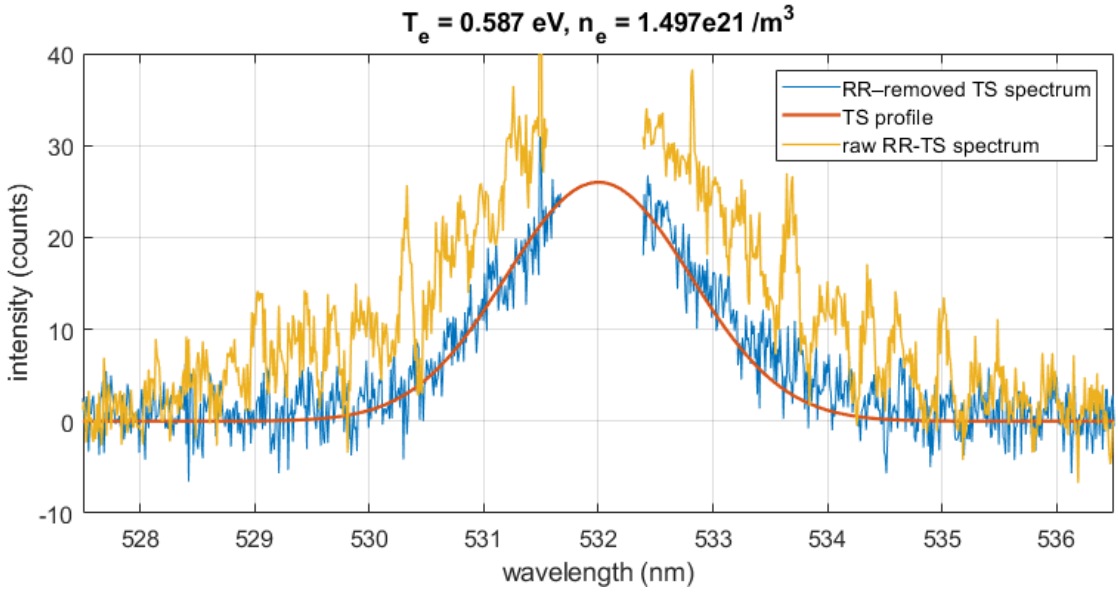


**(b)**

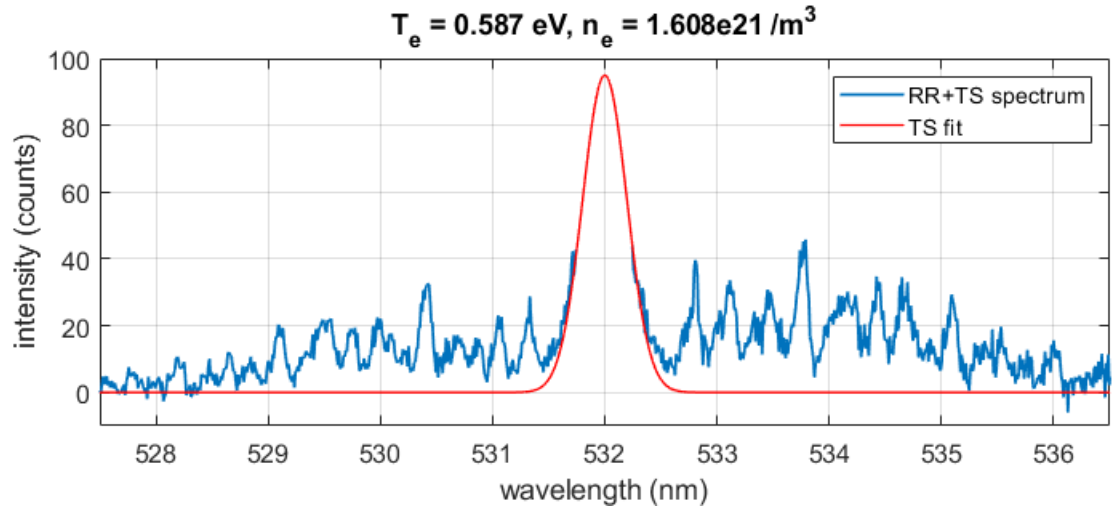


**Figure 31.** (a) From 90 degrees scattering angle, the "wings" of Thomson scattering expanded into the lines of rotational Raman of air, becoming a baseline offset for RR. (b) At 20 degrees, TS spectrum becomes narrow enough to be separated from rotational Raman scattering.

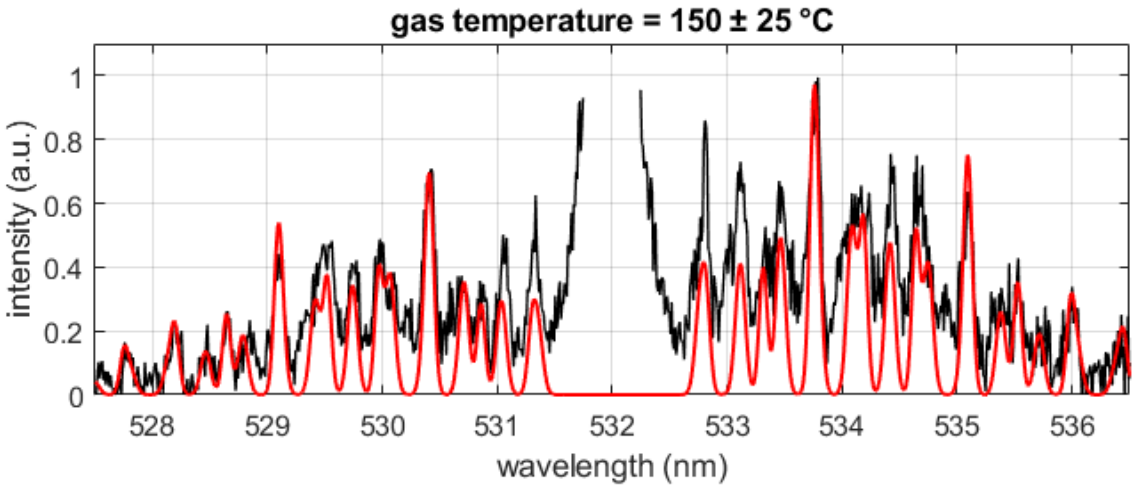


**Figure 32.** A simulated RR spectrum is fitted to the normalized RR portion of the 20-degree forward RR-TS scattering data. The spectrum was normalized to its strongest RR line. The fitting of the RR lines suggests the air temperature was 150 ± 25 °C.

As shown in Figure 32, a simulated RR spectrum is fitted to the RR section of the 20-degree forward "RR + TS" scattering data. The broadening in the simulated Raman lines is based on the instrument broadening (slit width of the spectrometer), which is the major source of the broadening effect for RR. The fitting of the RR lines suggests the air temperature in the plasma was 150 ± 25 °C.

Figure 33 (a) displays the fitted TS profiles obtained from the same atmospheric pressure plasma from all the scattering angles and theoretical RR lines at 150 °C. For this particular plasma, the bottom part of the TS from 20-degree scattering was wide enough to fit in the "gap" between the Stokes and anti-Stokes lines of RR.

Figure 33 (b) and (c) respectively show $T_e$ and $n_e$ of the plasma calculated from all the TS spectra. From 90 to 30 degrees, TS profile was obtained by subtracting a theoretical RR spectrum from the RR+TS spectra, while the gas temperature was assumed to be room temperature, only at 20 degrees scattering angle, the RR-TS separation occurred, and gas temperature was directly obtained from finding the best RR fit to the RR spectrum.

From 20 to 90 degrees, the $T_e$ are respectively 0.587 ± 0.087, 0.575 ± 0.062, 0.585 ± 0.035, 0.581 ± 0.039, and 0.587 ± 0.063 eV; and the $n_e$ are respectively (1.608 ± 0.416) × $10^{21}$, (1.531 ± 0.325) × $10^{21}$, (1.566 ± 0.371) × $10^{21}$, (1.582 ± 0.369) × $10^{21}$, and (1.497 ± 0.393) × $10^{21}$ $m^{-3}$. Both $T_e$ and $n_e$ are fairly consistent throughout the measurements at all the scattering angles. The errors of the measured electron temperatures and densities are propagated through the statistical uncertainty of the instruments and fitting errors.

**(a)**

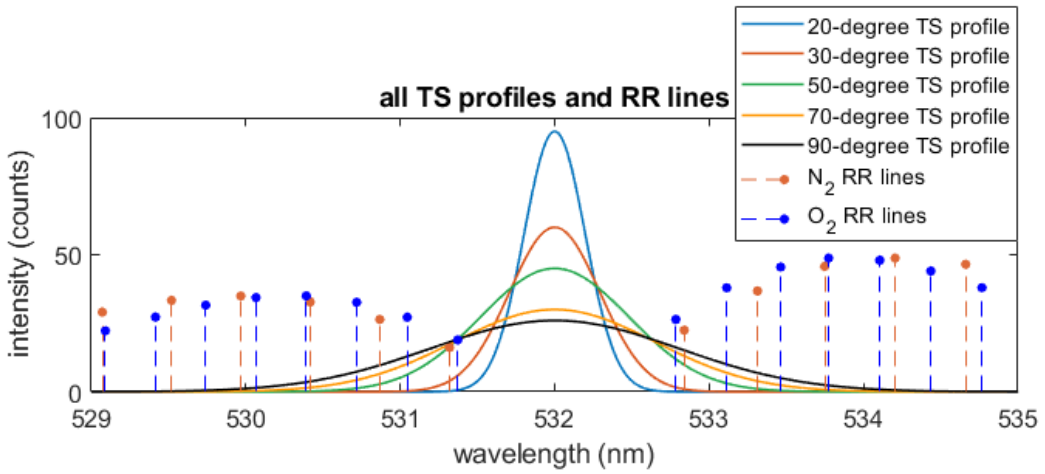


**(b)**

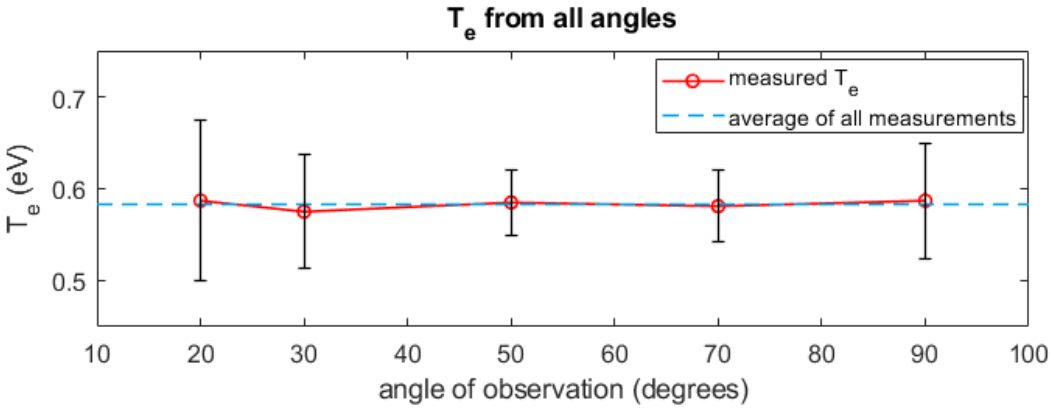


**(c)**

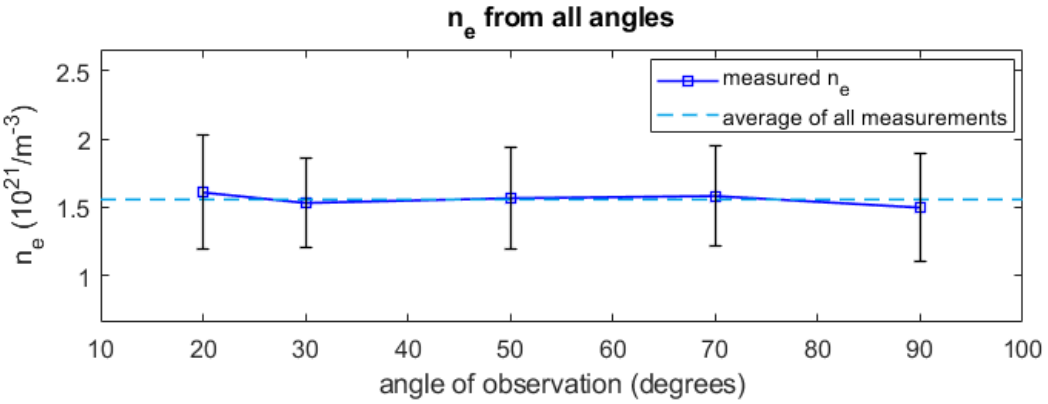


**Figure 33.** (a) TS profiles fitted from TS spectra with scattering angle 20, 30, 50, 70 and 90 degrees, as well as theoretical rotational Raman lines of air. (b) $T_e$ calculated from the Thomson scattering spectra. (c) $n_e$ calculated from the Thomson scattering spectra.

## Discussions

The immediate and the most important benefit of forward TS is the spectral separation of RR and TS. According to Figure 33, $T_e$ and $n_e$ obtained from the conventional RR-subtraction technique is about the same as forward TS technique within the range of error bars. However, forward TS eliminates the necessity of making an assumption of the gas temperature, and instead, it allows direct measurement of gas temperature from the RR+TS spectrum. Additionally, imaging from a forward position is able to increase the SNR. Because for the same plasma, while its FWHM decreases with the scattering angle, its $n_e$ maintains the same. As $n_e$ is proportional to the total emission power of TS, the amplitude of the narrowed TS profile increases to maintain the area (total emission power) of the TS Gaussian profile, thus increasing TS signal strength, and SNR.

The disadvantage of forward TS technique is that the Rayleigh scattering (RS) and stray light contamination overlap on the TS spectrum more than conventional 90-degree TS scattering. As the TS spectrum narrows, more of the TS spectrum "merges" into the RS band (due to broadening, which is a very narrow band centered on incident laser wavelength) and the "wings" of TS becomes smaller and harder to identify. And this could potentially increase the fitting error, but the benefit of better SNR from forward scattering also helps with the curve fitting and reduces the fitting error.

Another disadvantage of forward TS is possible negative impact on the accuracy of TS measurement. According to Equation 2, the electron temperature of $T_e$ is proportional to $\Delta\lambda^2/\sin^2(\theta/2)$, where $\Delta\lambda$ is the FWHM of the TS profile and $\theta$ is the scattering angle. As the scattering angle $\theta$ approaches 0 degree, the slightest change of FWHM of TS profile would result in a large change of $T_e$ fitting. The increase of fitting error for TS profile not only comes from the difficulty of fitting the smaller TS "wings", but also the increased $T_e$'s sensitivity to scattering angles (~2% fitting error for 90-degree scattering, and ~10% for 20-degree scattering due to $T_e$'s sensitivity to scattering angle). Another notable point for scattering angle is that the Salpeter scattering parameter $\alpha$ also changes with scattering angle. In this experiment, the plasma maintained the same, but $\alpha$ increased from 0.4 to 1.69

due to change of scattering angle (from 90 degrees to 20 degrees). So, an incoherent TS could shift into coherent domain if observed from a small scattering angle, and the spectral shape of TS spectrum as well as the calculation of $T_e$ could change, especially for high intensity lasers. So, a "soft limit" for scattering angle is that the angle must not be too small that TS becomes coherent, nor the uncertainty of fitting becomes too large that the fitted result becomes unconvincing (e.g. the fitting error goes up to ~100% for incoherent TS at 2-degree scattering).

Overall, forward TS has a benefit of higher SNR in the TS spectrum which reduces fitting error, but it also suffers from the difficulty of fitting due to smaller TS "wings" and increased $T_e$'s sensitivity to scattering angle, which both increase the fitting error. Whereas 90-degree TS does not have a SNR boost, it does not suffer from increased uncertainty of fitting either, as $T_e$ is less "sensitive" to scattering angle, and the spectrum is less affected by RS (though it overlaps with RR instead). This could be the reason that the error bars of $T_e$ are bigger at 20 and 90 degrees in Fig 7 (b), but smaller in the middle. The relative large error bar at 20 degrees is mostly the contribution of $T_e$ becoming sensitive to scattering angle, and at 90 degrees it's mostly contributed by the noise (relatively lower SNR) in the spectrum, whereas TS at 50 degrees is a balance between SNR and $T_e$ 's sensitivity to scattering angle, and resulted in the smallest error bar.

On the other hand, there is not a hard limit for maximum FWHM in forward TS technique either. As mentioned above, RS and stray light contaminates TS spectrum, and as TS gets narrower, the smaller the "wings" TS will be left to identify the TS profile and the harder it is to fit it, so the wider the TS spectrum, the easier it is to identify its profile. But, to accommodate spectral separation, the TS spectrum can only be as wide as the "gap" between the Stokes and anti-Stokes lines of RR, which puts a limit to FWHM as well. Since the "gap" varies with the composition of the gas, the maximum allowed FWHM, instead of being a constant, changes with the RR spectrum.

## Conclusions

Thomson scattering is an important optical diagnostics tool to measure electron number density and electron temperature in plasmas. A forward scattering-based RR-TS separation technique has been demonstrated to separate a RR and TS spectrum simultaneously obtained from a weakly ionized atmospheric plasma while the gas was heated to a certain temperature by the plasma. This technique allows simultaneous measurements of gas temperature, electron number density, and electron temperature of the weakly ionized plasma without the necessity of assuming the gas temperature. "RR + TS" spectra were obtained at 90, 70, 50, 30, and 20 degrees, and for this particular plasma, the complete RR-TS separation occurred as the scattering angle decreased to 20 degrees. Based on the 20-degree forward scattering, the air temperature was found to be 150 ± 25 °C, via fitting the RR spectrum; and electron temperature of the plasma calculated from the 20-degree Thomson scattering spectrum was 0.587 ± 0.087 eV, and electron number density was $(1.608 \pm 0.416) \times 10^{21}$ $m^{-3}$.

Forward TS increases the SNR and lowers the detection limit of $n_e$, while it might suffer from some fitting error. And the RR-TS separation is limited by the gas type, as the "gap" between the RR Stokes and anti-Stokes lines varies with RR spectrum of different gases. In the future, this methodology can be applied to atmospheric plasmas, plasma biomedicine, plasma catalysis, surface adhesion, and food processing. The measured data will help simulate plasma for understanding the reaction mechanism resulting in the evolution of species of interests.

## Acknowledgment

We would like to recognize the suggestions from Dr. Theodore Biewer in the error analysis. The work was supported by DOE, NSF, and GeoSonics.

# CHAPTER FIVE
# COMPRESSED SINGLE-SHOT HYPERSPECTRAL IMAGING

A version of the contents in this chapter was presented at the American Institute of Aeronautics and Astronautics (AIAA) SciTech Conference in 2020, and published on Applied Optics. Although the contents in this chapter is not directly related to Thomson scattering diagnostic, it serves as a preliminary study for future implementation on 2D Thomson scattering diagnostic.

This chapter demonstrates a compressed sensing-based single-shot hyperspectral imaging system for combustion diagnostics. The hyperspectral system can capture well-resolved spectra in a 2D plane through a single shot, i.e. converting a 3D data cube of 2D spatial and 1D spectral information into a compressed 2D hyperspectral image. Experimentally, the light emissions are first coded by a random binary pattern to generate the hyperspectral content, which is then sent through a spectrometer. The resulting compressed hyperspectral image is computationally analyzed to recover original 2D spatial and 1D spectral information. $C_2$* and CH* chemiluminescence emissions of a methane/air flame at various equivalence ratios are measured using the compressed hyperspectral imaging technique. Comparison to traditional measurements shows good agreement in the correlation of emission ratio to equivalence ratio. The technique can be further applied to other laser-based combustion diagnostics.

## Introduction

Combustion remains an essential part of modern technology, with no viable alternative having yet been emerged for practical aerospace vehicles. Novel combustion technologies, such as those for hypersonic vehicle propulsion systems and rotating detonation engines (RDEs), require detailed measurements of combustion processes for proper engineering and optimized operations. Since combustion processes are susceptible to disruption by physical probes, spectroscopic techniques are widely used for studying various aspects of

combustion. Characteristics, such as equivalence ratio [67, 68], velocity [69], temperature [70], and chemical concentration [71-73] in flames, can be determined non-intrusively from spectroscopic measurements. For many of the quantitative spectroscopic techniques, spectrometers are used, with the spectral resolution of the detected signal generally limited by the resolution of the spectrometer's gratings. Note that specialized hyper-spectrometers produce improved resolution [74], but require multiple spatial scans to obtain the full signal for larger regions of interest.

Compressed Sensing (CS), also known as compressive sensing or sparse sampling, is a type of digital signal reconstruction technique that recovers information from an under-sampled signal by finding the optimized solutions to the corresponding under-determined linear system of the signal [75, 76]. The prerequisite for CS is that the sampled data points must be incoherent and sparse in a domain. Since the technique is based on the signal's sparsity, it is not constrained by the maximum signal frequency and is therefore able to bypass the restriction imposed by the Nyquist sampling theorem on classical fixed-rate signal processing [76]. Typical images are sparse in nature so that CS has resulted in significant improvement in image compressions.

In the field of spectroscopy, compressed sensing has made it possible to obtain a 2D-spectral image with a 1D signal in a similar fashion to 1D-to-2D digital image reconstruction, or a hyperspectrum using a spectrometer or other similar light-dispersing device (e.g. a prism) instead of using a conventional hyperspectral imaging device [77, 78]. Even 1D-to-3D compressed hyperspectral reconstruction has been shown to be possible [79]. Though it results in lower resolution compared to conventional spectroscopy, the most significant benefit of compressed hyper-spectroscopy is that the hyperspectrum can be acquired in a single exposure instead of scanning the spectral region of interest with sequential exposures like a conventional hyper-spectrometer. This capability easily engenders acquisition of the full hyperspectra of transient targets, such as flames. Some spectra and/or images from combustion diagnostics are sparse in nature, such as chemiluminescence[80], Laser-induced Breakdown Spectroscopy(LIBS) [68], Radar

REMPI (coherent microwave scattering from Resonance-enhanced Multiphoton Ionization) [81], CARS (Coherent Anti-stokes Raman Scattering) [82], and Laser-induced Fluorescence (LIF) [83]. CS technique is demonstrated for chemiluminescence as an example to illustrate single shot 2D spatial and 1D spectral measurements in the flames.

## Principles

### *Description*

Compressed hyperspectral imaging is based on compressed sensing [76]. It involves acquisition of the emitted or reflected light coming from the scene or object and encoding it with a predesigned spatial binary pattern that has some level of sparsity (randomness). The encoding is performed by passing the light through or onto a physical implement such as a grating. In this work, the encoder is a digital micro-mirror device (DMD). The encoded light is collected by a light-dispersing device (e.g. a spectrometer). Then, the light-dispersing device generates spectral information by dispersing the coded light in one spatial direction according to its wavelengths, creating a spectral image. Thus, the spectral image contains two spatial axes (X and Y) in which the spectral axis ($\lambda$) is the same as one of the spatial axes. Once the spectral image is obtained, a reconstruction algorithm is utilized to separate the spectral axis and the spatial axis, and also to estimate the information lost by the coding process and thus recover a 3D hyperspectral data cube that contains both the spatial pattern of light emitted from the scene (or reflected from the object) as well as spectral information corresponding to emission wavelengths. The overall procedure requires both the coded spectral image and the coding pattern, as illustrated in Figure 34.

### *Algorithm*

The reconstruction algorithm used for the experiments is Compressed Hyperspectral Augmented Image Reconstruction (CHAIR), which is based on Two-step Iterative Shrinkage/Thresholding (TwIST) [84].

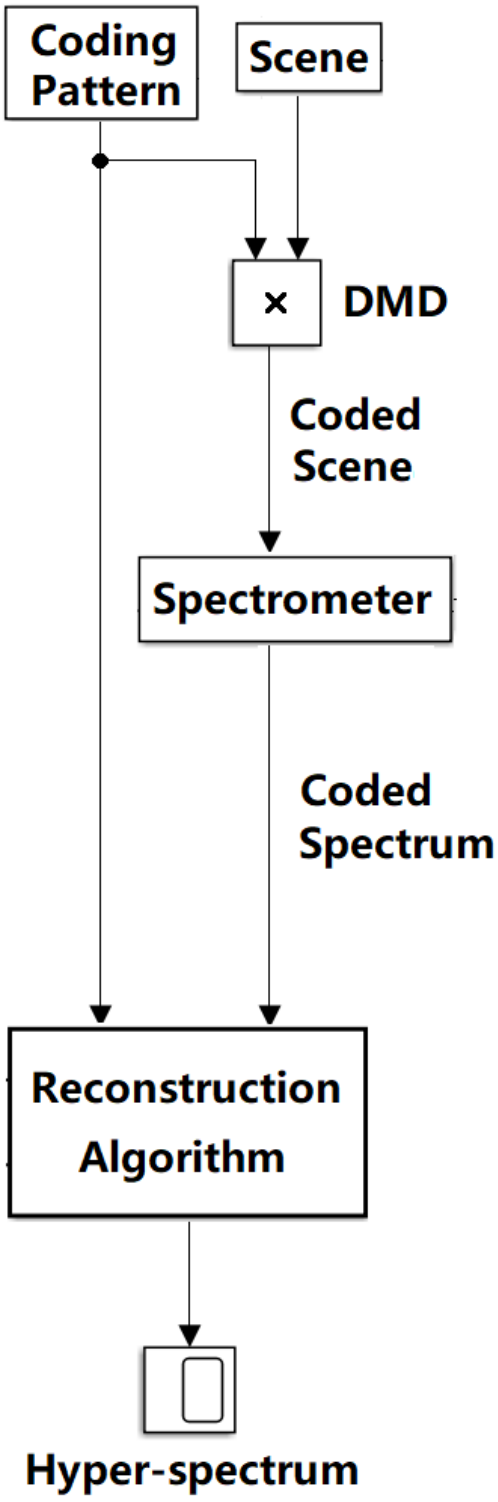


**Figure 34.** Block diagram illustrating the "hardware portion" of the compressed hyperspectral imaging technique.

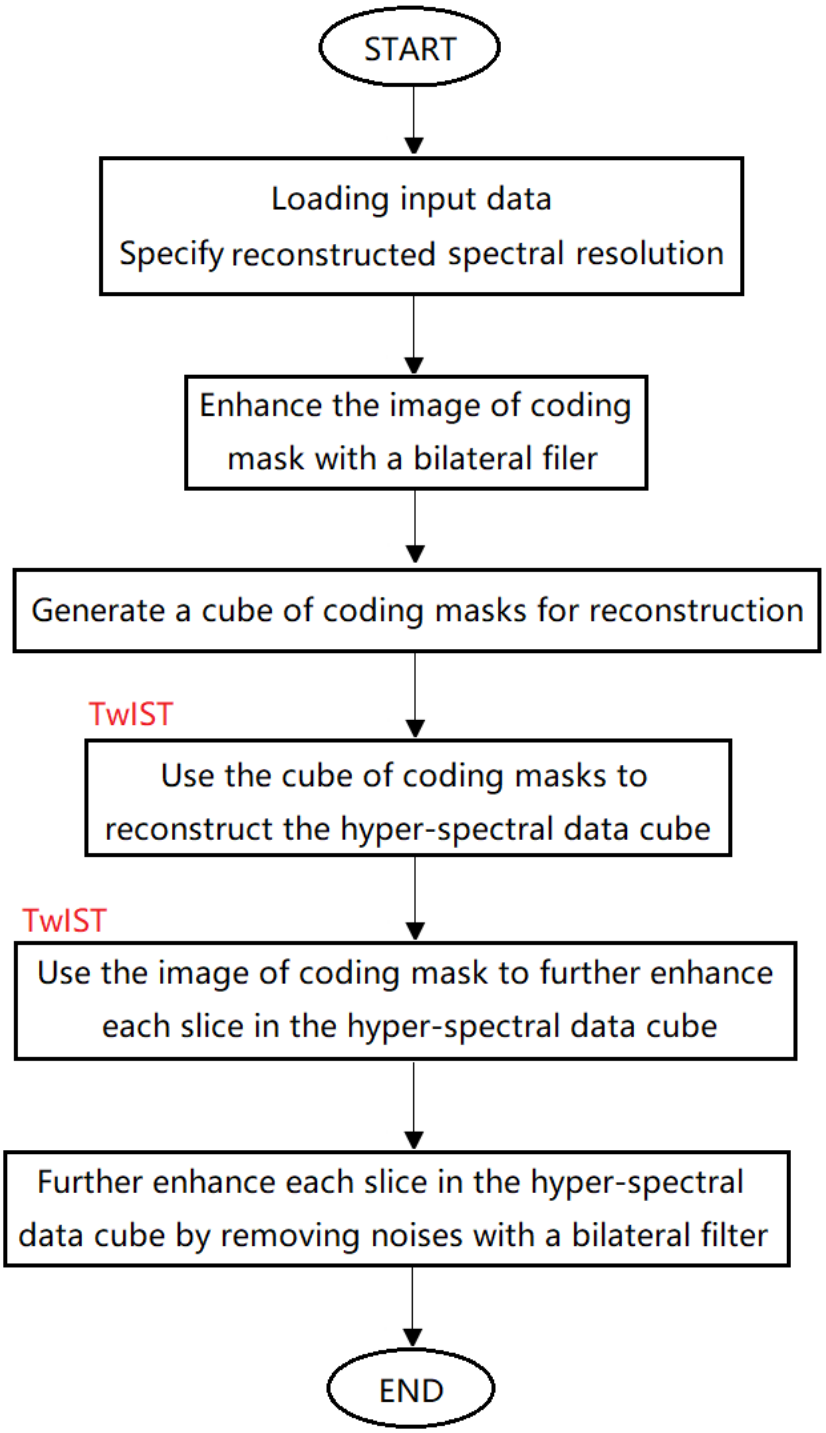


**Figure 35.** Algorithm flow chart illustrating Compressed Hyperspectral Augmented Image Reconstruction (CHAIR). It was designed specifically for hyperspectral reconstruction.

The CHAIR procedure is illustrated in Figure 35. CHAIR improves reconstruction quality by first enhancing the image of the coding pattern using a bilateral filter with a Gaussian kernel. A bilateral filter is a type of non-linear, edge-preserving, and noise-removing filter for smoothing images. The filter smooths the low frequency components in the image, while minimizing its effect on high frequencies that cause blurring. Next, a 3D cube of images of the coding mask is generated, in which each cube slice corresponds to a specific wavelength and is incrementally shifted away from the other slices along the wavelength axis. The 2D coded spectrum and 3D cube of shifted coding patterns are uploaded to the TwIST algorithm and the reconstructed hyperspectrum is generated. Residuals of the coding pattern may be left in the reconstructed hyperspectrum, and can be removed by running TwIST for a second time with the 2D coding pattern image and the 3D reconstructed hyperspectral cube. TwIST uses the image of the coding pattern to scan the hyperspectral slices and removes any residuals of the coding pattern. White noise is removed from the reconstructed hyperspectral slices by a bilateral filter.

Figure 36 shows the capability of TwIST to restore an image coded by a random binary pattern (RBP) that preserves half of the information from the original image. The MATLAB built-in image Cameraman is computationally masked by a high sparsity RBP with the same resolution as the image to simulate the encoded signal detected in compressed sensing. The image recovered by TwIST exhibits some loss of detail but maintains high similarity to the original.

Non-uniform intensity distribution of the encoded signal can be corrected by TwIST. Figure 37 shows the results of a simulated non-uniform signal intensity. A shaded RBP with a darker right hand side is used as the coding mask, therefore introducing non-uniform intensity to the input image. The subsequent reconstruction shows that the original intensity profile has been restored.

**(a)**

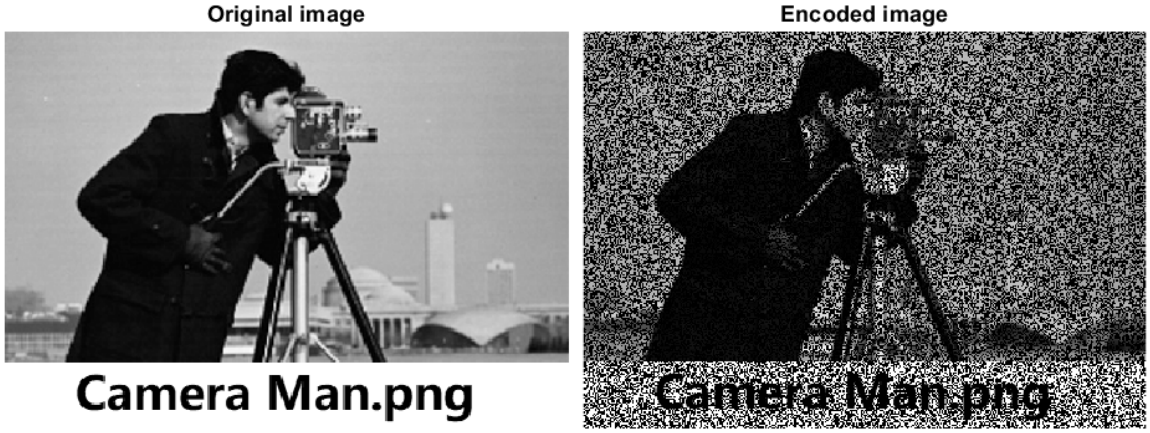


**(b)**

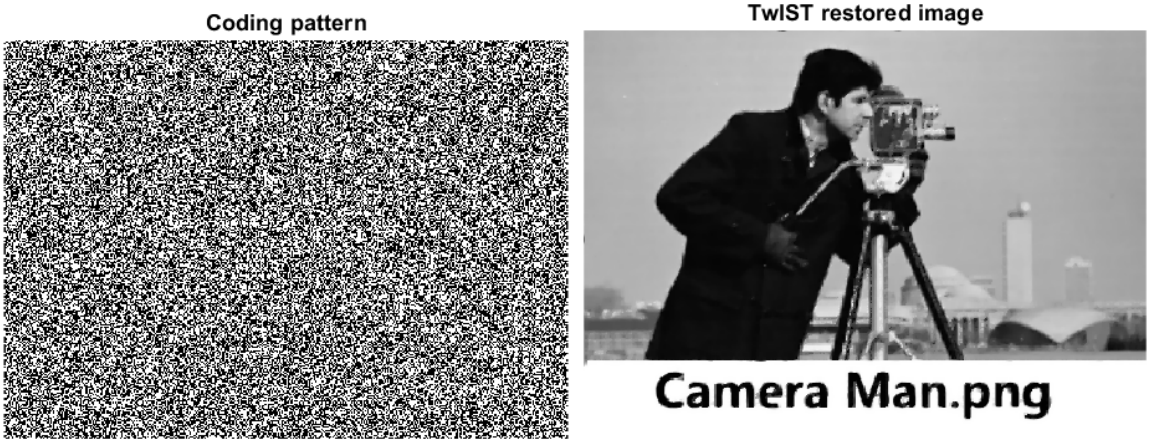


**Figure 36.** Compressed image reconstruction via TwIST. (a) From left to right: ground truth image; RBP coded image. (b) From left to right: the RBP applied on the ground truth image; the image reconstructed with TwIST. Details of the text "Camera Man.png" is degraded after reconstruction, suggesting loss of high frequency information.

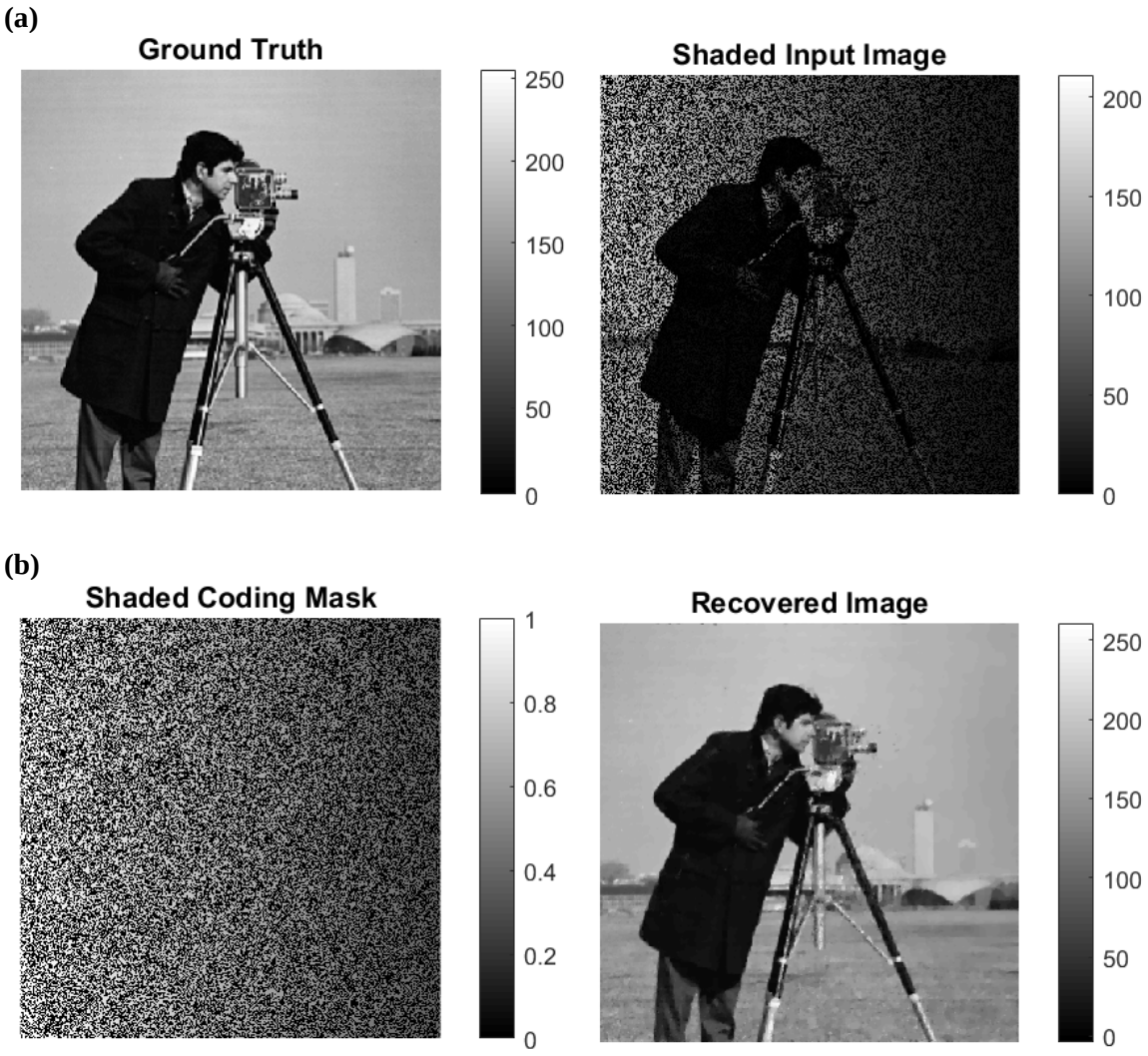


**Figure 37.** Non-uniform intensity correction via TwIST. (a) From left to right: ground truth image; input image with non-uniform intensity. (b) From left to right: shaded RBP coding mask simulating the effect of non-uniform intensity distribution on the DMD; reconstructed image.

## Experimental Setup

The demonstration of single-shot hyperspectral compressed sensing consisted of three parts. The first part was proof-of-concept testing of the reconstruction algorithm, Compressed Hyper-spectral Augmented Image Reconstruction (CHAIR), by computational simulation. Next, the concept was tested experimentally by reconstructing a two-color hyperspectrum of a target card. Finally, the technique was applied to generating hyperspectra of methane/air flames at various equivalence ratios.

The imaging setup is shown in Figure 38. It consists of collection optics, a pair of camera lenses, a Texas Instruments Light Crafter 4500 DMD, and a Princeton Instrument PI 2300i spectrometer with a PI-MAX4 ICCD camera. Light from the target object or scene is captured by the collection optics and passed through the first camera lens onto the DMD. The DMD contains 1120 × 912 micro-mirrors; each individual micro-mirror is mounted on a micro-electromechanical system (MEMS) that can independently rotate the micro-mirrors 12 degrees to the left or right of the orthogonal direction. A random binary pattern (RBP) is uploaded to the DMD, allowing it to encode the light reflected from the target scene by rotating the micro-mirrors fully into or away from the axial direction of the spectrometer slit based on the RBP's intensity values. The coded signal reflected from the DMD is passed to the spectrometer and camera. In order to preserve spatial information of the spectrum, the slit of the spectrometer was fully opened.

The experimental test of the technique was carried out on a USAF resolution card, simultaneously illuminated by low power continuous wave green (532 nm) and red (632.8 nm) lasers. The green laser produced lower intensity on the target than the red laser due to diffusion from the optics used in the laser setup. The reflection from the scene was therefore two-color (532 nm plus 632.8 nm) light with the spatial image of the resolution card. The chemiluminescence application was performed by imaging the non-premixed methane-air flat flame emissions of CH* (430 nm) and $C_2$* (515 nm) from a Hencken burner.

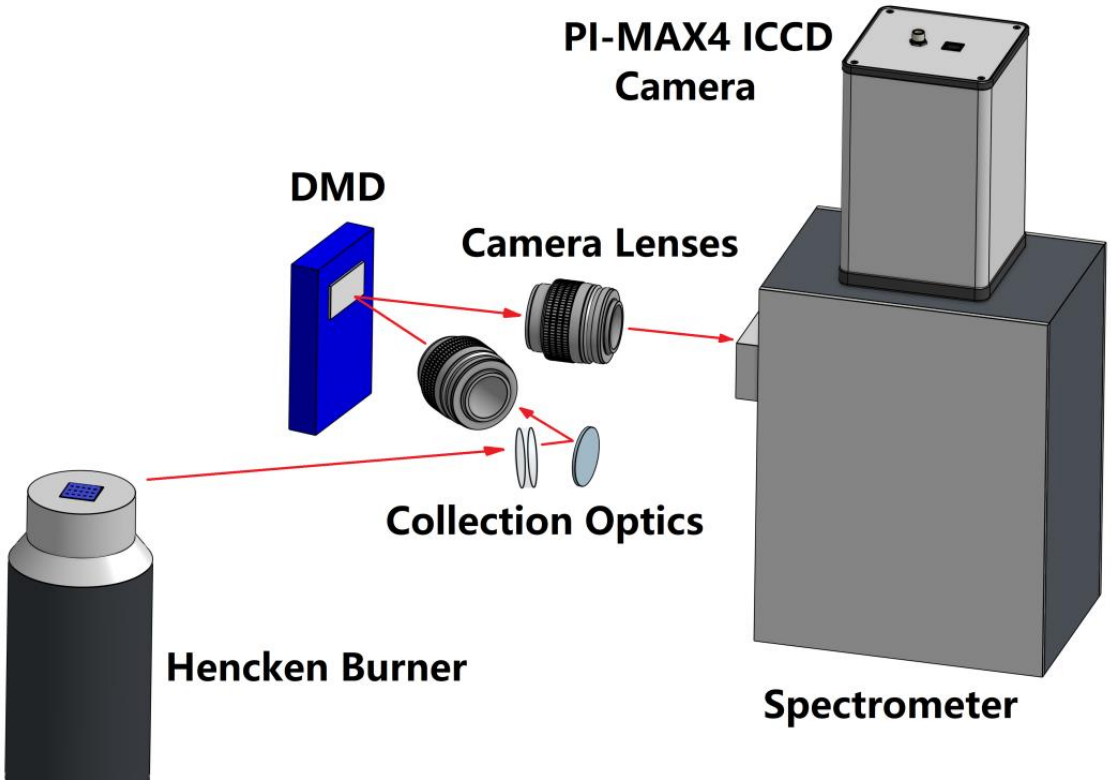


**Figure 38.** Diagram of compressed hyperspectral imaging experimental setup. A methane-air flame was employed for investigating the proof-of-principle of compressed hyperspectral Thomson scattering measurement.

The Hencken burner [85, 86] with a 25.4 mm by 25.4 mm square exit geometry (Technologies for Research, Model: RT1x1) generates a laminar and near adiabatic methane/air flame with sufficient optical access that is lifted from the burner surface since the fuel and oxidizer streams are separated until the exit of the burner. This burner has been widely used as a test bed for laser and optical diagnostic techniques. The fuel tubes have an inner diameter (ID) of approximately 0.54 mm and an outer diameter (OD) of approximately 0.83 mm. The oxidizer honeycomb is a hexagonal pattern with cell size of approximately 0.90 mm. The combustion occurred in open atmospheric conditions, with a fixed air flow rate at 9 L/min and a variable methane flow rate from 1.05 to 1.65 L/min such that equivalence ratios from 0.8 to 1.25 were achieved. According to the adiabatic flame calculation, a flame temperature ranging from 1992 K to 2092 K was obtained depending on the equivalence ratio (0.8 to 1.25) of the inbound gas.

## Results

### *Simulation*

An artificial spectrum was generated with the University of Tennessee's Power T Logo image to test the CHAIR algorithm, using the RGB color channels of the original image. As shown in Figure 39, contained both the spatial information of the image in the X and Y axes as well as spectral information in the third (i.e. $\lambda$) axis in the reconstructed results. The reconstruction showed the variable intensity of each color layer; with the highest intensity in the red channel and the lowest intensity in the blue channel as expected from the orange ground truth image. Therefore, the simulation demonstrated the viability of the CHAIR algorithm for hyperspectral reconstruction of a coded input image. The full results from this simulation are displayed in Figure 40. The coded artificial spectrum was created by moving each color layer of the 300 × 280 image away from its adjacent layer by 20 pixels. A series of simulations was performed to optimize the pixel increment of the layer shifts. The results showed that if the relative pixel increment is too low, the spectrum is essentially continuous, and CHAIR is unable to isolate the overlapped coded images. In most practical cases, spectral bands are not continuous but are very close to each other. In such cases, CHAIR would require a grating with a strong dispersal.

**(a)**

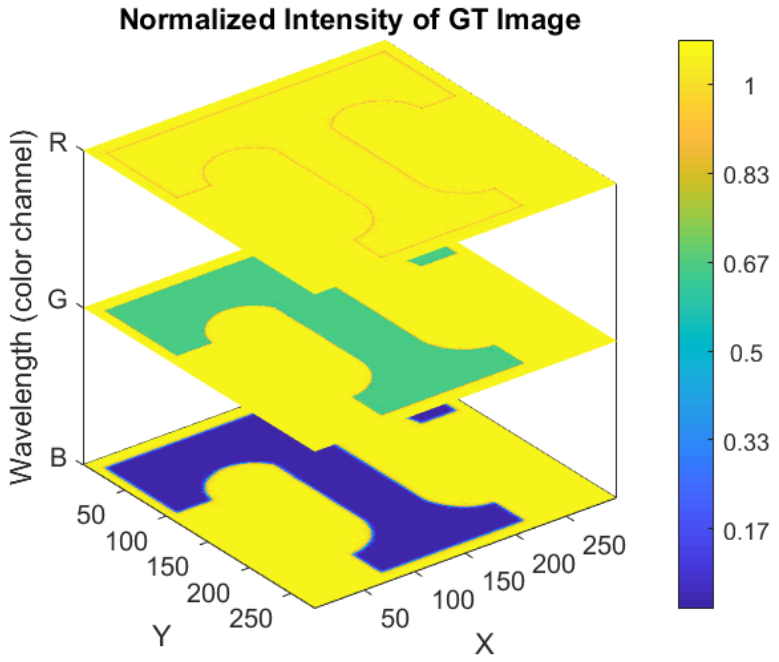


**(b)**

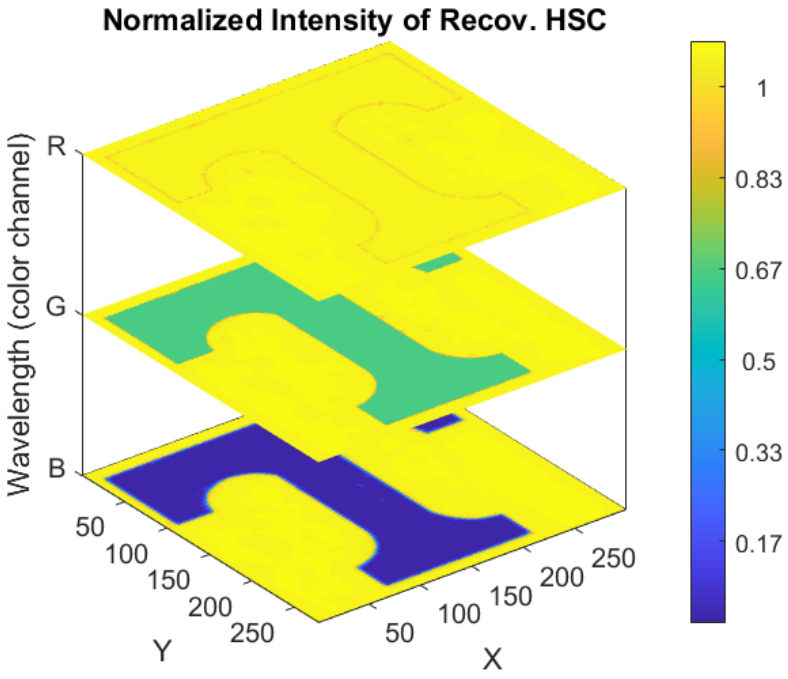


**Figure 39.** (a) Intensity at each RGB layers of the Ground truth "Power T" colored image v.s. (b) intensity at each RGB layers of the same colored image reconstructed from the artificial spectrum of "Power T" by CHAIR.

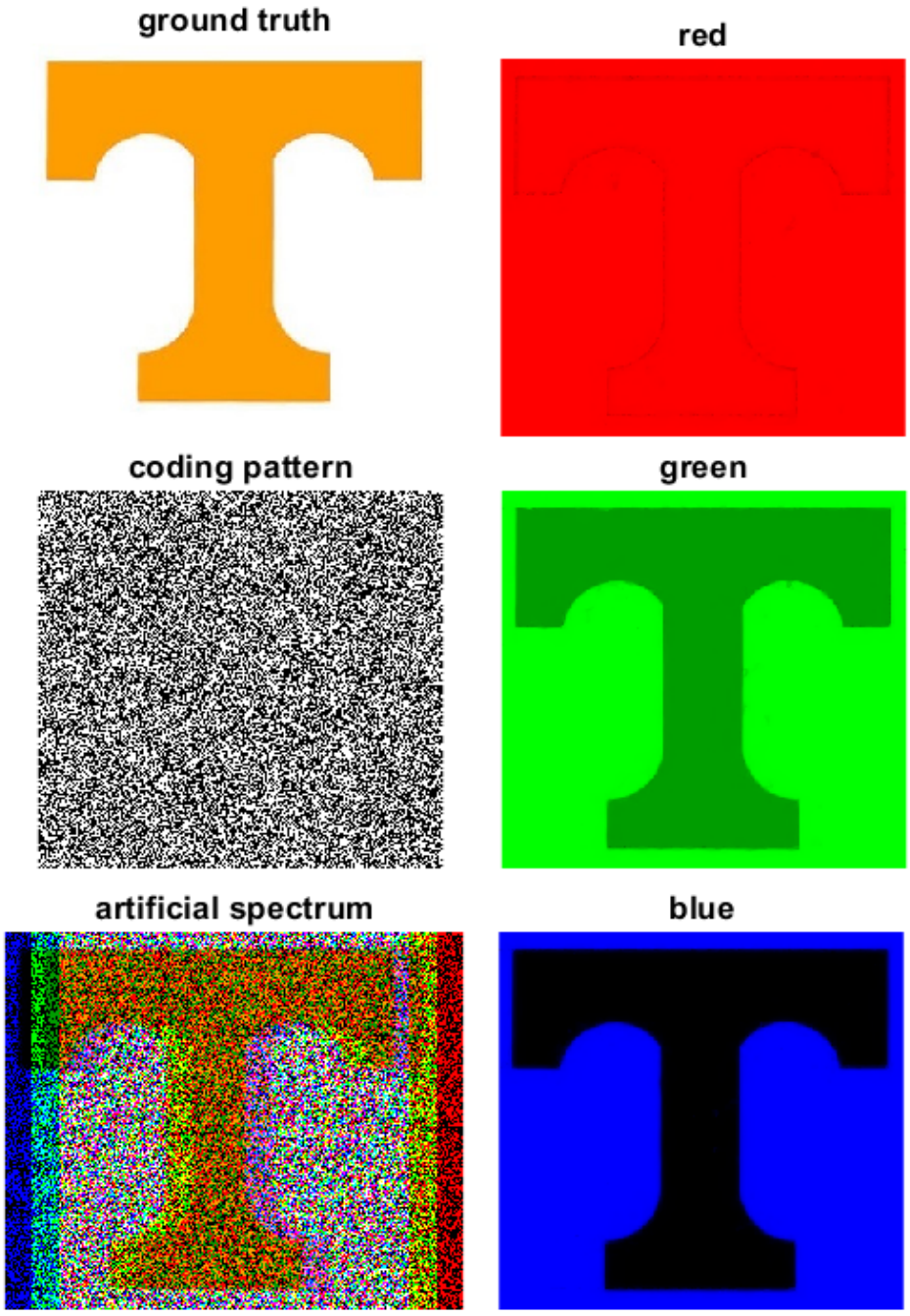


**Figure 40.** RGB image reconstruction by CHAIR compared to ground truth image. Left column from top to bottom: ground truth image; RBP; artificially generated spectrum using the red, green, blue layers of the RBP coded colored image of "Power T". Right column from top to bottom: reconstructed red layer of the colored image; reconstructed green layer of the colored image; reconstructed blue layer of the colored image.

***Dual-Laser Illuminated Resolution Card***

Following the simulations, the hyperspectrum of the two-color illuminated USAF resolution was obtained as a physical validation of the technique. The coding pattern was spatially matched with the coded spectrum in the image by directly imaging a plain target card illuminated by white light so that only the DMD coding pattern was passed into the spectrometer. Additionally, a non-uniform intensity distribution was observed; the non-uniform intensity was corrected using the method described in Algorithm Section. The reconstructed hyperspectrum of the laser-illuminated resolution card is shown in Figure 41. A stronger signal at 632.8 nm and a weaker signal at 532 nm observed in the reconstructed hyperspectrum (this inconsistency was expected due to the difference in the illumination laser intensities as described in Section 3). Results showed that the reconstructed regions-of-interest of the target were blurred by the compressed sensing process indicating the limitation of this setup. However, lower resolution in the reconstructed image is a characteristic of compressed sensing due to the way information is reconstructed from the sampled Fourier domain. Image resolution could potentially be improved by using a DMD with a higher resolution array or finely etched grating to achieve higher spatial detail.

***Flame Chemiluminescence***

Hyperspectra of a methane/air flame at various equivalence ratios were obtained. Figure 42 compares ground truth images, reconstructed spatial images from hyperspectra, and reference photographs taken by a digital single lens reflex camera (Nikon D5100) with filters for detecting 430 nm and 515 nm CH* and $C_2$* emissions, respectively. The images have been artificially color-mapped for visual distinction. Hyperspectral spatial images were generated for a range of wavelengths from which a 3D dataset was formed, as shown in Figure 43. The highest spatial image quality occurred when the equivalence ratio was 1.25. The spectral slices at 430 nm and 515 nm can be isolated from the rest of the hyperspectral dataset to obtain the 2D $C_2$*/CH* ratio as seen in Figure 44.

**(a)**

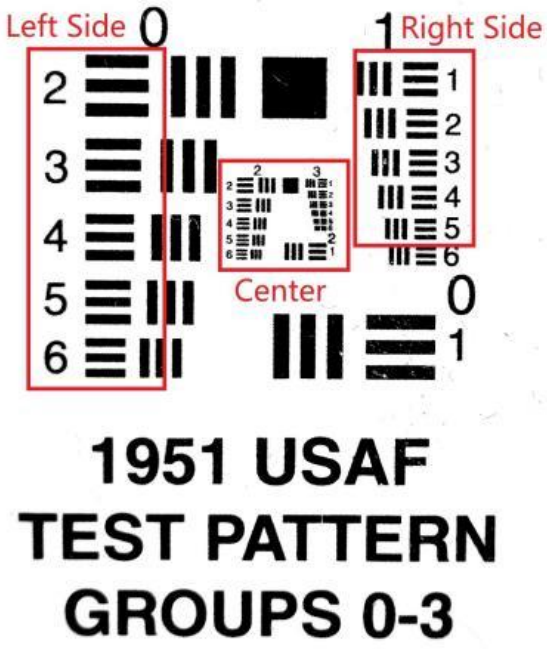


**(b)**

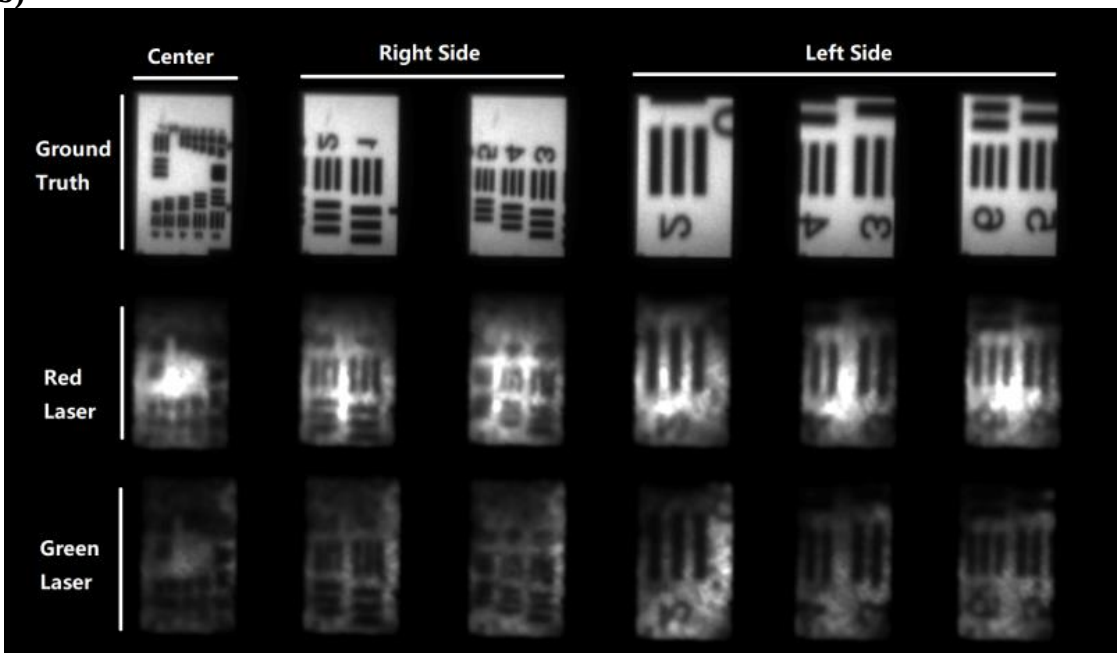


**Figure 41.** Reconstruction results of the laser illuminated USAF resolution pattern. (a) The original USAF resolution test pattern, the imaged areas are highlighted with red squares. (b) The reconstructed results show that the high resolution patterns are blurred by the compressed sensing process.

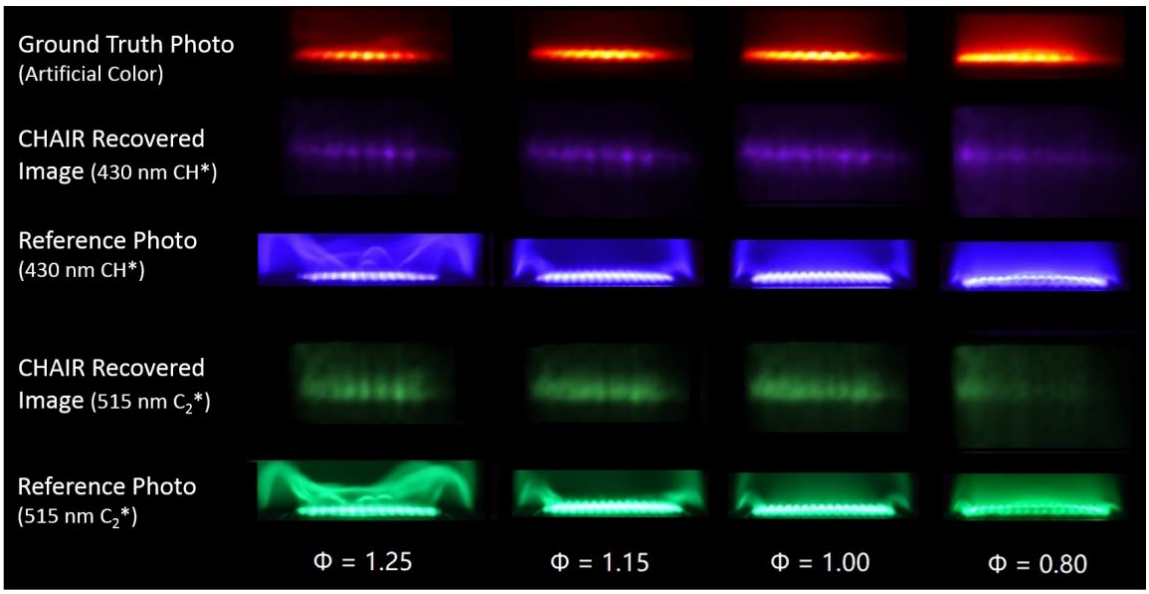


**Figure 42.** Comparison between ground truth spectral images, images from reconstructed hyperspectra, and reference photos taken with corresponding filters.

**(a)**

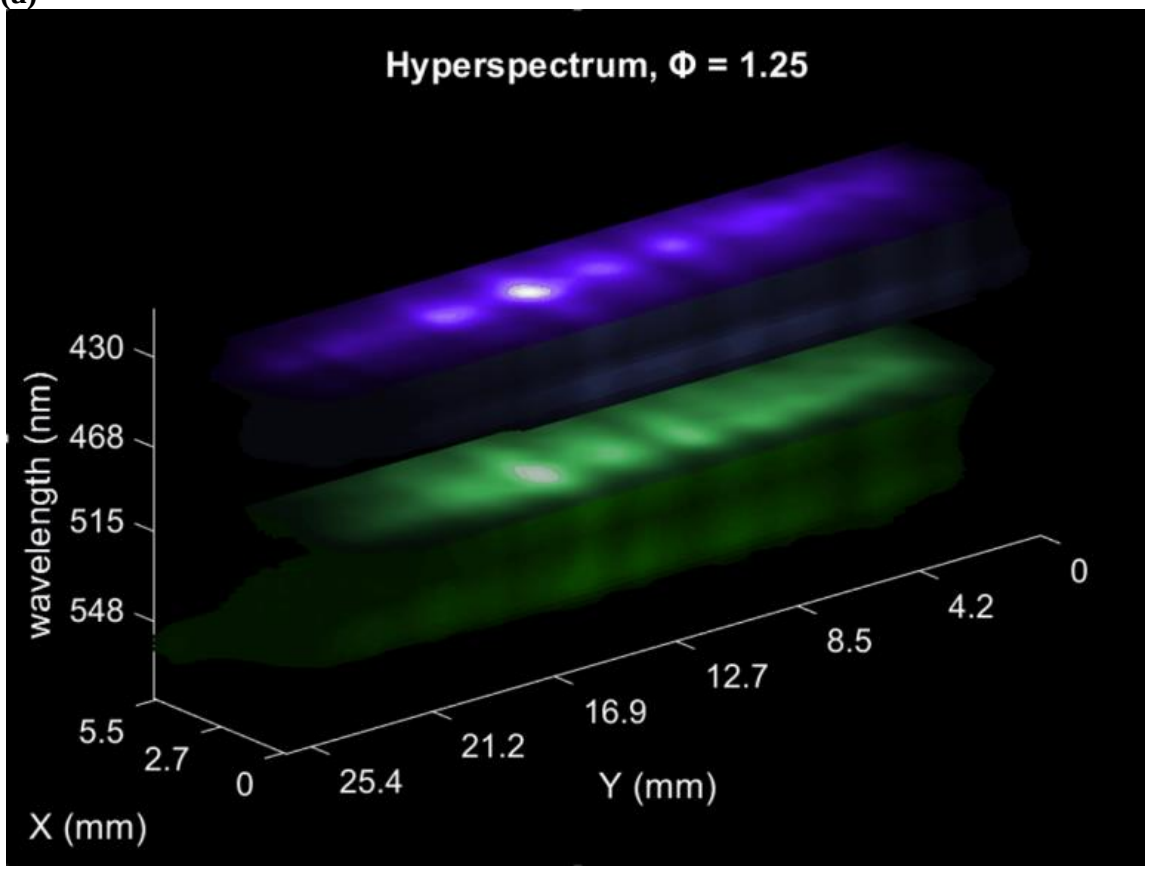


**(b)**

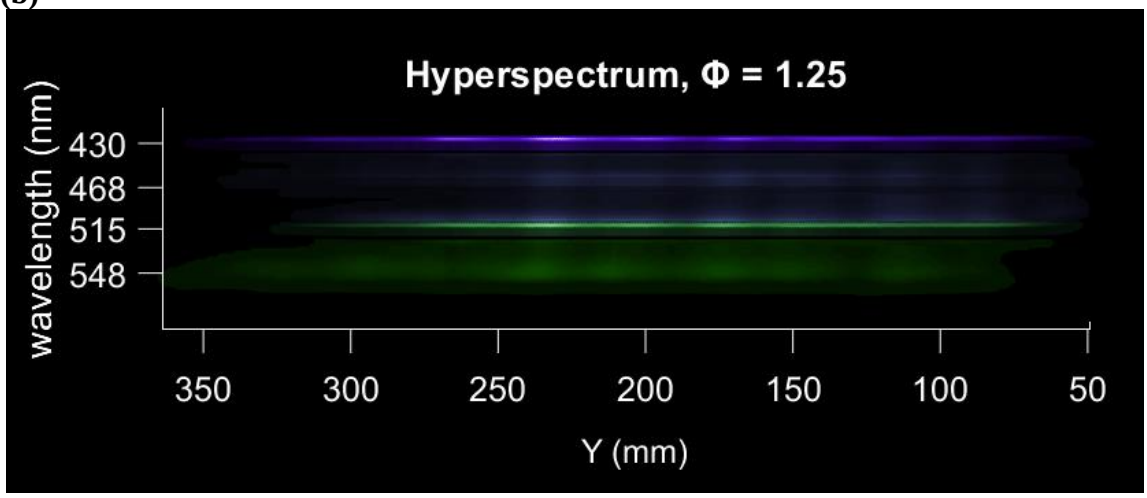


**Figure 43.** (a) Reconstructed hyperspectrum for methane/air flame chemilumiscence with an equivalence ratio of 1.25. (b) When viewed from sideways, the hyperspectrum is identical to a spectral image.

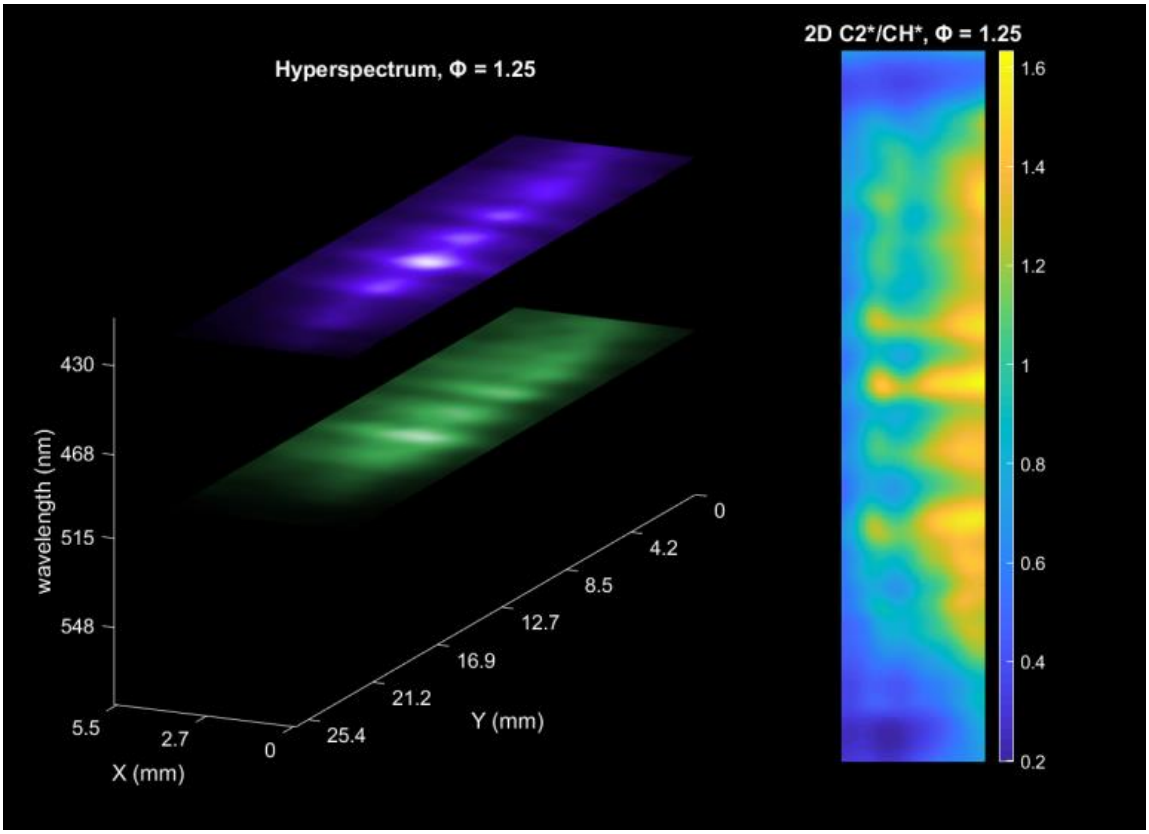


**Figure 44.** The spectral slices at 430 nm and 515 nm can be isolated from the rest of the hyperspectral dataset to obtain the 2D $C_2$*/CH* ratio.

There is some mismatch in the position of the flame between these two slices so that the values in the ratio have some degree of non-uniformity; improvement in the spatial image matching would result in higher uniformity. It should be noted that the reconstruction results exhibited higher than expected $CO_2$* continuum compared to the ground truth indicating that some false signal was produced by the compressed sensing process, however the $CO_2$* emission can be separated from the 2D $C_2$* and CH* slices as Figure 44 demonstrates. This separation capability of compressed hyperspectral imaging is advantageous since removal of the CO2* background is difficult to accomplish in 2D chemiluminescence imaging via filters. Spatial resolution of the reconstructed images was again lower than the ground truth images due to inherent quality loss from the compressed sensing process, but spectral accuracy was good; as shown in Figure 45 (a), the point-spectra for the hyperspectral reconstruction associated with the equivalence ratio of 1.25 were quite close to the ground truth spectrum. Spatial intensity corresponded to spectral accuracy. As an example, point 2 in the spatial image had the highest intensity, and the spectrum produced by the intensity of voxels along the wavelength axis that have the same X-Y coordinates as point 2 is closest to ground truth spectrum, because point 2 has the highest intensity concentration and therefore the highest similarity to the ground truth spectrum. Also, note that the blurring introduced by reconstruction process further broadens spectral lines, and this broadening effect can vary according to the values of the parameters of the reconstruction algorithm used , and the algorithm applied. so for this case, the FWHMs of the spectral lines in recovered spectra are about 3 nm wider than the FWHM in ground truth spectrum, as shown in Figure 45 (b).

The spectra were compared at the different equivalence ratios. Figure 46 (a) shows the ground truth spectra at different equivalence ratios and Figure 46 (b) shows the equivalent spectra from the reconstructed hyperspectra. The reconstruction results show that the intensities of the $C_2$* emission band (515 nm) and side bands (470 nm and 560 nm) increased as equivalence ratio was increased, matching the results from the ground truth spectra. Figure 47 shows the linear relationship between the ratio of CH* and $C_2$* emission intensities and the corresponding equivalence ratio.

**(a)**

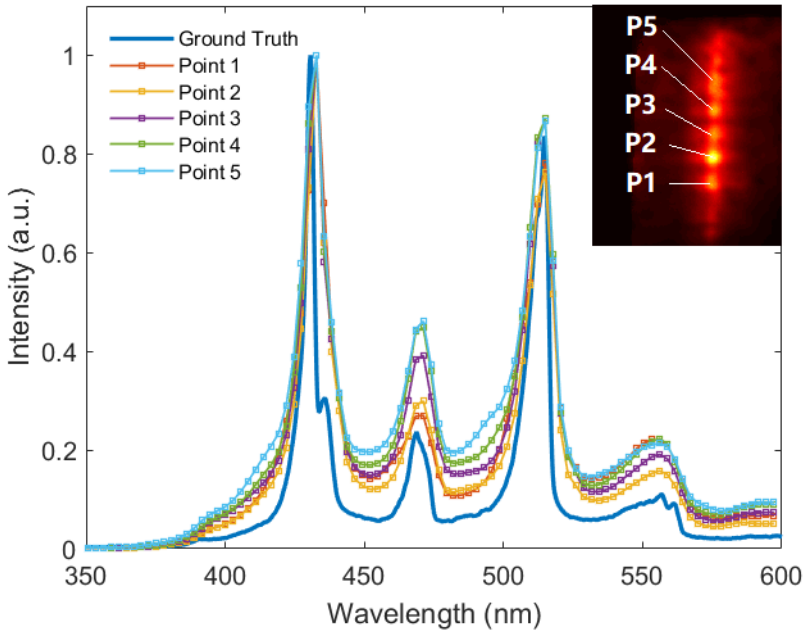


**(b)**

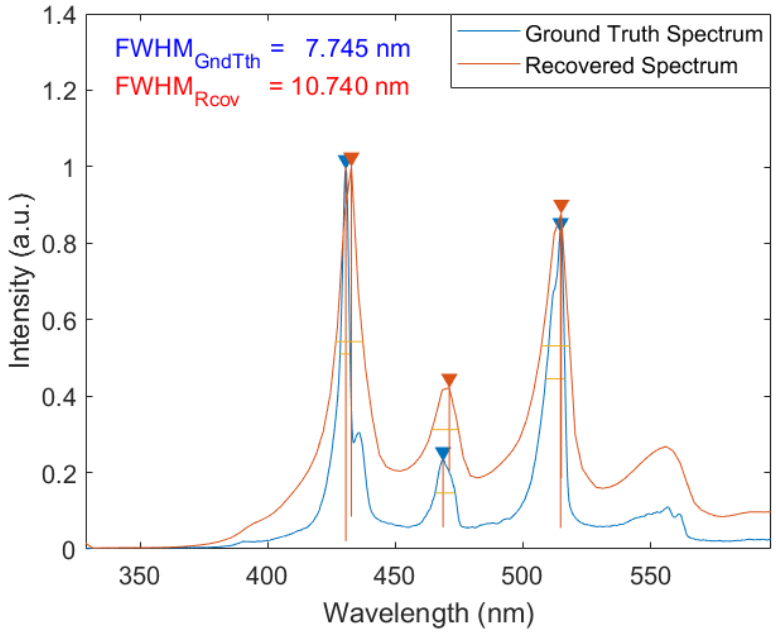


**Figure 45.** (a) Five point-spectra at equivalence ratio of 1.25. The inset spatial image indicates the locations of the selected points in the X-Y plane of the hyperspectrum. (b) A comparison between the ground truth spectrum and the recovered spectrum showing the FWHM of the recovered spectrum is ~3 nm wider. This is due to the blurring caused by the reconstruction algorithm.

**(a)**

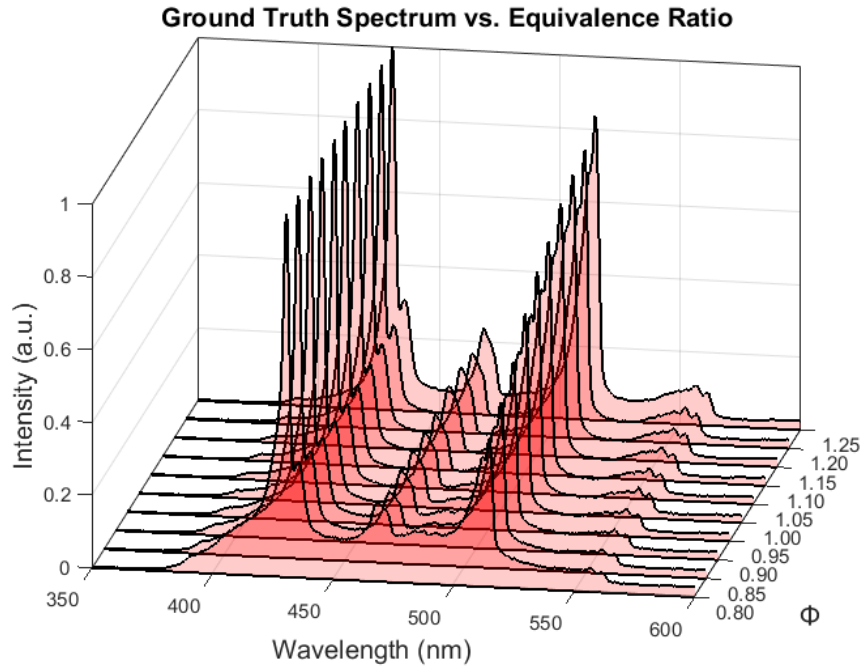


**(b)**

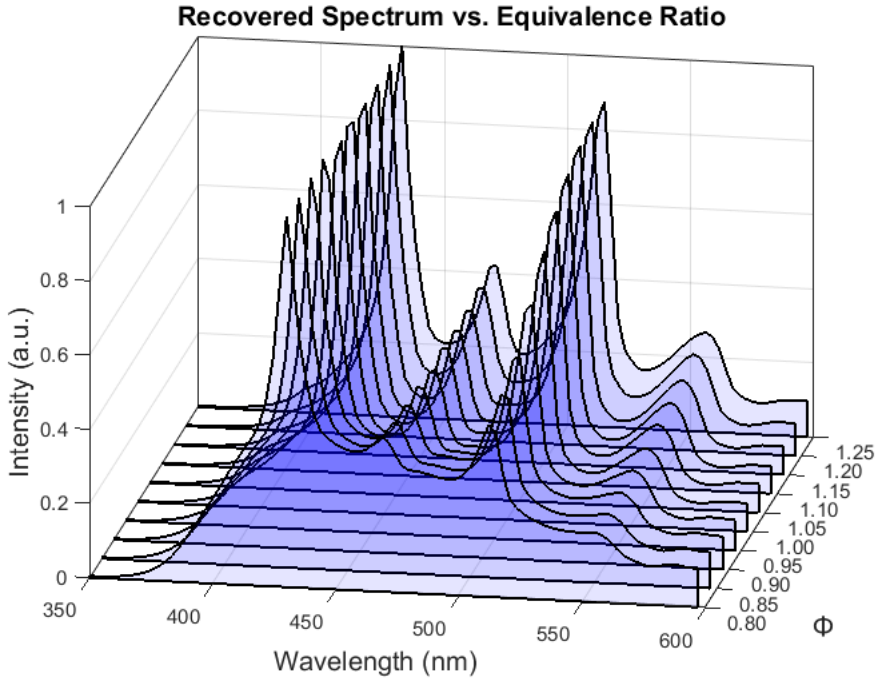


**Figure 46.** (a) Ground truth spectra and (b) spectra extracted from the hyperspectra at different equivalence ratios, showing that the intensities of the $C_2$* emission line as well as the side bands near 470 nm and 560 nm increased with equivalence ratio.

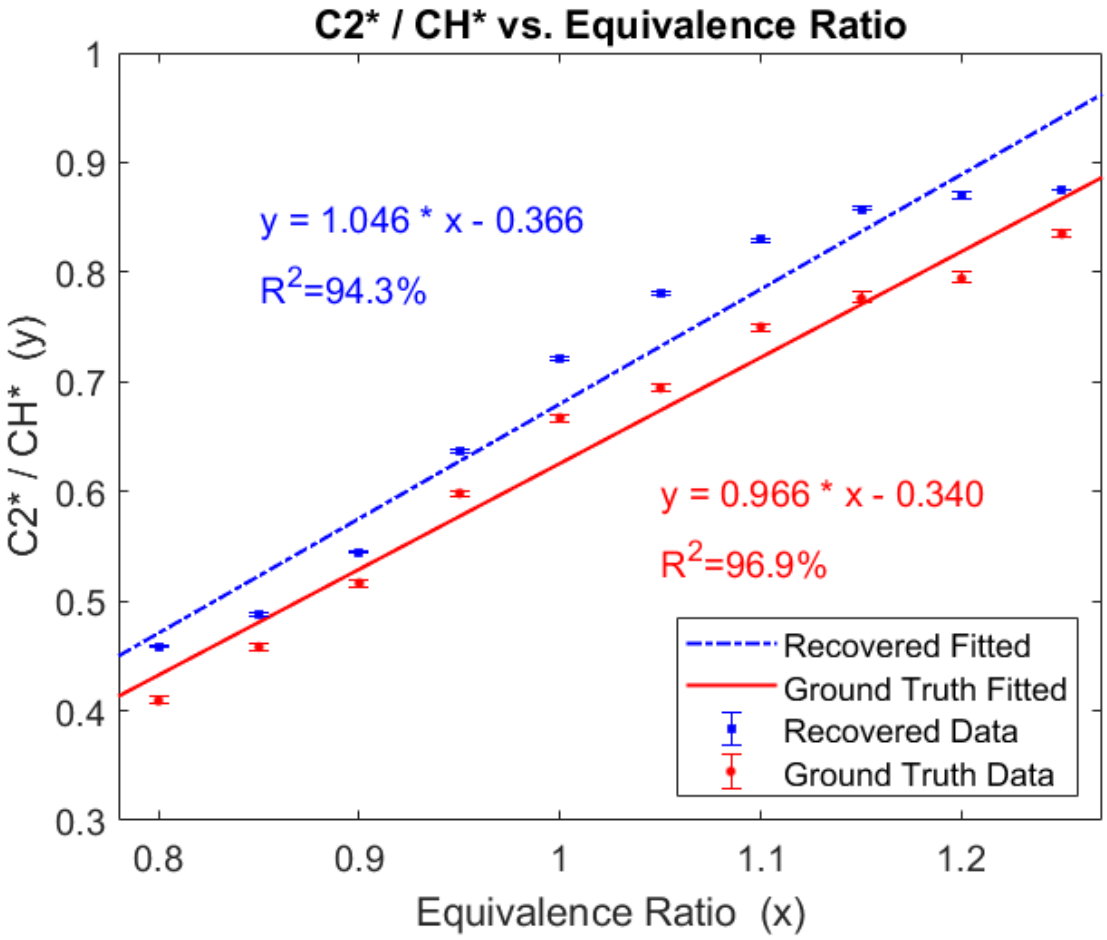


**Figure 47.** The linear relationship between the ratio of CH* and $C_2$* emission intensities and the corresponding equivalence ratio. The error bars in the figure represents minimum and maximum values measured at each data point.

The error bars in the figure represents minimum and maximum values of measurements at each data point. The high consistency in both structure and spectral emission of the flat flame provided a small error range of ±0.224 % for recovered data, and ±0.535 % for ground truth data. The reconstructed results matched closely with the expected values [80, 87], as demonstrated by the $R^2$ value of 93.1% for the reconstructed results' best-fit line as compared to the $R^2$ value of 96.9% for the ground truth correlation. It should be noted that the broadband $CO_2^*$ continuum emissions are not included in the recovery process, which might introduce additional errors for $R^2$ values. Subtractions from a separate monitor near 490nm will help.

## Summary

A compressed single-shot hyperspectral imaging system has been developed and demonstrated by applications to hyperspectral reconstruction of chemiluminescence emissions from methane/air flames. Spatial and spectral information were obtained from the reconstructed hyperspectral data cubes to provide wavelength spectra at any point in the X-Y plane and spatial images at any wavelength. The technique was validated in simulation and by experiment on test cases of simple spectra before application to flame chemiluminescence. It has been shown that the CHAIR reconstruction algorithm developed for this work is able to self-correct non-uniform input intensity. Finally, the reconstructed results of the methane/air flames showed a linear correlation between the ratio of $C_2$* and CH* flame emissions versus equivalence ratio that agreed well with the ground truth results. It should be noted that this technique can turn a spectrometer into a single-shot hyper-spectrometer with the temporal resolution being the same as the direct imaging methods since it does not require any dynamic pattern switching. With a predefined static pattern, the compressed hyperspectral imaging can achieve the temporal resolution of the imaging camera. However, the additional filtering by the random patterns for compressed sensing could reduce light intensity by up to a factor of 2, which might limit its applications for weak emissions.

In future work, the compressed hyperspectral imaging technique will be implemented on other combustion diagnostics, such as laser-induced breakdown spectroscopy. Additionally, the technique can be applied to other transient targets such as plasmas. Higher resolution coding patterns will be tested for better reconstruction quality via a high resolution DMD or etched plate. Single image super-resolution reconstruction may be implemented as a post-image processing application for higher reconstruction quality.

# CHAPTER SIX
# SUMMARY AND FUTURE WORKS

This dissertation included four individual Thomson scattering related projects, each project served as a task to upgrade a specific diagnostic capability of laser Thomson scattering diagnostics to meet a particular need in plasma research, especially fusion plasma. Task 1 has investigated the feasibility of constructing a mobile Thomson scattering system to aid the fusion facilities that need high performance plasma diagnostic support. The PDP system demonstrated in Task 1 features a multiple line-of-sights measurement that allows measurement of radial profile of a plasma via simultaneous data acquisition from 11 points. Task 2 focused on improving temporal resolution of Thomson scattering diagnostics with pulse-burst laser systems. The 10 kHz sampling rate provided by the pulse-burst laser was a great upgrade compared to conventional 10~50 Hz sampling rate provided by pulsed lasers. The a few mini-second-long burst duration provided nearly 100 meaningful measurements of Thomson scattering spectra. Task 3 has validated the hypothesis that forward Thomson scattering can narrow the spectrum hard enough to spectrally separate Thomson scattering and Raman scattering spectrum, providing an alternative approach for Thomson-Raman separation in diagnostics for weakly ionized plasmas. Task 4 developed a compressed sensing based hyperspectral reconstruction technique, and it was implemented on recovering the hyperspectrum of methane-air flame emission, as a preliminary proof-of-principle study for validating the feasibility of hyperspectral imaging of Thomson scattering. Potentially, all four of these tasks can be combined into one powerful Thomson scattering system. Further summaries for each task is discussed subsequently.

## Task 1

The PDP system has demonstrated its capability of simultaneous multiple line-of-sights measurement of an electrothermal arc plasma (ET-arc), and characterized its radial profile of electron temperature and density. However, only 3 out of 11 fibers had captured

Thomson scattering spectra, due to the narrow size of the plasma cone and the field-of-view (FOV) of the collection optics. The experiment did not have enough time to make adjustments to the collection optics so that the FOV can be narrower and concentrate on the plasma, thereby allowing more fibers in the fiber bundle obtaining Thomson scattered light (increasing spatial resolution), and consequently, establishing a more detailed plasma radial profile. Furthermore, the experiment also did not have enough time to take more measurements nor enough time to optimize the overall experimental conditions to maximize the signal-to-noise ratio (SNR) of the measurement.

The other unaddressed problem in the current state of the PDP system is the uneven distribution of laser power across the line of measurements. In the current configuration, the PDP system focuses the laser with a convex lens like any other conventional setup. This means the laser power is higher where the focal point of the lens is, and lower on both sides. This will result in either lower Thomson scattering intensity from the fibers on the sides or potentially over-saturation of Rayleigh scattering in the central fibers.

As a validation for the Thomson scattering diagnostic capability, for future works, more measurements on other plasmas, especially “cleaner” plasmas, such as a glow discharge with less neutrals and less hot gas, should be further conducted to better characterize the PDP system’s diagnostic limits. And on the ET-arc’s side, more time will be needed to integrate the PDP system to the ET-arc system and maximize the SNR as well as the spatial resolution of the measurements.

As for the laser power problem, this can be resolved either with a filter that blocks the Rayleigh band and use a high laser power to make Thomson scattering strong enough across the line of measurements, or potentially, use a focal-shaping diffractive optical element (DOE) before the laser focusing lens to create multiple focal points of the laser for the multiple line-of-sights measurements.

## Task 2

Pulse-burst laser systems were originally designed for aerodynamic researches. This task aim to take advantage of pulse burst lasers' high repetition rate, and apply it on Thomson scattering diagnostics to greatly improve temporal resolution of Thomson scattering measurements, which will be very beneficial for fusion plasma research, especially for observing edge-localized modes. The current results from table-top argon and helium glow discharge plasmas suggest the system is ready to be deployed on fusion-related plasma diagnostics.

## Task 3

Task 3 has demonstrate that in weakly ionized plasmas, rotational Raman scattering and Thomson scattering can be spectrally separated and therefore allows simultaneous measurements of both plasma temperature and density, as well as gas temperature. As a new technique, the current work has not yet fully investigated the limits of the system nor the limits of its application. The current configuration of the system requires tedious realignment every time the angle of observation is changed, due to the purpose of maximizing Thomson scattering intensity.

The future work can start with upgrading the system design and make it more practical to use, such as adding optical fibers into the collection optics for easy change of observation angle, at the cost of signal strength of Thomson scattering. The benefit of using optical fiber is the system becoming more practical to use, as no more repetitive realignment would be needed. The limits of this forward Thomson scattering system also worth further studies. Although, some "soft limits" has been discussed in current work, but more detailed and task-specific limits have not yet been established for practical applications. Also, given the uniqueness of the background correction in this work, a better data acquisition and processing procedure could be further investigated to potentially reduce the uncertainty of the measurements.

## Task 4

Compressed sensing is used in Task 4 to give spectrometers single-shot hyperspectral imaging capability. The aim is to restore the lost spatial information of Thomson scattering, and provide hyperspectra in Thomson scattering measurements. However, this technique is only meaningful when the diagnostic system is capable of taking 2D spatial images. The state-of-the-art Thomson scattering systems are laser induced single-point measurements, even if the spectrometer slit is fully opened to preserve spatial information, the spectral image can only obtain an image of 1D laser beam and Thomson scattered photons around it. Therefore, for compressed hyperspectral imaging of Thomson scattering to be meaningful, it requires emission from, for instance, a planar laser induced 2D Thomson scattering, which is a technique currently unavailable. Therefore, as preliminary study for that future application, the emission source was replaced by a 2D methane-air flame emission. The measurements from the reconstructed hyperspectrum of the flame emission are a proof-of-principle of this compressed hyperspectral imaging technique.

However, for this technique to be implemented on future Thomson scattering diagnostics, the system requires improvements on both its reconstruction algorithm and hardware. For algorithm, the core of the CHAIR algorithm developed for this task is based on TwIST, however, there are other algorithms that have not yet been tested and could potentially yield better reconstruction quality. A lately developed new algorithm TVAL3D has been compared with TwIST and yielded superior reconstruction results [88]. Updating CHAIR algorithm will enhance the quality of compressed hyperspectral imaging. On the other hand, adjustments on the imaging hardware should be investigated in the future for better imaging quality. First, the digital micro-mirror device is not an ideal coding device, it's small, and more importantly, it's reflective nature forces it to be placed non-perpendicular to the optical axis of the collection optics, and leave part of the regions unfocused in the image. Therefore, for future work, a transparent coding device will be more preferable. Experimentally, Thomson scattering intensity is much weaker than flame emission, it will be a challenge to image Thomson scattering hyperspectrum, especially when the random coding takes away half of its total intensity. Also, in terms of measurements, both the

uncertainty of electron temperature and density will increase due to the broadening (blurriness effect) from the reconstruction algorithm. Therefore, the next step for compressed hyperspectral imaging could be taking measurements from plasma emissions, and then rotational Raman scattering of air.

# REFERENCES


[1] T. P. Hughes, "A New Method for the Determination of Plasma Electron Temperature and Density from Thomson Scattering of an Optical Maser Beam", Nature, **194**, 268–269 (1962).

[2] M. Oliphant, P. Harteck and E. Rutherford, "Transmutation effects observed with heavy hydrogen", Proc. R. Soc. Lond. A, **144**, 692–703 (1934).

[3] V.P. Smirnov, "Tokamak foundation in USSR/Russia 1950–1990", Nucl. Fusion, **50** 014003 (2010).

[4] M. Barbarino, "A brief history of nuclear fusion", Nat. Phys., **16**, 890–893 (2020).

[5] T. Casper, Y. Gribov, A. Kavin, and et. al., "Development of the ITER baseline inductive scenario", Nucl. Fusion, **54** 013005 (2014).

[6] D. Hartmann, "Stellerators", Fusion Sci. and Tech., 61:2T, 46-58 (2017)

[7] Y. Xu, "A general comparison between tokamak and stellarator plasmas", Matter and Radiation at Extremes, **1**, 192 (2016).

[8] W. Biel, K. Lackner, O. Sauter and et. al., "Comment on 'On the fusion triple product and fusion power gain of tokamak pilot plants and reactors', by A. Costley", Nucl. Fusion, **57** 038001 (2016).

[9] Spitzer, Lyman Jr., "Controlled Nuclear Fusion Research, September 1965: Review Of Experimental Results", International Atomic Energy Agency, 792, 3-11 (1966); Conference on Plasma Physics and Controlled Nuclear Fusion Research, 6-10 (1965), ISSN 0074-1884.

[10] T. Hender, J. Wesley, J. Bialek and et. al., "Chapter 3: MHD stability, operational limits and disruptions", Nucl. Fusion, **47** S128 (2007).

[11] Y. Liang, "Overview of Edge-Localized Mode Control in Tokamak Plasmas", Fusion Sci. and Tech., 59:3, 586-601 (2011).

[12] H. Zohm, "Edge localized modes (ELMs)", Plasma Phys. Control. Fusion, **38** 105 (1996).

[13] A. Leonard, "Edge-localized-modes in tokamaks", Physics of Plasmas, **21**, 090501 (2014).

[14] M. Wade, “Physics and engineering issues associated with edge localized mode control in ITER”, Fusion Engineering and Design, **84**, 178-185 (2009).

[15] W. Lee, "Development of Raman and Thomson scattering diagnostics for study of energy transfer in nonequilibrium, molecular plasmas," PhD diss., The Ohio State University, (2003).

[16] A. Roettgen, I. Shkurenkov, M. Simeni Simeni, I. V. Adamovich, and W. R. Lempert, "Time-resolved electron temperature and electron density measurements in a nanosecond pulse filament discharge in H2–He and O2–He mixtures," Plasma Sources Science and Technology, **25**, 055008 (2016).

[17] A. Murphy, “Thomson scattering diagnostics of thermal plasmas: Laser heating of electrons and the existence of local thermodynamic equilibrium”, Phys. Rev. E, **69**, 016408 (2004).

[18] A. Murphy, “Electron Heating in the Measurement of Electron Temperature by Thomson Scattering: Are Thermal Plasmas Thermal?”, Phys. Rev. Lett. **89**, 025002 (2002).

[19] R. Engeln, B. Klarenaar, and O. Guaitella, “Foundations of optical diagnostics in low-temperature plasmas”, Plasma Sources Science and Technology, **29**, 063001 (2020).

[20] Z. He, C. Smith, Z. Zhang, and et. al., “Pulse-burst laser-based 10 kHz Thomson scattering measurements”, Plasma Sci. Technol., **21** 105603 (2019).

[21] N. Kafle, D. Elliott, E. Garren, and et. al., “Design and implementation of a portable diagnostic system for Thomson scattering and optical emission spectroscopy measurements”, Rev. Sci. Instrum, **92**, 063002 (2021).

[22] E. Lindquist, T. Gebhart, D. Elliott, and et. al., “Reconfiguration of an Electrothermal-Arc Plasma Source for In Situ PMI Studies”, Fusion Sci. and Tech., **77**:7-8, 921-927 (2021).

[23] T. Gebhart, L. Baylor, J. Rapp, A. Winfrey, “Characterization of an electrothermal plasma source for fusion transient simulations”, Journal of Applied Physics, **123**, 033301 (2018).

[24] T. Gebhart, “Design and Characterization of an Electrothermal Plasma Source for Fusion Plasma Transient Simulation”, Ann Arbor: University of Florida (2016).

[25] J. Coburn, T. Gebhart, C. Parish, and et. al., “Surface Erosion of Plasma-Facing Materials Using an Electrothermal Plasma Source and Ion Beam Micro-Trenches”, Fusion Science and Technology, **75**:7, 621-635 (2019).

[26] C. Smith, “Characterization of a Digital Holography Diagnostic for In Situ Erosion Measurement of Plasma-Facing Components in Fusion Devices”, PhD diss., University of Tennessee, (2020).

[27] D. Evans and J. Katzenstein, “Laser light scattering in laboratory plasmas”, Rep. Prog. Phys., **32** 207 (1969).

[28] G. Fiocco, and E. Thompson, “Thomson Scattering of Optical Radiation from an Electron Beam”, Phys. Rev. Lett., **10**, 89 (1963).

[29] J. Russell, and R. Cohn, “Thomson Scattering”, Book on Demand (2012).

[30] D. Froula, S. Glenzer, N. Luhmann, and J. Sheffield, “Chapter 1 - Introduction in Plasma Scattering of Electromagnetic Radiation (Second Edition)”, Academic Press: Boston. p. 1-30 (2011).

[31] T. Biewer, S. Meitner, J. Rapp, and et. al., “First results from the Thomson scattering diagnostic on proto-MPEX”, Review of Scientific Instruments, **87**, 11E518 (2016).

[32] N. Kafle, T. Biewer, and D. Donovan, “Dual-pass upgrade to the Thomson scattering diagnostic on the Prototype-Material Plasma Exposure eXperiment (Proto-MPEX)”, Review of Scientific Instruments, **89**, 10C107 (2018).

[33] N. Kenmochi, M. Nishiura, Z. Yoshida, and et. al., “Nd:YAG laser Thomson scattering diagnostics for a laboratory magnetosphere”, Review of Scientific Instruments, **89**, 10C101 (2018).

[34] M. Sos, P. Bohm, O. Grover, and et. al., “Observation and evaluation of the alignment of Thomson scattering systems”, Review of Scientific Instruments, **89**, 10C105 (2018).

[35] S. Rocco, J. Banasek, W. Potter, and D. Hammer, “Time-resolved and multiple-angle Thomson scattering on gas-puff Z-Pinch plasmas at pinch time”, Review of Scientific Instruments, **89**, 10C117 (2018).

[36] J. Banasek, T. Byvank, S. Rocco, and et. al., “Time-Resolved Thomson Scattering on Laboratory Plasma Jets”, IEEE Transactions on Plasma Science, **46** (11): p. 3901-3905 (2018).

[37] T. Carlstrom, F. Glass, D. Du, and et. al., “Thomson scattering measurements on DIII-D using in-vessel laser mirrors and lenses to diagnose a new divertor location”, Review of Scientific Instruments, Review of Scientific Instruments, **89**, 10C111 (2018).

[38] A. Ottaviano, T. Schindler, K. Zhai, and et. al., “Characterization and calibration of the Thomson scattering diagnostic suite for the C-2W field-reversed configuration experiment”, Review of Scientific Instruments, **89**, 10C120 (2018).

[39] R. Patton, K. Gabet, N. Jiang, and et. al., “Multi-kHz temperature imaging in turbulent non-premixed flames using planar Rayleigh scattering”, Applied Physics B, **108**, 377-392 (2012).

[40] R. Patton, K. Gabet, N. Jiang, and et. al., “Multi-kHz mixture fraction imaging in turbulent jets using planar Rayleigh scattering”, Applied Physics B, **106**, 457-471 (2012).

[41] C. Kaminski, J. Hult, and M. Aldén, “High repetition rate planar laser induced fluorescence of OH in a turbulent non-premixed flame”, Applied Physics B, **68**, 757-760 (1999).

[42] N. Jiang and W. Lempert, “Ultrahigh-frame-rate nitric oxide planar laser-induced fluorescence imaging”, Opt. Lett. **33**, 2236-2238 (2008).

[43] N. Jiang, M. Webster, W. Lempert, and et. al., “MHz-rate nitric oxide planar laser-induced fluorescence imaging in a Mach 10 hypersonic wind tunnel”, Appl. Opt., **50** (4), A20-A28 (2011).

[44] N. Jiang, R. Patton, W. Lempert, and J. Sutton, “Development of high-repetition rate CH PLIF imaging in turbulent nonpremixed flames”, Proc. Combust. Inst., **33** (1), 767-774 (2011).

[45] J. Miller, S. Engel, T. Meyer, T. Seeger, and A. Leipertz, “High-speed CH planar laser-induced fluorescence imaging using a multimode-pumped optical parametric oscillator”, Opt. Lett., **36** (19), 3927-3929 (2011).

[46] M. Slipchenko, J. Miller, S. Roy, and et. al., “Quasi-continuous burst-mode laser for high-speed planar imaging”, Opt. Lett., **37** (8), 1346-1348 (2012).

[47] K. Gabet, N. Jiang, W. Lempert, and J. Sutton, “Demonstration of high-speed 1D Raman scattering line imaging”, Applied Physics B, **101**, 1-5 (2010).

[48] D. Hartog, J. Ambuel, M. Borchardt, and et. al., “Pulse-burst laser systems for fast Thomson scattering (invited)”, Review of Scientific Instruments, **81**, 10D513 (2010).

[49] D. Hartog., M. Borchardt, D. Holly, A. Diallo, and B. LeBlanc, “A pulse-burst laser system for Thomson scattering on NSTX-U”, Journal of Instrumentation, **12** (10), C10002-C10002 (2017).

[50] M. Slipchenko, J. Miller, S. Roy, J. Gord, and T. Meyer, “All-diode-pumped quasi-continuous burst-mode laser for extended high-speed planar imaging”, Optics Express, **21** (1), 681-689 (2013).

[51] M. Laroussi, “Cold Plasma in Medicine and Healthcare: The New Frontier in Low Temperature Plasma Applications”, Frontiers in Physics, **8** (2020).

[52] M. Kehrer, A. Rottensteiner, W. Hartl, and etl. al., “Cold atmospheric pressure plasma treatment for adhesion improvement on polypropylene surfaces”, Surface and Coatings Technology, **403**, 126389 (2020).

[53] A. Bogaerts, X. Tu, J. C. Whitehead, and et. al., “The 2020 plasma catalysis roadmap”, Journal of Physics D: Applied Physics, **53**, 443001 (2020).

[54] D. Laroque, S. Seó, G. Valencia, J. Laurindo, and B. Carciofi, “Cold plasma in food processing: Design, mechanisms, and application”, Journal of Food Engineering, **312**, 110748 (2022).

[55] S. Pankaj, Z. Wan, and K. Keener, “Effects of Cold Plasma on Food Quality: A Review”, Foods, **7**, 4 (2018).

[56] M. Bogle, K. Arndt, and J. Dover, “Evaluation of Plasma Skin Regeneration Technology in Low-Energy Full-Facial Rejuvenation”, Archives of Dermatology, **143**, 168-174 (2007).

[57] R. Engeln, B. Klarenaar, and O. Guaitella, “Foundations of optical diagnostics in low-temperature plasmas”, Plasma Sources Science and Technology, **29**, 063001 (2020).

[58] S. Park, W. Choe, S. Moon, and S. Yoo, “Electron characterization in weakly ionized collisional plasmas: from principles to techniques”, Advances in Physics: X, **4**, 1526114 (2019).

[59] Y. Pan, K. Tomita, Y. Kawai, M. Matsukuma, and K. Uchino, “Measurements of spatial distributions of electron density and temperature of 450 MHz UHF plasma using laser Thomson scattering”, Japanese Journal of Applied Physics, **60**, SAAB03 (2020).

[60] S. Hübner, J. Sousa, J. van der Mullen, and W. Graham, “Thomson scattering on non-thermal atmospheric pressure plasma jets”, Plasma Sources Science and Technology, **24**, 054005 (2017).

[61] A. van Gessel, E. Carbone, P. Bruggeman, and J. van der Mullen, “Laser scattering on an atmospheric pressure plasma jet: disentangling Rayleigh, Raman and Thomson scattering”, Plasma Sources Science and Technology, **21**, 015003 (2012).

[62] R. Miles, A. Dogariu, and L. Dogariu, “Localized time accurate sampling of nonequilibrium and unsteady hypersonic flows: methods and horizons”, Experiments in Fluids, **62**, 248 (2021).

[63] C. Filip, S. Tochitsky, R. Narang, and et. al., “Collinear Thomson scattering diagnostic system for the detection of relativistic waves in low-density plasmas”, Review of Scientific Instruments, **74**, 3576-3578 (2003).

[64] S. Glenzer, O. Landen, P. Neumayer, and et. al., “Observations of Plasmons in Warm Dense Matter”, Physical Review Letters, **98**, 065002 (2007).

[65] E. Carbone and S. Nijdam, “Thomson scattering on non-equilibrium low density plasmas: Principles, practice and challenges”, Plasma Phys. Control. Fusion, **57**, 014026 (2014).

[66] N. Jiang, P. Hsu, J. Mance, and et. al., “High-speed 2D Raman imaging at elevated pressures”, Opt. Lett., **42**, 3678-3681 (2017).

[67] M. Gragston, P. Hsu, A. Patnaik, Z. Zhang, and S. Roy, “Time-Gated Single-Shot Picosecond Laser-Induced Breakdown Spectroscopy (ps-LIBS) for Equivalence-Ratio Measurements”, Applied Spectroscopy, **74** (3), 340-346 (2020).

[68] Y. Wu, M. Gragston, Z. Zhang, and et. al., “High-pressure 1D fuel/air-ratio measurements with LIBS”, Combustion and Flame, **198**, 120-129 (2018).

[69] N. Jiang, P. Hsu, P. Danehy, Z. Zhang, and S. Roy, “Simultaneous measurements of mixture fraction and flow velocity using 100 kHz 2D Rayleigh scattering imaging”, Appl. Opt., **58**, C30-C35 (2019).

[70] Y. Wu, J. Sawyer, Z. Zhang, and S. Adams, “Flame temperature measurements by radar resonance-enhanced multiphoton ionization of molecular oxygen”, Appl. Opt., **51**, 6864-6869 (2012).

[71] Y. Wu, M. Gragston, and Z. Zhang, “Experimental Characterizations of Ethanol and Jet-A Liquid Spray Flames”, AIAA Aerospace Sciences Meeting (2018).

[72] Y. Wu, C. Smith, and Z. Zhang, “Quantitative O2 Measurements in Flames at Elevated Pressures by Laser-induced Breakdown Spectroscopy”, the 54th AIAA Aerospace Sciences Meeting, San Diego, California (2016).

[73] B. Halls, N. Jiang, J. Gord, P. Danehy, and S. Roy, “Mixture-fraction measurements with femtosecond-laser electronic-excitation tagging”, Appl. Opt., **56**, E94-E98 (2017).

[74] C. Liu, C. Straif, T. Flügel-Paul, U. Zeitner, and H. Gross, “Comparison of hyperspectral imaging spectrometer designs and the improvement of system performance with freeform surfaces”, Appl. Opt., **56**, 6894-6901 (2017).

[75] Y. Eldar, and G. Kutyniok, “Compressed Sensing: Theory and Applications”, Cambridge University Press (2012).

[76] D. Donoho, “Compressed sensing”, IEEE Transactions on Information Theory, **52**, 1289-1306 (2006).

[77] M. Fickus, M. Lewis, D. Mixon, and J. Peterson, “Compressive Hyperspectral Imaging for Stellar Spectroscopy”, IEEE Signal Processing Letters, **22**, 1829-1833 (2015).

[78] J. Thompson, J. Bixler, B. Hokr, and et. al., “Single-shot chemical detection and identification with compressed hyperspectral Raman imaging”, Optics Letters, **42**, 2169-2172 (2017).

[79] A. Barducci, D. Guzzi, C. Lastri, and et. al., “Compressive sensing and hyperspectral imaging”, Proc. SPIE 10564, International Conference on Space Optics, ICSO 2012, 105642Z (2017).

[80] W. McCord, M. Gragston, Y. Wu, and et. al., “Quantitative fuel-to-air ratio determination for elevated-pressure methane/air flames using chemiluminescence emission”, Applied Optics, **58**, C61-C67 (2019).

[81] Z. Zhang, M. Shneider, and R. Miles, “Coherent microwave rayleigh scattering from resonance-enhanced multiphoton ionization in argon”, Physical Review Letters, **98** (26), 265005 (2007).

[82] S. Roy, J. Gord, and A. Patnaik, “Recent advances in coherent anti-Stokes Raman scattering spectroscopy: Fundamental developments and applications in reacting flows”, Progress in Energy and Combustion Science, **36**, 280-306 (2010).

[83] J. Daily, “Laser induced fluorescence spectroscopy in flames”, Progress in Energy and Combustion Science, **23**, 133-199 (1997).

[84] J. Bioucas-Dias, and M. Figueiredo, “A New TwIST: Two-Step Iterative Shrinkage/Thresholding Algorithms for Image Restoration”, IEEE Transactions on Image Processing, **16**, 2992-3004 (2007).

[85] Y. Wu, Z. Zhang, S. Adams, “O2 Rotational Temperature Measurements by Coherent Microwave Scattering from REMPI”, Chemical Physics Letters, **513**, 191-194 (2011).

[86] Y. Wu, A. Bottom, Z. Zhang, T. Ombrello, and V. Katta, “Direct Measurement of Methyl Radical in Methane/Air Flame at Atmospheric Pressure by Radar REMPI”, Optics Express, **19** (24), 23997-24004 (2011).

[87] K. Wang, F. Li, Y. Wu, and X. Yu, “Quantitative Measurements of Chemiluminescence in a Laminar Methane–Air Premixed Flame and Comparison to Numerical Methods”, Energy & Fuels, **32**, 5536-5543 (2018).

[88] F. Yin, Y. Meng, Q. Yang, and et. al., “High precision reconstruction for compressed femtosecond dynamics images based on the TVAL3 algorithm”, Optical Materials Express, **12** (11), 4435-4443 (2022).

# VITA

In 2015, Zichen He received his Bachelor degree in Biomedical Engineering at Northeastern University in Shenyang, China. He continued his study in biomedical engineering at University of Wisconsin-Milwaukee and obtained his Master of Science Degree in Biomedical Engineering in 2017, where he focused his field of research in applications of electrical engineering and enhanced his skills and knowledge in electronics and digital signal and image processing. Later, he had a lot of fun working as a research and development engineer for a virtual reality company for more than half a year before resuming higher education. So, in 2018, he moved to Knoxville, Tennessee and began his new adventure as a PhD student with Professor Zhili Zhang as his advisor. There, Zichen's study has changed from biomedical engineering to mechanical engineering, and his field of research was focused on laser diagnostics and computational imaging. From 2019 to 2021, Zichen worked as a student researcher on an ARPA-E founded Thomson scattering project under subcontract at Oak Ridge National Laboratory with Dr. Theodore Biewer as the principle investigator. After that, he continued his research at University of Tennessee until graduation.